



UNIVERSIDADE
ESTADUAL DE LONDRINA

DÉBORA RODRIGUES ROCHA

**MULTI-TECHNIQUE ANALYSIS TO ESTIMATE THE
MAXIMUM TEMPERATURE REACHED IN A BURNED
RED-YELLOW LATOSOL IN THE SOUTHERN AMAZON**

DÉBORA RODRIGUES ROCHA

**MULTI-TECHNIQUE ANALYSIS TO ESTIMATE THE
MAXIMUM TEMPERATURE REACHED IN A BURNED
RED-YELLOW LATOSOL IN THE SOUTHERN AMAZON**

Thesis presented as a partial requirement for
obtaining the degree of Doctor in Physics, State
University of Londrina.

Advisor: Prof. Dr. Fábio Luiz Melquiades
Coadvisor: Prof. Dr. Edivaldo Lopes Thomaz

Londrina
2022

Ficha de identificação da obra elaborada pelo autor, através do Programa de Geração Automática do Sistema de Bibliotecas da UEL

R672m Rocha, Débora Rodrigues.
Multi-technique analysis to estimate the maximum temperature reached in a burned Red-Yellow Latosol in the Southern Amazon / Débora Rodrigues Rocha. - Londrina, 2022.
99 f. : il.

Orientador: Fábio Luiz Melquiades.
Coorientador: Edivaldo Lopes Thomaz.
Tese (Doutorado em Física) - Universidade Estadual de Londrina, Centro de Ciências Exatas, Programa de Pós-Graduação em Física, 2022.
Inclui bibliografia.

1. Efeitos do fogo no solo - Tese. 2. EDXRF - Tese. 3. Estimativa de temperatura máxima - Tese. 4. Análise multivariada - Tese. I. Melquiades, Fábio Luiz. II. Thomaz, Edivaldo Lopes. III. Universidade Estadual de Londrina. Centro de Ciências Exatas. Programa de Pós-Graduação em Física. IV. Título.

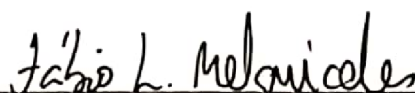
CDU 53

DÉBORA RODRIGUES ROCHA

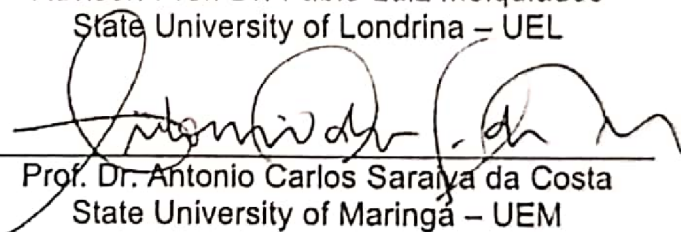
**MULTI-TECHNIQUE ANALYSIS TO ESTIMATE THE
MAXIMUM TEMPERATURE REACHED IN A BURNED
RED-YELLOW LATOSOL IN THE SOUTHERN AMAZON**

Thesis presented as a partial requirement for
obtaining the degree of Doctor in Physics,
State University of Londrina.

EVALUATION COMMITTEE



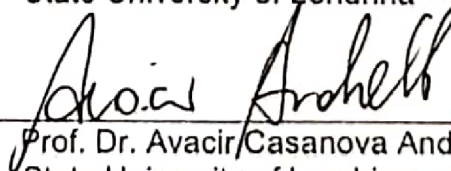
Advisor: Prof. Dr. Fábio Luiz Melquiades
State University of Londrina – UEL



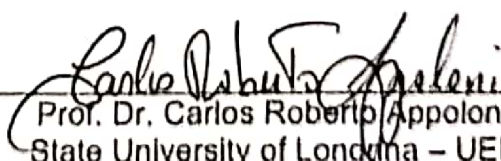
Prof. Dr. Antônio Carlos Saraya da Costa
State University of Maringá – UEM



Prof. Dr. Pedro Rodolfo Siqueira Vendrame
State University of Londrina – UEL



Prof. Dr. Avacir Casanova Andrello
State University of Londrina – UEL



Prof. Dr. Carlos Roberto Appoloni
State University of Londrina – UEL

Londrina, July 05th, 2022.

I would like to dedicate this work to God
through the hands of Virgin Mary.

ACKNOWLEDGEMENTS

I wish to thank my advisor, Prof. Fábio Luiz Melquiades, for being such a nice person, professor and scientist. Thank you for guiding, motivating, and supporting me during these years. I also thank my co-advisor, Prof. Edivaldo Lopes Thomaz, for all the support regarding the samples and the topics about soil and forest fires.

Many thanks to all the professors of the Physics Department who put lights in my way during my Ph.D. development. I wish to thank the friends who helped me with the lectures, tests, measurements, English practicing... Thank you for all the fruitful discussions and laughing moments, Fábio Lopes, José Vinícius, Diego, Felipe, Sandro, José Vitor and João Lucas.

I would like to thank my internship advisor, Prof. Jorge Mataix-Solera. I also thank Prof. Vicky, the colleagues Sara, Minerva, Raouf, and Virtudes. You all made my internship at Miguel Hernández University, Spain, much greater than I could ever imagine.

I am very thankful to CAPES, INCT-FNA and CNPq for the grants received to develop my Ph.D., and to the State University of Londrina and the Nuclear Applied Physics Laboratory for being the places where such study started and was made possible.

I thank the girls who were my roommates for some period of these studying years, Fabiana, Maria Julia, Laura, Rafaela, Ana Vitória, Roshni, Georgi, Rosa, and Rebeca. A special thanks to all my friends from GOU Emanuel, JS, Canção Nova, and PIO. Sharing my daily life with you was a great experience and I learned a lot from you all.

I would like to express all my gratitude to my family, mom, dad, and brother – Cleidenice, Aguinaldo and Pedro –, for always trusting in me and believing in my dreams, even when I did not believe myself. Thank you for being my relief and my joy. Many thanks to my grandmother, Aparecida, and grandfather, Luiz, especially for Sunday's afternoon coffees fulfilled with love and encouragement.

Above all, I thank God, who made all these experiences possible and amazing.

"There is nothing like looking, if you want to find something. You certainly usually find something, if you look, but it is not always quite the something you were after."

J. R. R. Tolkien – The Hobbit

RESUMO

ROCHA, Débora Rodrigues. **Análise multitécnica para estimar a temperatura máxima atingida em um Latossolo Vermelho-Amarelo de queimada no sul da Amazônia.** 2022. 99 p. Tese de doutorado (Física), Universidade Estadual de Londrina, Londrina, 2022.

Conhecer a temperatura máxima atingida no solo durante uma queimada é importante para avaliar a intensidade da queima. A conversão de florestas é um processo contínuo nos ecossistemas da Amazônia, sendo de grande importância prever os efeitos do fogo nas propriedades do solo e evitar danos aos sistemas ambientais. Métodos espectroscópicos combinados com análise multivariada podem fornecer informações químicas e mineralógicas importantes sobre o solo. Este estudo teve como objetivo prever a temperatura máxima atingida em um Latossolo Vermelho-Amarelo de uma região amazônica no Brasil. Foram investigadas amostras de roça de toco e de pastagens coletadas após eventos de incêndio, e amostras de solo não queimado submetidas ao aquecimento de mufla (150 a 800°C). A fluorescência de raios X por dispersão de energia (EDXRF) foi empregada para adquirir dados químicos. O procedimento experimental é rápido, requer preparação mínima da amostra e nenhum reagente químico. A concentração dos elementos e os dados espectrais foram analisados utilizando Análise de Componentes Principais (PCA) e regressão por Mínimos Quadrado Parciais (PLS). Além da EDXRF, foram realizadas análises com outras técnicas: análise térmica, tabela de cores Munsell, susceptibilidade magnética, difração de raios X (XRD) e espectroscopia no visível e no infravermelho próximo (Vis-NIR). A PCA realizada com as concentrações elementares da EDXRF apresentou uma tendência de agrupamento das amostras por seus locais de coleta. Os grupos formados de acordo com a temperatura não foram tão expressivos quanto os formados pelos locais de coleta. Modelos PLS com dados espectrais de EDXRF foram utilizados para prever a temperatura máxima atingida em amostras de solo. As temperaturas estimadas variaram de 325 a 608°C, faixa de temperatura relatada na literatura. A análise térmica indicou as principais transformações nos solos estudados (decomposição da matéria orgânica, desidroxilação da gibbsita, goethita e caulinita). Todas as amostras apresentaram comportamento semelhante. As cores Munsell concordaram com os resultados da análise térmica. Em geral, os valores de susceptibilidade magnética encontrados foram baixos, indicando um pequeno teor de minerais magnéticos (maghemita) nos solos. As análises por XRD e Vis-NIR indicaram os minerais presentes nos solos. A PCA desenvolvida com as intensidades dos picos dos minerais indicou que o local de coleta e a temperatura de aquecimento desempenham um papel importante na caracterização do solo, pois as componentes principais agruparam as amostras de acordo com tais características das amostras. Considerando as vantagens e resultados instrumentais, o emprego de técnicas espectroscópicas como a EDXRF, aliadas à análise multivariada, tem se mostrado uma tecnologia alternativa viável para avaliar os efeitos do fogo no solo.

Palavras-chave: efeitos do fogo no solo; EDXRF; regressão PLS; estimativa de temperatura; aquecimento controlado.

ABSTRACT

ROCHA, Débora Rodrigues. **Multi-technique analysis to estimate the maximum temperature reached in a burned Red-Yellow Latosol in the Southern Amazon**. 2022. 99 p. PhD thesis (Physics), State University of Londrina, Londrina, 2022.

Knowing the maximum temperature reached in soil during burning is important to evaluate fire intensity. Forest conversion is an ongoing process in Amazon ecosystem. It is of utmost importance to predict fire effects on soil properties and avoid damaging environmental systems. Spectroscopic methods combined with multivariate statistics may provide soil chemical and mineralogical information. This study aims at predicting the maximum temperature reached in a Red-Yellow Latosol from an Amazonian region in Brazil. Slash-and-burn and pasture samples collected after fire events, and unburned soil samples submitted to muffle heating (150 to 800°C) were investigated. Energy dispersive X-ray fluorescence (EDXRF) was employed to acquire chemical data. The experimental procedure is rapid, requires minimal sample preparation and no chemical reagents. The concentration of the elements and the spectral data were analyzed using Principal Component Analysis (PCA) and Partial Least Squares regression (PLS). In addition to EDXRF, some other analyses were performed: thermal analysis, Munsell color chart, magnetic susceptibility, X-ray diffraction (XRD) and visible and near-infrared spectroscopy (Vis-NIR). The PCA performed with the elemental concentrations presented a tendency of grouping the samples by their collection sites. The groups formed according to heating temperature were not as expressive as the ones formed by collection sites. Partial least squares regression with EDXRF spectral data was successfully applied to predict the maximum temperature reached in soil samples. Estimated temperatures ranged from 325 to 608°C, a temperature range which has been reported elsewhere. Thermal analysis indicated the main transformations in the studied soils (organic matter decomposition; gibbsite, goethite and kaolinite dehydroxylation). In general, the samples had similar behavior. The Munsell colors observed, which are transformation indicators, agreed with thermal analysis results. In general, values of magnetic susceptibility found in this study were low, indicating a small content of magnetic minerals (maghemite) in the investigated soils. The XRD and Vis-NIR analyses indicated the minerals present in the studied soil. The PCA developed with the peak intensities of the minerals indicated that the collection site and the temperature of heating play an important role in the soil characteristics, as the principal components grouped the samples according to such features of soils. Considering the instrumental advantages and results, the employment of spectroscopic techniques such as EDXRF combined with multivariate analysis has proved to be a feasible alternative technology to evaluate fire effects in the soil.

Key-words: fire effects on soil; EDXRF; PLS regression; temperature estimation; controlled heating.

LIST OF FIGURES

Figure 1 –	Representation of photoelectric effect and characteristic X-ray fluorescence radiation in an atom.....	24
Figure 2 –	Munsell Color System for color notating	29
Figure 3 –	Different magnetic properties of materials 2D-represented by the magnetic moment dipoles, based on Harris (2002)	31
Figure 4 –	X-ray diffraction in the crystal lattice structure	34
Figure 5 –	Bragg-Brentano geometry used on powder diffraction	35
Figure 6 –	Vis-NIR spectra of different minerals commonly found in soils. CR: continuum removed.....	37
Figure 7 –	Geometric representation of first and second principal components. The first one (PC1) coincides with the major variability direction, and the second one (PC2) with the second major variability direction. The PCs are always orthogonal	39
Figure 8 –	Illustrative PCA applied to a 3-dimensional space, reducing it to 2-dimensional space.....	40
Figure 9 –	(a) Study area (red dot) in the southern Amazon region at Rio Branco Basin, Porto Velho, Rondônia, Brazil, and (b) collection points	45
Figure 10 –	Superposed EDXRF spectra of all studied samples at (a) 15 kV and (b) 50 kV. Some regions were zoomed to label the peaks	52
Figure 11 –	Concentration (%) of Al, Si, K, Ca, Ti, Mn, Fe, Zn, Sr and Zr in the studied soils. The numbers after the sample name mean the collection depth (05 for 0 – 5.0 cm and 510 for 5.0 – 10.0 cm). F1 and F2: forests collected from 0 – 20.0 cm. RB1, RB2, RB3 and CP1: pasture 1. RB4, RB5, and CSB: slash-and-burn. RB6 and CP2: pasture 2. Black dashed line stands for detection limit	54
Figure 12 –	Biplots of (a) PC1 x PC2, (b) PC1 x PC3 and (c) PC2 x PC3. Classes: F1 and F2 forests, CP1: control forest of pasture 1, CSB: control forest of slash-and-burn, CP2: control forest of pasture 2. In the biplot (c), PC2 x PC3, the classes are the heating temperatures	57
Figure 13 –	(a) Scores for PC1 x PC2, (b) scores for PC1 x PC3, (c) loadings for PC1 x PC2, and (d) loadings for PC1 x PC3. The scores classes are the collection sites (F1, F2, CP1, CP2 and CSB)	59
Figure 14 –	Measured versus predicted temperature of model 1. Prediction samples are the F1 controlled heating samples (red triangles). Calibration samples (black dots) are the controlled heating samples F2, CP1, CP2 and CSB	62

- Figure 15** – Thermal analysis of unburned samples. Dot symbols: TGA, square symbols: DTA, and plus symbols: DSC. The dashed red line indicates the mass (%) and the dashed gray line indicates the temperature for TGA analysis. (a) Forest 1 (F1), (b) forest 2 (F2), (c) pasture 1 (CP1), (d) slash-and-burn (CSB) and (e) pasture 2 (CP2)65
- Figure 16** – Munsell colors of the analyzed samples in different collection depths. RB1-RB6: burned samples. F1, F2, CP1, CP2, CP2, CSB: unburned samples. 25-750: F2 aliquots heated in muffle (25 indicates the unburned aliquot). The number indicates the temperature peak (50-750°C) that the sample was heated.....67
- Figure 17** – XRD patterns of (a) unburned and fire-burned samples (F1, F2, CP1, CP2, CSB, and RB1 to RB6), and (b) slash-and-burn sample (CSB) in different temperatures (25 to 800°C). Kaolinite (K), gibbsite (Gb), goethite (Gt), anatase (A), hematite (H) and quartz (Q) most intense peaks were labeled. The quartz peak at $2\theta = 26.7^\circ$ extrapolated the y-scale.....70
- Figure 18** – PCA biplots performed with XRD intensities. (a) PC1 x PC2, grouped by collection sites and (b) PC1 x PC2, grouped by heating temperature. The number after the mineral name indicates some other peak that characterize the same mineral in the XRD pattern.....72
- Figure 19** – Vis-NIR reflectance spectra of controlled-heat F2 aliquots, from 50 to 750°C. The 25°C aliquot was not heated.....74
- Figure 20** – Vis-NIR reflectance spectra of burned samples (RB) from pasture 1 (RB1, RB2 and RB3), slash-and-burn (RB4 and RB5), and pasture 2 (RB6)75
- Figure 21** – Vis-NIR absorbance graphs. (a) controlled-heated samples F2, ranging from 25°C to 150°C (green lines), from 250 to 450°C (blue lines) and from 550 to 750°C (red lines), Al-OH band region. (b) Fire-burned samples from pasture 1 (RB1, RB2, and RB3), pasture 2 (RB6), and slash-and-burn (RB4 and RB5) sites, Al-OH band region.....76

LIST OF TABLES

Table 1 –	Minerals and materials with their chemical formula, Fe content, and magnetic susceptibility (Dearing, 1994)	32
Table 2 –	Particle size distribution and chemical characteristics in each forest site (F1 and F2). Soil collection depth: 0-20.0 cm.....	51
Table 3 –	Certified and measured elemental concentrations and their respective relative deviation. Concentrations lower than the quantification limit are indicated as < QL	53
Table 4 –	PLS models developed with EDXRF spectra at 50 kV. LVs: number of latent variables. RMSEC: root mean squared error of calibration. RMSECV: root mean squared error of cross-validation. RMSEP: root mean squared error of prediction. CV Bias: Cross-validation bias. Pred Bias: prediction bias. R ² Cal: determination coefficient of calibration. R ² CV: determination coefficient of cross-validation. R ² Pred: determination coefficient of prediction.....	62
Table 5 –	Controlled-heat temperature and estimated temperature by PLS models with their respective relative deviations	63
Table 6 –	Main transformations and reactions with their respective mass loss in each temperature range.....	66
Table 7 –	Munsell color for each soil sample studied. YR: yellow-red. RB1, RB2, RB3, CP1: old pasture. RB4, RB5, CSB: slash-and-burn. RB6, CP2: recent pasture. F1, F2: forest. RT1-RT8: F2 heated aliquots.....	67
Table 8 –	Magnetic susceptibility measured for F2 aliquots: unburned, muffle heated at 400 °C and at 800 °C; fire-burned samples RB1 to RB6; and unburned samples CP1, CP2 and CSB. (χ_{FD}) is the frequency dependent magnetic susceptibility, and SD is the standard deviation	68

LIST OF ABBREVIATIONS

COW	Correlation Optimized Warping
CP1	Unburned pasture 1 samples
CP2	Unburned pasture 2 samples
CRM	Certified Reference Material
CSB	Unburned slash-and-burn samples
DL	Detection limit
DSC	Differential Scanning Calorimetry
DTA	Differential Thermal Analysis
EDXRF	Energy Dispersive X-ray Fluorescence
F1	Unburned forest 1 samples
F2	Unburned forest 2 samples
IAEA	International Atomic Energy Agency
NIPALS	Nonlinear Iterative Partial Least Squares
NIR	Near-infrared Spectroscopy
PC	Principal Component
PCA	Principal Component Analysis
PLS	Partial Least Squares Regression
QL	Quantification limit
RB1-RB6	Fire-burned samples from 1 to 6
RMSEC	Root Mean Square Error of Calibration
RMSECV	Root Mean Square Error of Cross-Validation
RMSEP	Root Mean Square Error of Prediction
SVD	Single Value Decomposition
TGA	Thermogravimetry Analysis
Vis-NIR	Visible Near-infrared
XRD	X-ray Diffraction
XRF	X-ray Fluorescence

CONTENTS

1	INTRODUCTION	15
1.1	MOTIVATION AND JUSTIFICATION	15
1.2	OBJECTIVES	18
2	BRIEF LITERATURE REVIEW	19
3	THEORETICAL FUNDAMENTS	21
3.1	ENERGY DISPERSIVE X-RAY FLUORESCENCE.....	21
3.2	THERMAL ANALYSIS	27
3.3	MUNSELL COLOR CHART	28
3.4	MAGNETIC SUSCEPTIBILITY.....	30
3.5	X-RAY DIFFRACTION.....	33
3.6	VISIBLE NEAR-INFRARED	35
3.7	MULTIVARIATE ANALYSIS	37
3.7.1	Data Treatments.....	41
4	MATERIAL AND METHODS	44
4.1	SAMPLING.....	44
4.2	CONTROLLED HEATING IN MUFFLE FURNACE	46
4.3	PARTICLE SIZE DISTRIBUTION AND CHEMISTRY	46
4.4	ENERGY DISPERSIVE X-RAY FLUORESCENCE.....	47
4.5	MULTIVARIATE ANALYSIS WITH EDXRF DATA	47
4.6	THERMAL ANALYSIS	48
4.7	MUNSELL COLOR CHART	49
4.8	MAGNETIC SUSCEPTIBILITY.....	49
4.9	X-RAY DIFFRACTION.....	49
4.10	VISIBLE NEAR-INFRARED	50
5	RESULTS	51
5.1	PARTICLE SIZE DISTRIBUTION AND CHEMISTRY	51
5.2	ENERGY DISPERSIVE X-RAY FLUORESCENCE.....	51
5.2.1	EDXRF Quantitative Results	52
5.2.2	Elemental Concentration	54
5.2.3	Principal Component Analysis	55
5.2.4	PLS Models and Temperature Estimation	61

5.3	THERMAL ANALYSIS	63
5.4	MUNSELL COLOR CHART	66
5.5	MAGNETIC SUSCEPTIBILITY.....	68
5.6	X-RAY DIFFRACTION.....	69
5.7	VISIBLE NEAR-INFRARED	79
6	DISCUSSION	77
7	CONCLUSIONS	81
8	SCIENTIFIC PRODUCTION	82
	REFERENCES	84
	ANNEXES	91
	ANNEX A	92
	ANNEX B	98

1 INTRODUCTION

1.1 MOTIVATION AND JUSTIFICATION

Fire is a common disturbance in ecosystems and affects physical, chemical and biological soil properties (Araya et al., 2016). There are two types of fires: prescribed (controlled fire) and wildfire (unplanned fire). Prescribed fires are commonly practiced to reduce the levels of available fuel, to minimize the extent and severity of forest fires, or to facilitate the germination and growth of some species of plants (Certini, 2005). Wildfire, in its turn, is an unplanned fire caused by lightning or other natural causes, by accidental (or arson-caused) human ignitions, or by an escaped prescribed fire (National Park Service, 2021).

Fire effects extent and duration on soil depend primarily on the burn severity, which is determined by several factors as quantity, nature and humidity of fuel, air temperature and humidity, wind speed and site topography. Identifying fire severity and soil changes after burning is essential to conduct post-fire management, e.g., the recuperation of burned areas. In addition, it is important to monitor plants and soil in scenarios where climate change is occurring, as fires tends to increase and it would directly interfere with the systems fertility (Moya et al., 2019).

Fire severity mapping may be developed by qualitative indicators (ash color, soil depth, and structure); quantitative indicators (biochemical indicators, remaining branches minimum diameter); or satellite mapping. Although coarse-resolution may be inadequate for heterogeneous ecosystems (Guerrero et al. 2007, Melquiades & Thomaz, 2016), very high-resolution multispectral imagery using an unmanned aerial vehicle (drone) demonstrated satisfactory estimation of fire severity (Carvajal-Ramírez et al., 2019).

In prescribed fires, the maximum temperature reached in soil can be monitored with thermocouples, as they can be installed before fire starts. However, for accidental or unplanned fires, when this monitoring system would not be previously installed, a methodology to predict the maximum temperature reached after the fire becomes necessary.

There are few references which correlate the maximum temperature reached in a fire event with the physical and chemical soil properties (Marcos et al., 2018; Merino et al., 2014), and further analysis is needed to establish an accurate

temperature prediction method. Thomaz, Nunes and Watanabe (2020) indicate there is a lack of studies about forest conversion to pastures and its effects on soil physical properties (temperature, moisture, density, and the infiltration of water into the soil), when compared to studies about chemical properties of soil.

The employment of multi-techniques which consider soil chemical and mineralogical properties may be useful to measure fire intensity after a burn event. Thermal analysis provides information about soil chemical structure, organic matter content and its relationship with temperature. It is possible to determine the reactions associated to mass changes, heat absorption or heat release in each reaction.

The Munsell color charts are a quick and affordable way to assess soil types, based on three properties of color: hue (basic color), chroma (color intensity) and value (lightness). It allows for direct comparison of soils. The color of the soil is correlated with the organic matter content and its mineralogy (Poppiel et al., 2020).

Magnetic susceptibility measures how a material can be magnetized when submitted to a magnetic field. The magnetic susceptibility in soils give information about the minerals found, particularly Fe-bearing minerals (Dearing, 1994). It is possible to classify different types of materials, and identify the processes of their formation or transport, for example.

X-Ray Diffraction (XRD) and visible near infrared (Vis-NIR) is frequently employed to study soil mineralogy and its crystalline structures, complementing X-ray fluorescence (XRF) measurements (Guembou et al., 2019; Javadi, Munna & Mouazen, 2021). XRF and Vis-NIR may be useful to observe which transformations occurs on minerals of burned soils, and gave some information on how these transformations are related to temperature.

Energy Dispersive X-Ray Fluorescence (EDXRF), one of the X-ray techniques widely employed in the environmental sciences, mining, chemistry, metallurgy, and archeology, has also been employed in soil science and agronomy (Weindorf et al., 2014), including fire induced changes studies. EDXRF is a qualitative and quantitative multi-element analysis technique based on the measurement of characteristic X-rays emitted by the elements present in the sample. Some EDXRF advantages over other techniques are its non-destructive character, the multi-element analysis possibility, little or no sample preparation requirement, often does not generate chemical residues, relatively simple use, speed, accuracy and relatively low cost. Disadvantages found in some cases may be due to physical matrix effects (soil

particle size, homogeneity, moisture content) and/or interference and enhancement effects depending on sample composition (Peinado et al, 2010). In recent years, data acquirement has become more sophisticated due to the improvement of computers and detection instruments. The large amount of information, often complex and varied, gave rise to multivariate data analysis (Ferreira et al., 1999). The multivariate analysis application in experiments involving spectroscopy is straightforward, since the number of variables in a single spectrum can easily reach several thousand. Furthermore, it is usually necessary to determine some sample characteristic which is not directly measured by means of the spectrum. The EDXRF spectrum, for example, carries implicit information about soil chemical characteristics (elemental composition, organic matter content), which are reflected in the intensity of characteristic peaks, scattering peaks, and in the background profile. By using multivariate analysis, it is possible to extract such implicit information and construct informative models.

The first attempt to perform a post-fire estimation with EDXRF was conducted by Melquiades and Thomaz (2016), with a Inceptisol and controlled muffle heating. The authors found such estimation was feasible. Afterwards, Rocha et al. (2019) conducted a study with a Inceptisol. Univariate and multivariate analysis were employed to estimate the maximum temperature reached in fire-burned samples. The best result ($R^2 = 0.90$) was achieved using the EDXRF spectra scattering region, with an estimated relative deviation in temperatures ranging from 8% to 25%. Multivariate analysis presented better results than univariate regression. In the current study, multivariate analysis and multi-techniques measurements are presented. Such new steps aim to describe the statistical approach, improving the models and going further in the investigation of what was concluded in the previous studies.

From the simplest ones, as visual analysis at field, to the most complex ones, as laboratory analysis methods, literature presents different techniques to measure fire effects in soil. It is possible to measure important soil properties by using spectroscopic techniques coupled with multivariate analysis, but there is still a need for investigation and methodology improvement. This study was conducted with Amazon soils. Due to its heterogeneity and complexity, more studies concerning the region are necessary, for what we strive to fill such a gap in this research.

Considering the importance of studying the fire effects in soil and the analytical methodologies applied nowadays, some hypotheses arise: changes in soil structure, composition, and the relation of these changes with fire intensity can be

determined by spectroscopic techniques; it is possible to estimate the maximum temperature reached in soils during fire by using multivariate calibration with spectroscopic data; the data acquired with different techniques may improve the soil characterization and the maximum temperature estimation models.

1.2 OBJECTIVES

General objective:

Estimate the maximum temperature reached in Amazonian soil during fire by using a multivariate calibration model with EDXRF data and other techniques (thermal analysis, Munsell color chart, magnetic susceptibility, XRD, and Vis-NIR).

Specific objectives:

Employing EDXRF in Amazonian soils to acquire the elemental concentration and the spectrum of each sample to develop the temperature estimation models post-fire.

Performing thermal analysis to understand the reactions and transformations in soil due to heating.

Using the Munsell color chart to characterize the color of the soil collected from different sites and at different temperatures.

Measuring the magnetic susceptibility to verify the magnetic behavior of the soil from different sites and when it is submitted to different temperatures.

Performing XRD and Vis-NIR to determine the soil mineralogy and its changes due to heating.

2 BRIEF LITERATURE REVIEW

Fire effects studies aim at determining soil physical, chemical and biological changes caused by burning events. Such changes can be found, for instance, in soil pH, composition, organic matter, color, and structure. Currently employed methodologies to measure these changes can be simple visual field analysis, field analysis using *in situ* equipment, or a more complex analysis such as laboratorial methodologies, which often uses more complicated preparation of samples.

Heat-induced changes in soil are usually reported in its superficial layer, between 0 and 5.0 cm (Badía et al., 2017), because soil is a poor heat conductor (DeBano et al., 1998). Some exceptions (fire-induced changes at depth > 5.0 cm) can be detected in soils burned under masticated fuel, i. e., forests treated mechanically by reducing vegetation into small chunks (grind, chip or break brush, small trees, and slash them into small pieces) to avoid catastrophic fires (Busse et al., 2005).

Forest conversion is a constant process in the Amazonian southern portion. Several impacts on soil and aquatic systems e.g., biogeochemical cycles, may be caused by such forest conversion process (Thomaz et al., 2020). Predicting the maximum temperature reached in soil and the immediate, cumulative and possibly long-term persistence effects on soil properties is of utmost importance. Several studies have focused on the long-term effect of land conversion in soils with few considerations about fire effects (Moraes et al., 1996; Souza et al., 2018; Melo et al., 2017; Thomaz et al., 2020).

Carvalho et al. (2018) used multivariate analysis to characterize different types of land use changes in an Oxisol in southern Amazon. Physical, chemical and biological attributes were analyzed in laboratory, and the results showed the data grouping into two distinct sets: one due to anthropic preparation operations, and other due to soil liming. These results demonstrated that investigating fire effects after a burning event (accidental fires or prescribed fires for agricultural purposes) is essential to understand soil behavior and to propose correction procedures for fire induced changes in soil.

Melquiades and Thomaz (2016) conducted the first attempt to perform a post-fire estimation with EDXRF with controlled muffle heating and multivariate analysis. Rocha et al. (2019) conducted a study comparing univariate and multivariate

analysis, and concluded that the last one can provide better results.

Araya et al. (2016) studied soils in Sierra Nevada, California, and observed significant changes in soil crystalline structure in 250 °C to 450 °C range, mainly due to organic matter loss and transformation of gibbsite and kaolinite phases. They used muffle burn simulation and characterized the samples using Munsell Color Chart, XRD and laboratory chemical methods.

Souza et al. (2018) carried out a study concerning physical, chemical, and mineralogical attributes of a representative group of soils on Amazon. They performed laboratory analysis and XRD measurements in three different heating temperatures (25, 300 and 500 °C). The authors found that kaolinite is the predominant mineral in the clay fraction in Amazon soils in Pará. They claim that due to the great extent and heterogeneity, there is still scarce research carried out in the region.

Vibrational spectroscopic methods as near-infrared reflectance (NIR) spectroscopy combined with multivariate statistical analysis suggest that temperature estimation is feasible (Guerrero et al., 2007; Arcenegui et al., 2010). Pérez-Bejarano and Guerrero (2018) employed NIR data combined with partial least squares regression (PLS) to estimate the maximum temperature reached during fire. They confirmed the importance of sample set variability used to calibrate the models. Guerrero et al. (2007) used the PLS calibration with NIR data to build prediction models for maximum temperature reached in soil after fires. For nonlocal models (prediction done with soil samples collected from a different site than the samples employed in the calibration set), the correlation coefficient R^2 ranged from 97% to 99%, and the RMSEP from 26.0 to 37.4°C. RPD values were always above 5.7, which was considered a high accuracy.

3 THEORETICAL FUNDAMENTS

3.1 ENERGY DISPERSIVE X-RAY FLUORESCENCE

X-rays were discovered in 1895 by Wilhelm Conrad Röntgen in Wurzburg, Bavaria, Germany, while he was working with cathode-ray tubes (Martins, 1998). At that time, the interesting work by Hertz and Lenard involving electrical discharges in vacuum tubes would have motivated his research. Röntgen wrapped a Crookes tube with black cardboard, and with laboratory lights turned off he observed a piece of paper near the experiment glowing, as current flowed through the Crookes tube. The piece of paper had barium platinocyanide in its composition, a fluorescent material. Turning off the current, Röntgen checked a dark shadow on the barium platinocyanide paper. By placing other objects between the tube and the paper, he realized incoming rays from the Crookes tube had a high penetration capacity. The physicist gave them the name “X-rays”, because of not knowing their nature. Röntgen received the first Nobel Prize in Physics, in 1901, due to such discovery.

In a Crookes tube, electric current flow between two electrodes. Positive ions are produced and bombard the cathode (negative electrode) due to the potential difference established along the tube. Then, electrons are emitted from the cathode and acquire speed, hitting the target. The target can be the anode (positive electrode), tube wall or a metallic sheet attached to the anode (Pereira, 2012). Accelerated electrons colliding against a target may generate X-rays, as the electrons slowdown in the target.

The collision of electrons against the target can produce two types of X-rays: braking radiation (also known as bremsstrahlung) and characteristic radiation. Braking radiation results from the deceleration of an incident electron by the protons in the target (Coulomb interaction). This interaction causes a deflection in the trajectory and the incident electron loses speed, what causes a partial or total loss of its kinetic energy. The difference between initial and final energy is emitted mainly as heat, but also as X-rays. Braking radiation produces a continuous spectrum. Characteristic radiation, in its turn, may occur when the target is ionized by the incident electrons through photoelectric effect. In the process, incident electrons interact with electrons of inner shells of target atoms. If the target electron receives enough energy and is ejected, a vacancy will remain in such shell. This vacancy may be filled by an electron

from one of the outermost electrosphere layers, emitting the exceeding energy as X-rays. Such X-ray will have a discrete energy which value is equal to the energy difference between the upper and lower layers involved in the process. As each atom has different energy values between its electron shells, the characteristic X-ray emitted can be interpreted as a “fingerprint” of each element.

X-ray phenomenon became important for natural sciences and also for medical field due to its varied practical applications. Today, it is known that X-rays are a type of high-energy electromagnetic radiation, ionizing, originated in the transitions of electrons in the innermost levels of an atom, with a wavelength ranging from 0.1 to 100 Å (Oliveira, Ribas & Souza, 2009).

If a beam of electromagnetic radiation strikes a material and interacts with its atoms, such beam will be attenuated by absorption or scattering. From a few keV to tens of MeV, there are several processes which may occur in the radiation interaction with matter, as elastic scattering (Rayleigh, Thomson), photoelectric effect, inelastic scattering (Compton), and pair production (Burcham, 1974).

In elastic scattering, there is no exchange of energy, nor ionization of atoms. In this phenomenon, incident radiation is treated as a wave (Yoshimura, 2009). Incident oscillating electric field interact with bounded electrons in the material, which will acquire the same moving frequency of incident electrons. Therefore, bounded electrons will radiate in the same energy as incident radiation.

Photoelectric effect, in its turn, occurs when all the energy of the incident photon ($h\nu$, according to the corpuscular theory) is transferred to a bound electron of the atom, which is ejected with kinetic energy T equal to:

$$T = h\nu - E_K \quad (1)$$

T is the difference between the incident photon energy ($h\nu$) and the E_K binding energy of the K-shell electron, for example. The atom becomes ionized, and the vacancy left by the ejected electron is occupied by another electron from an outer shell, in order to de-excite the atom. The de-excitation process can occur through two different effects: the production of X-rays by fluorescence or the emission of Auger electrons. In the first one, X-rays are emitted with energy equal to the energy difference between the electronic levels involved (characteristic X-rays). In the second one, the energy that would be emitted as an X-ray is converted into energy for another electron,

which is then emitted from the atom.

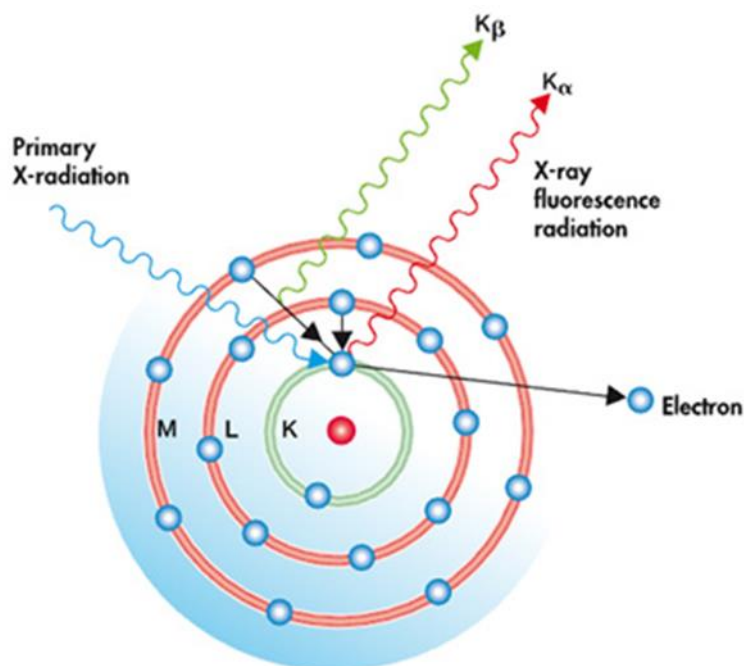
In Compton or inelastic scattering, the incident photon is scattered by an electron practically free from the target material. As part of its energy is lost (transferred to the electron), by conservation of linear momentum the photon acquires a certain angle in relation to its initial propagation direction. Its final energy, E_f , is given by:

$$E_f = h\nu' = \frac{h\nu_0}{\frac{1 + h\nu_0}{mc^2} * (1 - \cos\theta)} \quad (2)$$

with ν_0 the initial frequency of the photon, ν' the final frequency, h the Planck's constant, m the electron rest mass, c the light speed, and θ the angle formed between the initial and final propagation direction of the photon. The electron which interacted with the photon, called the recoil electron, is ejected with kinetic energy equal to the energy transferred by the photon minus its binding energy.

Energy Dispersive X-Ray Fluorescence (EDXRF) is a spectroscopic technique based in the photoelectric effect and consists in detecting characteristic X-rays emitted by the sample. Figure 1 schematically shows the fluorescence phenomenon.

Figure 1 - Representation of photoelectric effect and characteristic X-ray fluorescence radiation in an atom



Source: <https://wpo-altertechnology.com/xrf-x-ray-fluorescence-spectroscopy-hi-rel-parts/>.

Retrieved: May 23, 2022.

In this technique, the emitted X-rays are separated according to their energy. The process can be summarized in three parts: (i) excitation of the elements which compose the sample through photoelectric effect, (ii) emission of characteristic X-rays in the de-excitation process of atoms and (iii) detection of X-rays to be displayed in a spectrum with intensity in function of energy (Nascimento Filho, 1999).

In order to emit X-rays, the sample must be excited. It can be done in several ways: excitation by accelerated particles (such as electrons, protons or ions), X-ray excitation, alpha particles, negative beta particles or gamma rays emitted by radionuclides, or X-ray tubes.

For the characteristic X-rays production, it is necessary to remove electrons from the innermost layers of the atoms in the sample. Therefore, the energy of the excitation radiation must be greater than the binding energy of the electron in the atom. The minimum energy to rip the electron from the atom is called the absorption cutoff. Such energy can be roughly calculated for the electrons in the K and L shells from the atoms of an element, using Bohr's atomic theory for the hydrogen atom and hydrogenoid atoms with Moseley's experimental considerations, according to the

equation:

$$E = \frac{me^4(Z-b)^2}{8\varepsilon_0^2h^2n^2} \quad (3)$$

where E is the electron's binding energy (in Joules), m is its rest mass, e is the electric charge, Z is the atomic number of the X-ray emitting element, b the Moseley constant ($b=1$ for the K shell and $b=7.4$ for the L layer), ε_0 the electrical permittivity in a vacuum, and h the Planck's constant at the principal quantum number of the electronic level.

Substituting the values for the constants according to the international system of units (SI) and knowing that $1 \text{ eV} = 1.6 \times 10^{-19} \text{ Joules}$, the previous equation can be written as:

$$E = 13,65 \frac{(Z-b)^2}{n^2} \quad (4)$$

and it can be seen that the binding energy E of the electron is directly proportional to the atomic number squared of the element.

After the ionization of the atom, an electron from an outermost shell will fill the vacancy formed, emitting a characteristic X-ray according to the equation:

$$E_X = E_{ni} - E_{nf} \quad (5)$$

with E_X the characteristic X-ray energy, E_{ni} and E_{nf} the electron energies at the initial and final levels, respectively. This is why the observed energy (characteristic X-ray) is unique for each element.

The X-rays emitted by an element have the following denomination:

- K, for transitions from higher levels to level K: $K\alpha$ for transitions $L \rightarrow K$ and $K\beta$ for transitions $M \rightarrow K$;
- L, for transitions from higher levels to level L: $L\alpha$, for transitions $M \rightarrow L$ and $L\beta$ for transitions $N \rightarrow L$.

Sometimes, the energy that would be emitted in the form of characteristic X-rays is converted into the energy of another electron. This electron is ejected from the atom with characteristic energy, and is called an Auger electron. Thus, it is possible to define the fluorescence yield as the number of X-rays effectively emitted

in relation to the number of vacancies that were produced in a given layer. For the K layer, a low fluorescence yield can be observed for lighter elements, up to approximately $Z < 20$. For layer L, elements with $Z < 50$ present low efficiency, as well as elements with $Z < 80$ for layer M.

Regarding to the X-rays detection, the EDXRF emerged in the early 1970s with the development of the Si(Li) semiconductor detector, which is capable of separating X-rays of nearby energies. This type of detector produces electronic pulses proportional to the X-ray energies, which are selected by the computer system and recorded in the form of counts versus energy spectra. There is a simple relationship between the intensity of a characteristic X-ray and the concentration of the respective element in the sample. When using a monoenergetic beam for excitation, the equation is given as follows:

$$I_i = C_i \cdot S_i \cdot A \quad (6)$$

where I_i is the characteristic X-ray intensity, C_i is the elemental concentration in the sample for the i element, S_i is the elemental sensitivity for the i element, and A is the absorption factor.

The sensitivity S_i depends on the geometry of the system, the detector efficiency and also on a set of fundamental physical constants, namely: the elemental absorption coefficient for the photoelectric effect on the incident radiation energy, the fluorescence yield for K X-rays, the fraction of K photons emitted as characteristic $K\alpha$, and the jump ratio (probability of removing electrons from all layers in relation to the probability of L, M, and other layers). The absorption factor A relates the density, thickness and total absorption coefficient of the sample matrix.

The spectrum generated in EDXRF contains an approximately continuous line under the peaks. This continuum is a consequence of the interactions of scattering radiation from the sample with the detector, in addition to the characteristic radiation emitted by the elements. Thus, under each peak in the spectrum there is an area, called background, which belongs to the continuum. The detection limit (DL_i) and the quantification limit (QL_i) of an element are directly related to the background (BG_i) according to the equations:

$$DL_i = 3\sqrt{BG_i} \quad QL_i = 10\sqrt{BG_i} \quad (7)$$

They can be expressed as elemental concentrations (ppm, for example), by dividing the value of DL_i or QL_i by the elemental sensitivity S_i .

The Compton correction may be applied to elemental intensities to correct matrix effects as absorption, grain size effects and variation in tube voltage and current. It is performed by calculating the ratio between the intensity of the element and the peak intensity of Compton-scattered radiation.

$$I_{Corrected} = \frac{I_{Element}}{I_{Compton}} \quad (8)$$

Usually, for specimens made up of oxides, the scattered intensity is usually intense and can be measured with sufficient precision in a relatively short time (Van Grieken & Markowicz, 2002).

3.2 THERMAL ANALYSIS

In this study, three thermal analysis techniques were employed: thermogravimetry analysis (TGA), differential thermal analysis (DTA), and differential scanning calorimetry (DSC).

The first one is a technique in which the sample weight is measured as a function of temperature using a high-precision thermobalance within the furnace (Plante, Fernández & Leifeld, 2009). The sample weight is continuously measured during the heating program and the percentages of mass loss can be calculated from the acquired data.

The second one, DTA, is a technique that records the temperature difference between a sample and a reference standard (often inert). The sample and the reference sample are submitted to an identical atmosphere in a controlled heating process. The temperature difference is plotted against time or temperature.

The last technique, DSC, measures the energy added to an unknown sample and to a reference standard sample as a function of the temperature. DSC has two classes of instruments based on their operation principles: heat flux or power compensation. Heat flux DSC measures a temperature difference between the sample and the reference standard and transforms the signal into a heat flow rate. Power compensation aims to establish a near to zero difference temperature between the

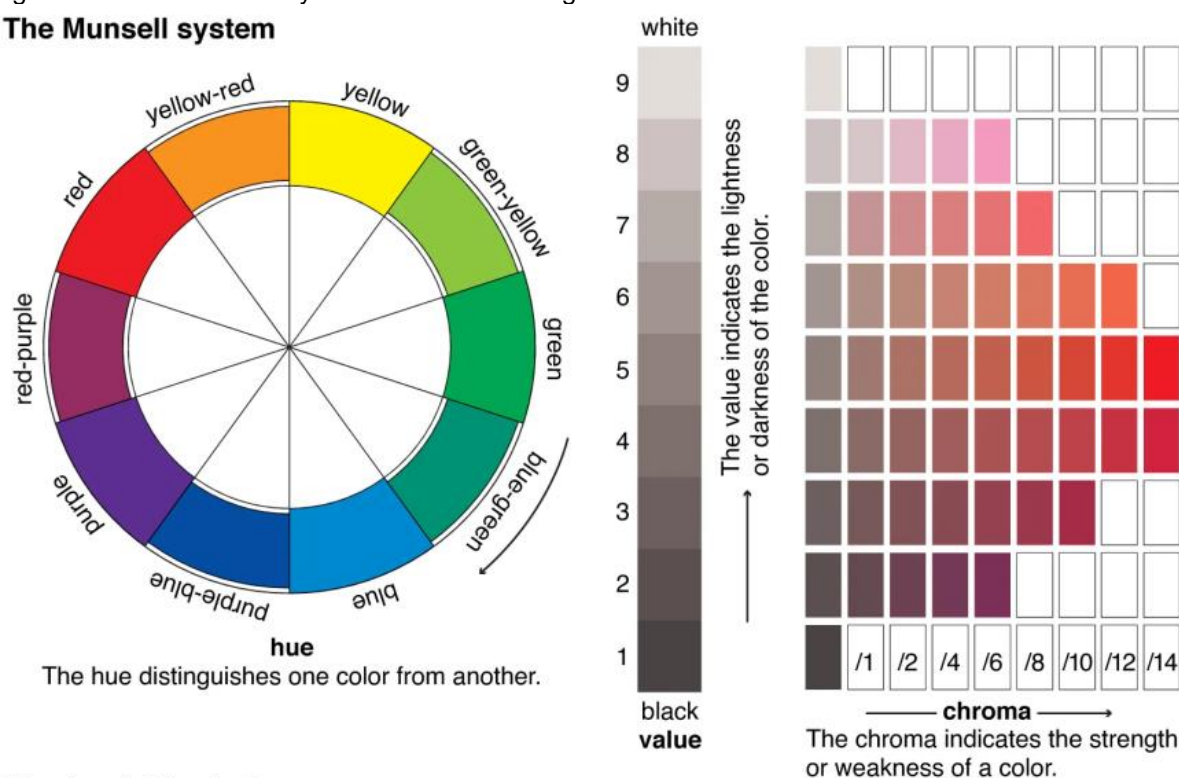
sample and the reference standard while they are submitted to the same heating program. The differential power input, which compensates the temperature differences, is recorded and the energy required to do this is a measure of the enthalpy or heat capacity changes in the samples relative to the reference standard.

The combination of DTA and DSC techniques is important in the thermal analysis because some reactions are not associated with changes in mass (and then, undetectable by TGA), but all these reactions absorb or release heat and thus are detectable by DTA/DSC.

3.3 MUNSELL COLOR CHART

Methods for describing and classifying colors date back hundreds of years. The pioneer in this field was the chemist Chevreul (1786 – 1889), with an excellent work using dye and pigment mixture, but that did not influence the practical users because his color system was difficult to retain in one's memory. The scientist Helmholtz (1821 – 1894) stated that the color possesses three simple attributes or dimensions. His work remained buried for a time, until in the late nineties, when the instructor of art, Mr. Albert Munsell (1858 – 1918), decided to illustrate the three dimensions of color graphically on a color sphere. He planned a series of color charts presenting carefully standardized scales of "hue", "value" and "chroma" (Cooper, 1929). The first color chart appeared in 1905, with suggesting application to the field of art education. In 1913, fifteen standard color charts were assembled in the "Atlas of the Munsell Color System". The Atlas has been replaced by the "Munsell Book of Color" and combines practical teaching experiences with the rigorous investigation of scientists. Figure 2 presents the Munsell Color System.

Figure 2 - Munsell Color System for color notating

The Munsell system

© Encyclopædia Britannica, Inc.

Source: <https://www.britannica.com/science/Munsell-color-system#/media/1/397642/148652>. Retrieved: May 22, 2022

Hue: the first characteristic the eye detects. Passing a ray of sunlight through a prism breaks the light into red, yellow, green, blue, etc., and this distinguishing of any color indicates the hue. In notating a color, its hue is indicated by the initial letter or letters of the color (R for red, YR for yellow-red, etc).

Value: between black and white, it can be various degrees of light strength, ranging from the darkest gray to the lightest gray. The colors can be seen at these various intermediate levels of light strength. This variation is called value, and indicates how light or dark a color is. Pure black is indicated as 0 and pure white as 10. In notating a color, the value comes after the hue letter, p. e., R 5/, for a red of a lightness about half-way between black and white.

Chroma: hue is the name of a color, value is the amount of light, and chroma is the degree of strength in a color. Two colors may have the same hue and value, but different chroma. For instance, one red of half-way value may be a strong red and the other a weak, grayish red. Chroma is the intensity of the color, its saturation. In notating a color, the chroma comes after the slash, p. e. R 5/5. So, the general notating is hue value/chroma.

The Munsell Color Chart is employed in the soil science

conventionally, and provide information about the mineralogical soil phases. The main factors that influence soil color are the organic matter (causes darkness, decreasing Munsell value and chroma) and the mineralogy (modifies the hue) (POPPIEL et al., 2020).

3.4 MAGNETIC SUSCEPTIBILITY

During the 1970s and 80s, scientists realized that magnetic properties were useful for describing and classifying all types of environmental materials (Dearing, 1994). All matter like rocks or soil, the dust in the air, river water or leaves on a tree, etc., is affected by a magnetic field. The magnetic effect may be weak or negative, but exists and can be measured easily. Magnetic susceptibility measures the “magnetizability” of a material, and enables to identify the Fe-bearing minerals, classify different types of materials, identify the processes of their formation or transport, be diagnostic of specific processes (like burning soil or soil waterlogging), and create “environmental fingerprints” for matching materials.

Magnetism is controlled by the inherent forces or energies created by the electrons of the atoms. The way in which different electrons are arranged and their movements determine the total magnetic energy or moment of the atom. Atoms make up molecules, molecules make up materials. The overall type of magnetic behavior of a material is defined by the configuration and interaction of all the electron motions in all atoms. There are five kinds of magnetic behavior: ferromagnetism, ferrimagnetism, canted antiferromagnetic, paramagnetism and diamagnetism. The first three are able to remain magnetized in the absence of a magnetic field and may be identified using remanence measurements.

Ferromagnetism: the magnetic moments are highly ordered and aligned in the same direction on the material (p. e. pure Fe, Co, Ni), the magnetic susceptibility is very high, but will not normally be found in the environment. Canted antiferromagnetic: the crystal structures are aligned but have opposing magnetic moments, and the forces virtually cancel each other. The magnetic susceptibility is low. Common materials with such behavior are goethite and hematite. Ferrimagnetism: the most important category in natural materials, the magnetic moments are strongly aligned, but exist as two sets of opposing but unequal forces controlled by the crystal lattice structure of certain minerals (p. e. magnetite, and other Fe-bearing minerals).

Paramagnetism: the magnetic moments arise mainly due to Mn and Fe ions, and are aligned only in the presence of a magnetic field. Weaker magnetic susceptibility values are obtained in such materials (p. e. biotite and pyrite). Diamagnetism: the resulting magnetic moment is zero. External magnetic field interacts with the orbital motion of electrons to produce weak and negative values of magnetic susceptibility (p. e. quartz, kaolinite, calcium carbonate, organic matter, water).

The sum of all the magnetic susceptibilities cited above is the magnetic susceptibility of the material. Normally, the diamagnetic component is negative, very weak, and can be ignored. Exceptions to this are where the sample is almost all water, quartz or organic matter. Figure 3 illustrates the five magnetization types, and Table 1 present the values of magnetic susceptibility for some materials and minerals.

Figure 3 - Different magnetic properties of materials 2D-represented by the magnetic moment dipoles, based on Harris (2002)

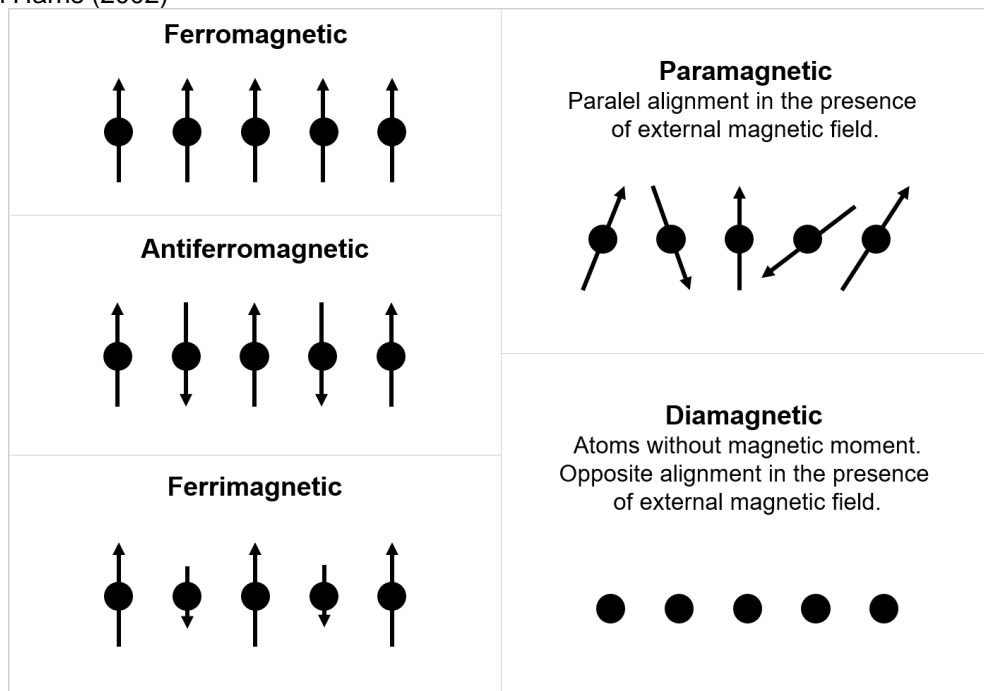


Table 1 - Minerals and materials with their chemical formula, Fe content, and magnetic susceptibility (Dearing, 1994)

Mineral or material	Chemical Formula	Fe (%)	Magnetic Susceptibility ($10^{-8} \text{ m}^3 \text{ kg}^{-1}$)
Ferromagnetic			
Iron	Fe	100	27600000
Cobalt	Co	0	20400000
Nickel	Ni	0	6885000
Ferrimagnetic			
Magnetite (0.012 – 0.069 μm)	Fe_3O_4	72	44000 - 111600
Magnetite (1 – 250 μm)	Fe_3O_4	72	39000 - 71600
Maghemite	$\gamma\text{-Fe}_2\text{O}_3$	70	28600 - 41000
Canted antiferromagnetic			
Hematite	$\alpha\text{-Fe}_2\text{O}_3$	70	27 - 169
Goethite	$\alpha\text{-FeOOH}$	63	35 - 125
Paramagnetic			
Ilmenite	FeTiO_3	37	170 - 200
Olivine	$(\text{Mg, Fe})\bullet 2\text{SiO}_4$	<55	1 - 130
Biotite	Mg, Fe, Al Silicate	31	5 - 95
Diamagnetic			
Quartz	SiO_2	0	-0.58
Organic matter	C, H, O, N	Variable	-0.9
Water	H_2O	0	-0.9
Kaolinite	$\text{Al}_4\text{Si}_4\text{O}_{10}(\text{OH})_8$	0	-1.9

The measurement of magnetic susceptibility is extremely simple, as it can be made on all materials, the measurements are safe, fast and non-destructive, can be made in the laboratory or field with minimal training, and complement many other types of environmental analyses. A sensor creates a weak magnetic field from an alternating current (AC), p. e. a solenoid, and detects the magnetization of the material lying in it. Different materials will affect the magnetic field in different ways. The magnetic susceptibility is the ratio between the magnetization of the material and the magnetic field, and is calculated relative to air, which is used to zero the meter. The mass specific magnetic susceptibility is calculated using the mass (m) of the sample and the magnetic susceptibility measured at low frequency (χ_{LF}), according to the equation:

$$\chi_{LF} = \frac{10 * \kappa_{LF}}{m} \quad (9)$$

The percentage of frequency dependent magnetic susceptibility (χ_{FD}) can be defined by the equation 10, where χ_{HF} and χ_{LF} are the magnetic susceptibility at high and low frequency, respectively.

$$\chi_{FD} = 100 * \frac{\chi_{LF} - \chi_{HF}}{\chi_{LF}} \quad (10)$$

Superparamagnetic crystals that are < 0.03 mm have a magnetic behavior which shows rapid change over time. They lose the induced magnetization received in a very short period of time; about 1/10000th of a second. It occurs due to their natural thermal energy, which is sufficiently strong to overcome the energy induced by a magnetic field. The measurement of frequency dependent susceptibility exploits this phenomenon by measuring a sample twice, at two different magnetization frequencies (Dearing, 1994).

3.5 X-RAY DIFFRACTION

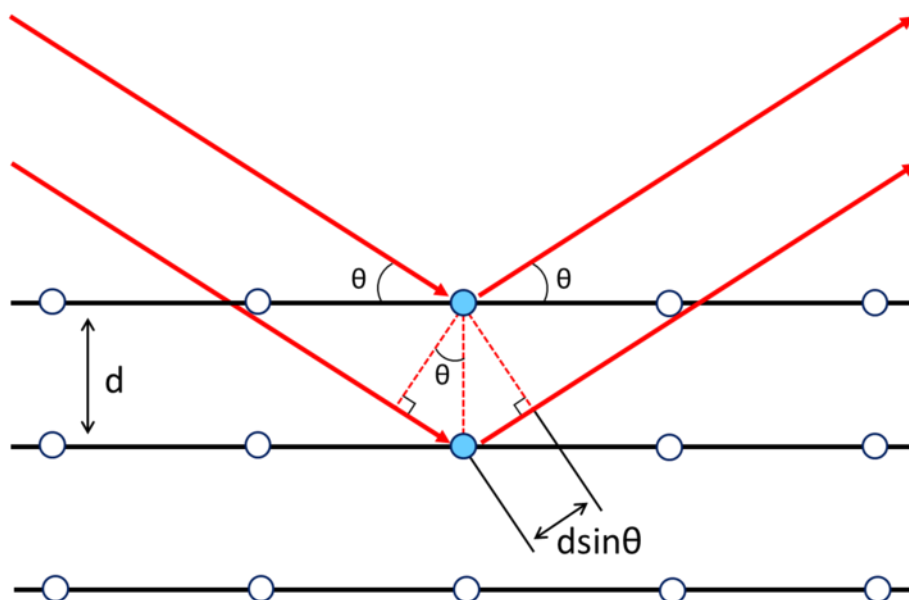
Wilhelm Roentgen studied the X-rays in 1895 and a key question that needed to be answered was whether these rays were made up of corpuscles or waves. An experiment was proposed by Max von Laue to show that, if they were wave-like, X-rays should be diffracted by a crystal. In April 1912, Laue, Paul Knipping, and Walter Friedrich obtained spots on a photographic plate when an incident X-ray beam reached a copper sulfate crystal (they obtained even better photographs with ZnS and diamond in other subsequently tries). This demonstrated, for the first time, that X-rays can be diffracted by crystals and should be treated as waves (Glazer, 2013). Laue received the Nobel Prize for this study in 1914. However, he was unable to account for the exact arrangement of the spots, mainly because he made some incorrect assumptions about the diffraction process and the crystals structures.

William Henry Bragg was convinced that X-rays were particle-like in nature, and so, with his son William Lawrence Bragg, set about showing how Laue's patterns could be explained by channeling of particles through 'avenues' within the crystals. However, W. L. Bragg became convinced that the correct explanation was

actually the one in which X-rays consisted of waves rather than particles. In 1912, W.H. Bragg realized the importance of his son insight, and then father and son collaborated to study the new field. The W.L. Bragg paper subsequently appeared in print in February 1913 and heralded a revolution in the scientific understanding of crystals and their atomic arrangements, being the beginning of X-ray crystallography. This study area led to many of the most important scientific achievements of the last century, and these continue to the present day. Now, X-ray diffraction is a common technique in the study of various crystal structures in chemistry, geology, biology fields, among others.

X-ray diffraction occurs when a primary X-ray beam with a wavelength similar to the distance between the atoms is elastically scattered by the electrons of the atoms in the crystal. A diffracted beam is produced with certain geometrical conditions, as can be seen in Figure 4. The horizontal lines represent a 2D crystal lattice with imaginary planes. Two arrows downing from the left side and going up to the right side represent the X-ray beams.

Figure 4 - X-ray diffraction in the crystal lattice structure



Source: <https://www.nextpng.com/en/transparent-png-zach>. Retrieved: Oct 13, 2020

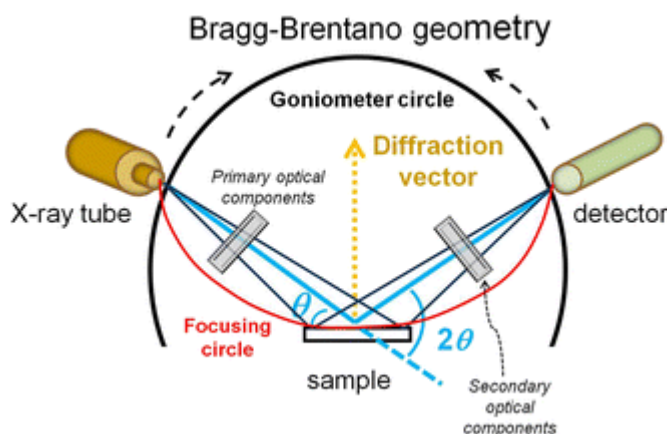
The Bragg's law can be used to calculate the angle where constructive interference from X-rays scattered by the atoms takes place resulting in a diffraction peak:

$$n\lambda = 2d\sin\theta \quad (11)$$

In this equation, n is any integer, λ is the X-ray wavelength, d is the interplanar spacing in the crystal and θ is the diffraction angle measured by the goniometer on the diffractometer (Yale University, 2020). Constructive interference occurs when the difference ($2d\sin\theta$) traveled by the bottom X-ray beam in Figure 4 is equal to $n\lambda$.

The most used geometry of powder diffractometers is the Bragg-Brentano para-focusing geometry. Although this geometry requires precise alignment and careful sample preparation, it offers a high resolution and high beam intensity analysis. Figure 5 shows the Bragg-Brentano scheme.

Figure 5 - Bragg-Brentano geometry used on powder diffraction



Source: Domenéch-Carbó & Osete-Crotina, 2016

The X-rays produced by the X-ray tube pass through the primary optical components, interact with the sample, and are diffracted by the crystalline structure. Then, the diffracted X-rays pass through the secondary optical components and reach the detector. The X-ray tube and the detector move around the sample to record the intensities as a function of the diffraction, generating a diffractogram.

The crystal lattice structure determines the peaks position in the diffraction pattern, whereas the diffraction intensity is determined by the arrangement and by which atoms are on the lattice planes.

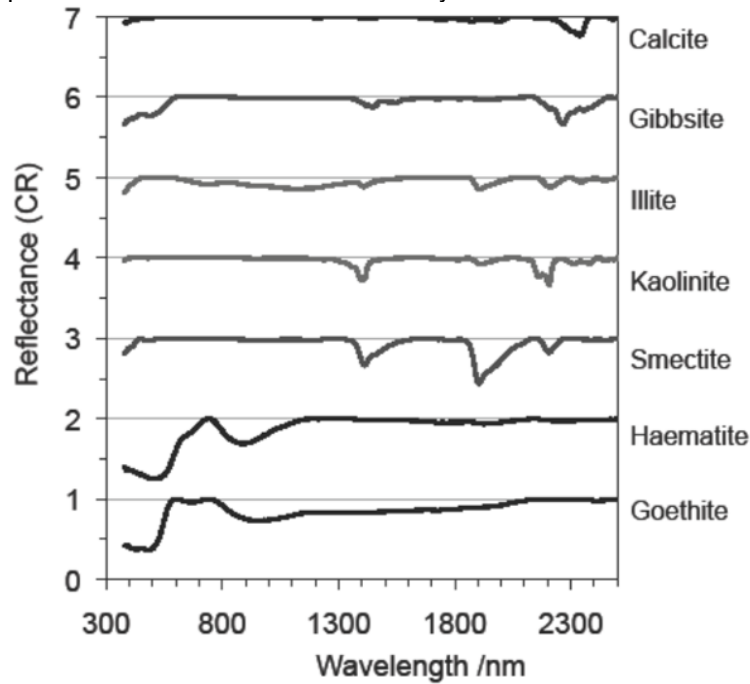
3.6 VISIBLE NEAR-INFRARED

First reported in 1800 by Frederick William Herschel, Near Infrared Spectroscopy (NIR) is a type of vibrational spectroscopy widely applied in agricultural

and environmental studies. Energy employed ranges from 2.65×10^{-19} J to 7.96×10^{-20} J, which corresponds to wavelengths from 750 nm to 2500 nm. Such energy can promote molecules (containing C-H, N-H, S-H or O-H bonds) to their lowest excited vibrational state through a fundamental vibrational transition (Pasquini, 2003). Therefore, it is possible to acquire qualitative and/or quantitative information from the interaction of near-infrared electromagnetic waves with the sample constituents. Measurements performed with NIR are fast (one minute or less per sample), non-destructive, and non-invasive, with minimum sample preparation demands. Only in the eighties such technique started to get attention, mainly by instrumental improvements associated with spectral data acquisition and their treatment on computers with Chemometrics.

NIR spectrum originates from radiation energy being transferred to atoms as mechanical energy. In a given wavelength range, some frequencies will be absorbed by the sample, some will not be absorbed, and others will be partially absorbed. Measurement modes in NIR spectroscopy can be transmittance, transreflectance, diffuse reflectance, interactance and transmittance through a scattering medium. Diffuse reflectance measurement of solid samples is a distinguishing measurement mode employed in NIR spectroscopy. In such method, scattering and absorbance by the sample contribute to the signal intensity. Figure 6 presents some Vis-NIR spectra of common minerals found in soils. CR means that the continuum was removed.

Figure 6 - Vis-NIR spectra of different minerals commonly found in soils. CR: continuum removed



Source: Stenberg et al., 2010

It is possible to estimate the concentration of a given substance in a sample or to estimate a property when such characteristics reflect significant changes in spectra features. Equation 12 is used for analytical methods based on reflectance measurements.

$$f(C) = \text{Log} \left(\frac{1}{R} \right) \quad (12)$$

C is the concentration and R is the reflectance. R is obtained by the ratio between the intensity of radiation reflected by the samples, and the same quantity reflected by a non-absorbing material over the whole spectral range of measurement. Samples grain size may affect the reflectance spectrum. Reducing grains size to get a more uniform sample increases signal distinguishment.

3.7 MULTIVARIATE ANALYSIS

The experimental data acquirement reached a high sophistication level, especially by using electronic instruments that may generate and register a large quantity of data in a relatively small-time interval. However, just by observing the raw data in big matrices may be not enough to interpret the important information. It is necessary to have a tool to manage the multivariate data and extract such information

from the experiment (Ferreira, 2015).

Once collected, the data is organized into a matrix X . Each line corresponds to a sample and each column to a variable. Therefore, each matrix element x_{ij} corresponds to the j^{th} variable measured value for the i^{th} sample. The X matrix can be represented by $X_{I \times J}$, where I is the total number of samples and J the total number of variables.

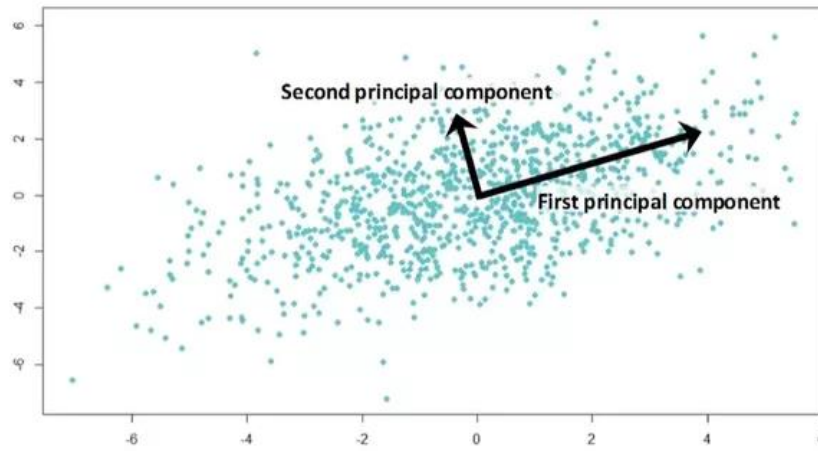
$$X_{I \times J} = \begin{bmatrix} x_{11} & \cdots & x_{1j} & \cdots & x_{1J} \\ \vdots & & \ddots & & \vdots \\ x_{I1} & \cdots & x_{Ij} & \cdots & x_{IJ} \end{bmatrix} \quad (13)$$

The line-space (samples) will have dimension I , while the column-space (variables) dimension J . In spectroscopy techniques, the number of variables can easily reach thousands as they are related to the intensities of the electromagnetic radiation evaluated in each wavelength range or energy range

A fundamental exploratory method for multivariate data investigation is Principal Component Analysis (PCA). By using this methodology, it is possible to explore, compare and interpret the differences between samples (even slightly differences).

This method is substantiated in the concept of correlation between the variables. For instance, two different variables in a data matrix can be highly correlated with each other, which indicates the existence of a latent factor that makes these two variables increase or decrease together. Therefore, it is possible to find a smaller number of variables (latent factors) that almost be efficient to describe the original data. To do this, the PCA compress the data and project them into a lower dimensional space. Such projections are done by a linear transformation, and the relationship between the samples are not changed. As result, a new variable set is defined with desirable and specific properties. These new variables (or axis) are called Principal Components (PC), also known by factors or eigenvalues. The first Principal Component, PC1, coincides with the data major variability direction. The second, PC2, should be perpendicular to PC1 and in the second major variability direction of data. Figure 7 geometrically illustrates this process. Once the number of PCs is defined, the original data is projected in the space generated by them.

Figure 7 - Geometric representation of first and second principal components. The first one (PC1) coincides with the major variability direction, and the second one (PC2) with the second major variability direction. The PCs are always orthogonal



Source: <https://medium.com/analytics-vidhya/principal-component-analysis-pca-with-code-on-mnist-dataset-da7de0d07c22>. Retrieved: Jan 16, 2021

Mathematically, the PCA process consists in decomposing the matrix $X_{(I \times J)}$ into two matrices: scores T and loadings L . The scores express the relationship between the samples, while the loadings indicate the relationship between the variables.

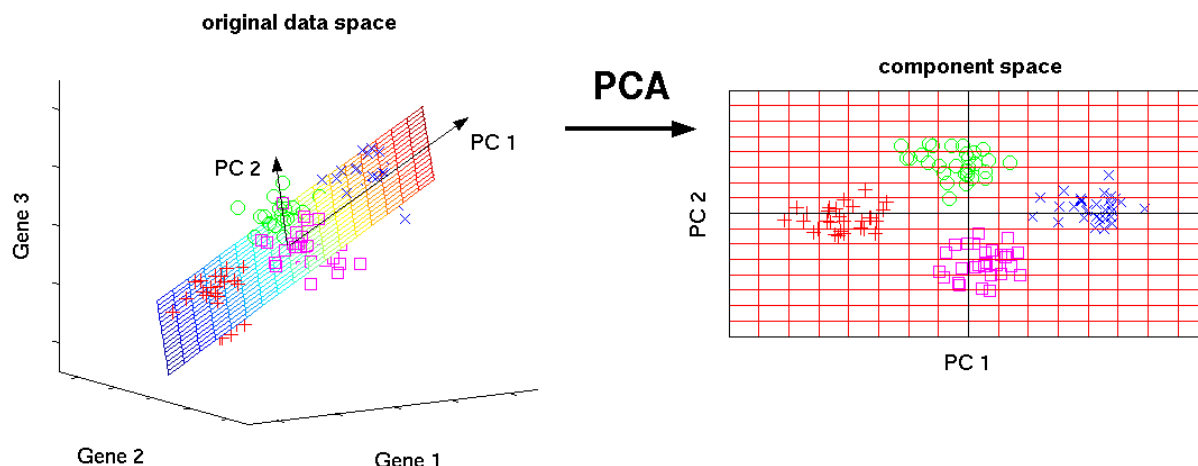
$$X = TL^T \quad (14)$$

This decomposition is equivalent to a basis change in the original variables space R^J , that has dimension J , to the principal components space, also defined in R^J . The original data is projected into the principal components space and the scores matrix carries this new projection information. The scores matrix can be written as the transformation of X by a matrix R , $T = XR$. As the loadings matrix columns are orthonormal, it is possible to write $T = XL$, which indicates that the loadings matrix is the proper transformation matrix, R .

Once the A number of PCs is defined, $X = TL^T$ can be rewritten as $X = \hat{X} + E$, where $\hat{X} = T_A L_A^T$ represents the original data and E is the $(I \times J)$ residual matrix, i.e., the data that was not modeled by the PCA (random variations, as experimental errors). T_A contains the samples coordinates information in the new axis system defined by L_A . Therefore, by applying PCA, the data important structure is separated from the experimental error. The total variance explained by the new system (what percentage of original data is explained by the reduced space) is the sum of the explained variance of each principal component. Figure 8 illustrates the PCA process

for a hypothetical system with three genes as variables and several samples (green, pink, red and blue points). The original data (3-dimensional) is projected into the principal components space (2-dimensional).

Figure 8 - Illustrative PCA applied to a 3-dimensional space, reducing it to 2-dimensional space



Source: <https://medium.com/@elmbarkikram/toward-data-science-machine-learning-algorithms-you-should-know-to-become-a-data-scientist-fdac93db9468>. Retrieved: Jan 16, 2021

There are three methods described in the literature to decompose the matrix X in scores and loadings: (i) singular value decomposition (SVD), (ii) matrix correlation diagonalization and (iii) Non-linear Iterative Partial Least Squares (NIPALS) algorithm.

As an exploratory method, PCA is a great tool. Now, if the quantification of some property of interest needs to be done, it will be necessary to develop an empirical model. It is often not possible to access the property of interest by just measuring the sample. To quantify such property, a previous calibration is necessary. A sample set with known properties is selected and measured by the equipment. Then, the calculations are made to relate the acquired data to the property of interest previously known. By following this process, the mathematical model (also known by regression model) is built. This model can be employed to access the property of interest in other unknown samples, since they are measured in the same modeling samples conditions.

The Partial Least Squares Regression (PLS) is a biased method that employs factor analysis. The motivation is to approximate the original data space to a reduced dimension space. The calculated factors are called latent variables, and are

not calculated exactly as the principal components of PCA, where each factor is obtained to explain the major variance of \mathbf{X} . A restriction is imposed in the \mathbf{X} matrix decomposition, directing it to a target solution \mathbf{y} that is the property of interest. The latent variables are calculated by means of keeping a compromise between the explained variance of \mathbf{X} and the dependent variable prediction, \mathbf{y} (property of interest). The information about the property of interest is included in the latent variables calculation, and this process is efficient to improve the models. In the PLS method, each latent variable is obtained maximizing the covariance between the t scores of \mathbf{X} matrix and the target property \mathbf{y} .

$$\mathbf{X} = \mathbf{T}_A \mathbf{L}_A^T + \mathbf{E} = \mathbf{X}_A + \mathbf{E} \quad (15)$$

$$\mathbf{y} = \mathbf{T}_A \mathbf{q} + \mathbf{e} \quad (16)$$

In the last equation, \mathbf{q} is the regression coefficient, estimated by the least squares method, $\mathbf{y} = q_1 t_q + \dots + q_A t_A + e \rightarrow \hat{\mathbf{q}} = (\mathbf{T}_A^T \mathbf{T}_A)^{-1} \mathbf{T}_A^T \mathbf{y}$, where q_0 vanishes because the data normally is mean centered or autoscaled and the unit column is not included in the \mathbf{X} matrix.

It is necessary to calculate t_a , l_a and q_a for the latent variable a ($a = 1, 2, \dots, A$) in the equations (15) and (16). According to equation (14), $\mathbf{T} = \mathbf{XW}$, where the letter \mathbf{W} is used for the weights matrix to differentiate it from the PCA loadings \mathbf{L} matrix. The correlation restriction between \mathbf{t} and \mathbf{y} is assured by doing the weight factor w_a proportional to the covariance between \mathbf{X} and \mathbf{y} . For the first latent variable ($a = 1$), it can be written as $\mathbf{w}_1 = \mathbf{X}^T \mathbf{y} (\mathbf{y}^T \mathbf{y})^{-1}$. Then, it is necessary to normalize w_1 , by calculating $\hat{\mathbf{w}}_1 = \mathbf{w}_1 / (\mathbf{w}_1^T \mathbf{w}_1)^{1/2}$.

The next step is the scores vector calculation, $\mathbf{t}_1 = \mathbf{X} \hat{\mathbf{w}}_1$. The scores vector is used to estimate the loadings vector l_a and the \mathbf{q} coefficient of \mathbf{y} , through the equations (15) and (16). By doing the matrix \mathbf{X} columns regression in the scores vector \mathbf{t}_1 , $\mathbf{X}^T = \mathbf{L}_1 \mathbf{t}_1^T \rightarrow \hat{\mathbf{L}}_1 = \mathbf{X}^T \mathbf{t}_1 (\mathbf{t}_1^T \mathbf{t}_1)^{-1}$. The \mathbf{q} coefficient is calculated as $\hat{\mathbf{q}}_1 = (\mathbf{t}_1^T \mathbf{t}_1)^{-1} \mathbf{t}_1^T \mathbf{y}$. Next, \mathbf{X} and \mathbf{y} are updated and the process repeated to estimate the next latent variables ($a = 2, 3, \dots, A$), until the last one. The residues of \mathbf{X} and \mathbf{y} are also calculated.

Assuming that the data was previously mean centered, the scores may be expressed as $\mathbf{T}_A = \mathbf{XW}_A (\mathbf{L}_A^T \mathbf{W}_A)^{-1}$. Substituting this expression in the general equation (16), the regression vector \mathbf{b} is obtained, $\hat{\mathbf{y}} = \mathbf{T}_A \mathbf{q} = \mathbf{XW}_A (\mathbf{L}_A^T \mathbf{W}_A)^{-1} \hat{\mathbf{q}} \rightarrow \hat{\mathbf{b}} = \mathbf{W}_A (\mathbf{L}_A^T \mathbf{W}_A)^{-1} \hat{\mathbf{q}}$.

3.7.1 Data treatments

It is necessary to treat the acquired data before the multivariate analysis to ensure or enhance the performance (normalizing the data, removing irrelevant information, and minimizing the noise). There are two treatment types: transformation and preprocessing. The transformation treatments (smoothing, baseline correction, normalization, horizontal alignment, etc.) are applied to the samples, while the preprocessing treatments (mean center, autoscale, Pareto scaling, etc.) are applied to the variables (Ferreira, 2015).

Spectra alignment

The samples spectra acquired by EDXRF technique may present a lack of horizontal alignment (some samples can be shifted from others along the x-axis) due to room temperature variation, system electronic parts, etc. The Correlation Optimized Warping (COW) is an alignment method (transformation treatment) that can be applied to the data before the multivariate analysis. COW aligns one shifted spectrum (\mathbf{x}_s) to a reference spectrum (\mathbf{x}_r). The reference spectrum can be the mean spectrum, for example. Both \mathbf{x}_s and \mathbf{x}_r are divided in an $N=J/M$ number of windows (segments), where J is the variables total number and M is the number of variables in each spectrum window. Each window of \mathbf{x}_s is aligned with the respective \mathbf{x}_r window. There is also a flexibility parameter (slack) to determine the initial and final points of the window, i. e., the window can be stretched or compressed in the alignment process.

Preprocessing treatments

The preprocessing treatment is an important step, and it is applied to the variables. In the EDXRF data, the variables are the detected X-ray intensities in each channel of the established energy range. To mean center the data, the mean value of each variable (column) is calculated and then subtracted from each variable value of that respective column. The data structure is preserved. In the equation, \bar{x}_j is the mean value of the j^{th} column and the index i indicates the i^{th} sample.

$$x_{MCij} = x_{ij} - \bar{x}_j \quad (17)$$

The variables autoscale is done by calculating the mean center and dividing the result by the respective column standard deviation σ_j . In this process, the variables become dimensionless. It is recommendable when the data range have great variation, because the variables with larger standard deviation will be compressed and the ones with smaller standard deviation will be expanded.

$$x_{AS_{ij}} = \frac{x_{ij} - \bar{x}_j}{\sigma_j} \quad (18)$$

The Pareto scaling uses another scale factor, the standard deviation square root. The variable dimension turns into the square root of its original dimension.

$$x_{Pareto_{ij}} = \frac{x_{ij} - \bar{x}_j}{\sqrt{\sigma_j}} \quad (19)$$

Before the Pareto scaling process, the initial and final parts of the spectra (background regions without characteristic peaks) need to be excluded to avoid undefined divisions by zero.

Poisson scaling uses the square root of the mean as scale factor. The variable dimension turns into the square root of its original dimension.

$$x_{Poisson_{ij}} = \frac{x_{ij}}{\sqrt{\bar{x}_j}} \quad (20)$$

4 MATERIALS AND METHODS

4.1 SAMPLING

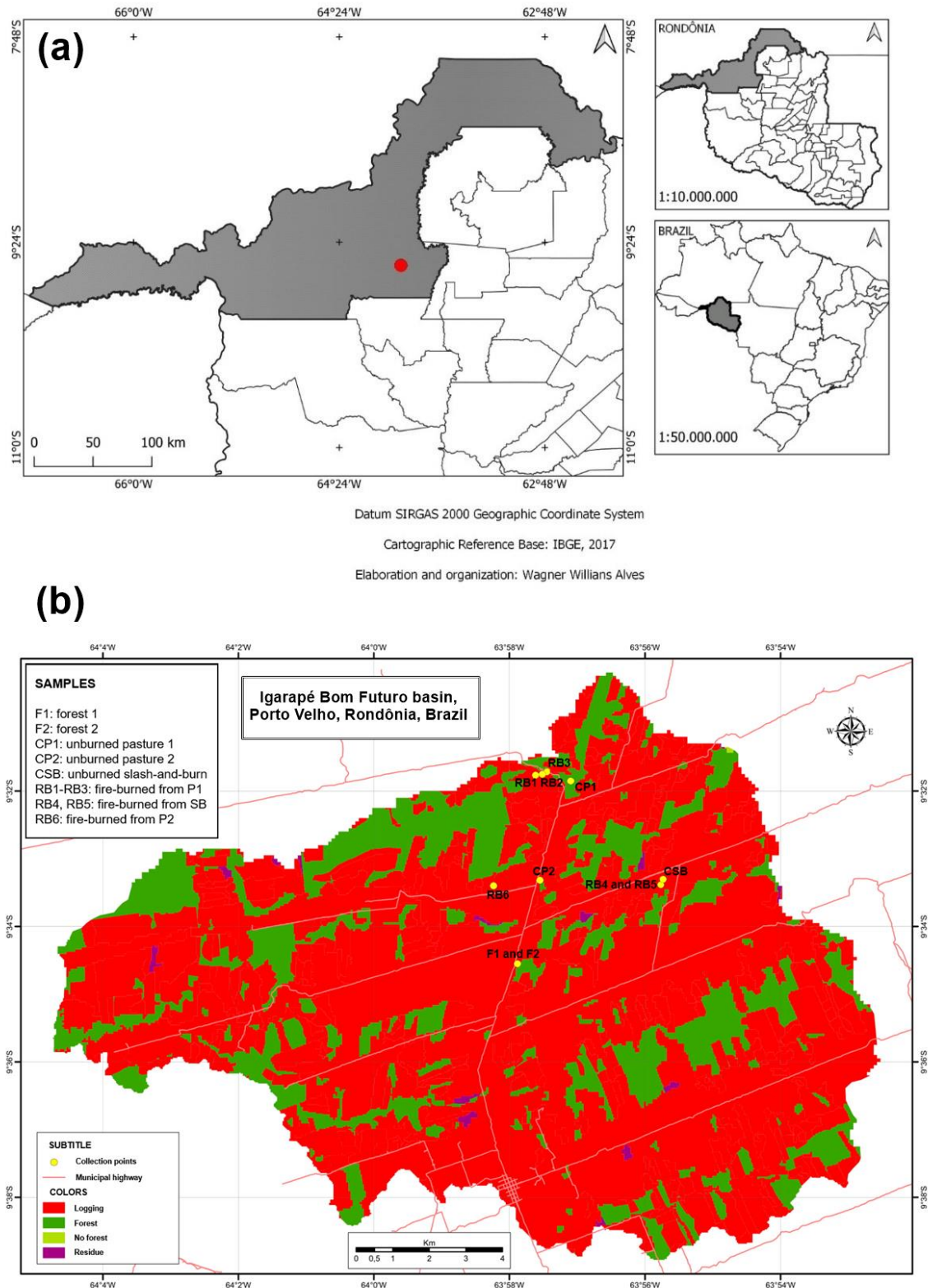
The sampling area extends over the southern Amazon region at Igarapé Bom Futuro basin, Porto Velho, Rondônia, Brazil. The soil is classified as Latossolo Vermelho-Amarelo Distrófico (EMBRAPA SiBCS, 2018). The correspondent nomenclature is Ferralsol (FAO, 2015) or Oxisol (USDA-NRCS, 1999). The region has 2100 mm mean annual precipitation, and the mean temperature is 25°C. Local vegetation is predominantly open ombrophilous forest. Open forests are characterized by large areas, regardless of variations in the relief shape. Open ombrophilous forests with lianas are characterized by the presence of *Phanera splendens* (Kunth) Vaz, *Doliodarpus major* J. F. Gmel., *Salacia opacifolia* (J F. Macbr.) A. C. Sm., and *Adenocalymma schomburgkii* (DC.) L. G. Lohmann (EMBRAPA, 2019).

The sampling set was obtained in private farms where part of the forest was turned into an agricultural area (pasture or cultivation area). Fire events history in each area was known and the idea was to predict the maximum temperature in these areas. The studied sites were two unburned forests (forest 1 and forest 2), pasture 1 (deforestation occurred in 2014), pasture 2 (deforestation occurred in 2017), and a slash-and-burn site. Due to the difficulties in accessing these areas and local conflicts, the data set consisted of 11 composite samples (each sample being a mix of 6 subsamples): F1 (unburned forest 1); F2 (unburned forest 2); CP1 (unburned pasture 1); CP2 (unburned pasture 2); CSB (unburned slash-and-burn); RB1, RB2 and RB3 (burned pasture 1); RB4 and RB5 (burned slash-and-burn); and RB6 (burned pasture 2).

Samples F1 and F2 were collected from 0 to 20.0 cm depth, while the other samples (RB1 to RB6, CP1, CP2, and CSB) were collected from 0 to 5.0 and from 5.0 to 10.0 cm depth. Samples collected from 0 - 20.0 cm were analyzed with classical methods. Samples collected from 0 - 5.0 and 5.0 - 10.0 cm was analyzed to measure the differences in elemental concentrations and the fire effects in each depth. Figure 9 presents the studied region map. The distance between collection points was 3.0 to 4.0 km from one land use to other, and 0.5 to 1.0 km from one point to other in the same land use site. After the laboratory heating treatments (which will be further explained in the controlled heating section), 43 samples were studied, [(5 unburned

samples x 6 temperatures for controlled heating) + 6 fire-burned samples + 7 controlled-heated F2 aliquots].

Figure 9 – (a) Study area (red dot) in the southern Amazon region at Rio Branco Basin, Porto Velho, Rondônia, Brazil, and (b) collection points



4.2 CONTROLLED HEATING IN MUFFLE FURNACE

The samples were previously dried at room temperature for 24 h, ground and sieved up to a particle size of $<125\ \mu\text{m}$, aiming to obtain homogeneous samples and improve the performance of the EDXRF measurements (FREITAS et al., 2021). Unburned aliquots of samples F1, F2, CP1, CP2, CSB were submitted to heating to develop the temperature estimation models. The peak temperature levels studied were 250, 400, 530, 600 and 800°C , using aliquots of samples F1, CP1, CP2 and CSB. Using aliquots of sample F2, the studied temperature levels were 150, 250, 350, 450, 550, 650, and 750°C . Such temperature gradient comprises the major biological, chemical, physical, and mineralogical changes which occur in soils during wildfires (Giovannini, 1988; Certini, 2005; Santín & Doerr, 2016). The heating features (temperature levels, time intervals) were programmed before placing the sample inside the muffle furnace. During the heating process, the temperature was monitored through the muffle display and the variation was considered the error in muffle temperature. No thermocouple was inserted inside the samples or muffle furnace. The heating rate for each range was different due to equipment recommendations: from room temperature to 400°C , $10^{\circ}\text{C min}^{-1}$; from 400 to 500°C , $5^{\circ}\text{C min}^{-1}$; from 500 to 600°C , $4^{\circ}\text{C min}^{-1}$; and from 600 to 800°C , $3^{\circ}\text{C min}^{-1}$. The controlled heating was performed with 5.0 g of soil in a porcelain capsule, exposed 20 min to peak temperature, a time interval employed in previous studies (Mataix-Solera et al., 2008; Jiménez-Pinilla et al., 2016; Rocha et al. 2019). The sample cooled down inside the muffle with the door slightly open. The heating process was performed in the Laboratório de Filmes Finos e Materiais (FILMAT), Universidade Estadual de Londrina (UEL), Londrina, Paraná.

4.3 PARTICLE SIZE DISTRIBUTION AND CHEMISTRY

Particle size distribution and chemical properties were determined by conventional soil analysis methods, described in Claessen et al. (1997) and Thomaz (2017a, 2017b). The measurements were performed at the Universidade do Centro-Oeste (UNICENTRO), Guarapuava, Paraná. Particle size distribution was analyzed by complete dispersion. The pH was determined with an electrode in CaCl₂; soil organic matter with the Walkley-Black method; P with a colorimeter of optical density; total N

by Kjeldahl method; exchangeable cations Al, Ca, Mg, K, Na, and cation exchange capacity by four extraction methods, KCl N, HCl 0,05 N, calcium acetate with pH 7.0, and ammonium acetate with pH 7.0, and saturation base calculated as the percentage of cations exchange capacity occupied by base cations (Ca^{2+} , Mg^{2+} , K^{+} , and Na^{+}).

4.4 ENERGY DISPERSIVE X-RAY FLUORESCENCE

The employed equipment was the Shimadzu EDX-720 Spectrometer at the Laboratory of X-ray Analysis (LARX), Universidade Estadual de Londrina, Londrina, Paraná. It uses a 50 W Rh X-ray tube. The data were acquired in two different conditions: 15 kV, 200 s for Na-Sc range, and 50 kV, 100 s for Ti-U range. The first condition was found to give better results for chemical elements with $Z < 20$ and the second one focused on the heavier chemical elements (Tavares et al., 2020). In both cases, current was automatically adjusted to maintain the dead time lower than 30%. Soil samples of 5.0 g were analyzed in polyethylene cups covered with 2.5 μm Mylar film. A 10 mm collimator was employed and the spectra were acquired in 2048 channels. Samples were measured in triplicate at air atmosphere.

The EDXRF equipment was calibrated before the measurements and analyses. The certified reference material (CRM) IAEA04 soil sample was employed in the calibration and the CRMs IAEA09, IAEA13, IPT32 and IPT42 in the validation. By using these four standard soil samples in the validation process, all the elements of interest, i. e., all the elements measured with good accuracy in the employed methodology, were covered (Al, Si, Ca, K, Ti, Mn, Fe, Zn, Sr and Zr).

IAEA04 was measured seven times and the elemental intensities computed. Elemental sensibilities S_i were calculated using the equation (6), $I_i = C_i \cdot S_i \cdot A$. As the standard samples have similar composition to the analyzing samples, it was not needed to calculate the absorption factor A (it was incorporated in S_i). The other four CRMs (IAEA09, IAEA13, IPT32 and IPT42) were measured to validate the calibration performed with IAEA04. The intensities of Rayleigh and Compton Rh scatterings from the X-ray tube target were also included in the quantitative routine.

4.5 MULTIVARIATE ANALYSIS WITH EDXRF DATA

Several algorithms are described in the literature to calculate the PLS

parameters (Andersson, 2009). In this research was employed SIMPLS, developed by de Jong (1993).

EDXRF data consisted of two matrices, one at 15 kV condition and the other at 50 kV condition, each one with 2048 variables (energy channels). Each matrix had 43 lines (samples). Both the initial and final parts of the spectra lacked informative peaks, so they were excluded to avoid noise modeling. By this way, the number of columns (energy channels) was 1475 at 15 kV, and 1270 at 50 kV. Thus, the matrices dimensions were (43 x 1472) at 15kV, and (43 x 1270) at 50 kV. Spectra alignment was conducted with Correlation Optimized Warping (COW) algorithm (Tomasi et al., 2014) before the spectra analysis. In terms of preprocessing methods, Pareto scaling was employed in the PLS models development (equation (20)). Considering the complete data set, a cross-validation was conducted in blocks. Initially, five PLS models were developed: model 1: using all the heated aliquots except those from F1; model 2: using all the heated aliquots except those from F2; model 3: using heated aliquots except those from CP1; model 4: using heated aliquots except those from CP2; model 5: using heated aliquots except those from CSB. Model 1 was used to estimate the temperature of samples F1, model 2 the temperature of samples F2, model 3 the temperature of samples CP1, model 4 the temperature of samples CP2, and model 5 the temperature of samples CSB. Finally, in order to estimate the temperature levels in the RB samples, model 6, using all heated aliquots from F1, F2, CP1, CP2, and CSB was developed.

In addition to the PLS models developed with EDXRF spectra, models using the elemental intensities (Al, Si, K, CA, Ti, Mn, Fe, Zn, Sr, Zr) and Compton correction (equation (8)) were also performed.

The models were evaluated according to their root mean square error of calibration (RMSEC), root mean square of cross-validation (RMSECV), root mean square error of prediction (RMSEP), determination coefficient of calibration (R^2 Cal), determination coefficient of cross-validation (R^2 CV), and determination coefficient of prediction (R^2 Pred) (Valderrama, Braga & Poppi, 2009).

4.6 THERMAL ANALYSIS

The thermal analysis was carried out with forests (F1 and F2), pasture

1, pasture 2 and slash-and-burn control soil samples (CP1, CP2 and CSB, respectively). These soil samples were not previously submitted to muffle heating treatments in laboratory. DSC and TGA measurements were done simultaneously with SDT Q600 V20.9 Build 20, Module DSC-TGA Standard equipment. Soil samples varied between 4.8 to 7.1 mg and were heated in alumina pans. Heating rate was $10\text{ }^{\circ}\text{C}\cdot\text{min}^{-1}$, temperature ranged from room temperature to $1200\text{ }^{\circ}\text{C}$, and air atmosphere was employed ($100\text{ mL}\cdot\text{min}^{-1}$) in the process. The analysis was performed by the Grupo de Física Aplicada em Materias (GFAMA), at the Universidade do Centro-Oeste, (UNICENTRO), Guarapuava, Paraná.

4.7 MUNSELL COLOR CHART

The sample color was determined by visually comparing the soil color (dry, powder samples) with the Munsell color chart, at the laboratory of the Geosciences Department, in the Universidade Estadual de Londrina (DGEO-UEL), Londrina, Paraná. The evaluated samples were the unheated ones (F1, F2, CP1, CP2, and CSB) and 8 aliquots from F2 forest that were submitted to controlled heating.

4.8 MAGNETIC SUSCEPTIBILITY

The equipment employed was the Magnetic Susceptibility Meter Model MS2 (Bartington Instruments, Oxford England) with MS2B dual frequency sensor, available at the Universidade Estadual de Maringá (UEM), Maringá, Paraná. Each sample ($\sim 1.0\text{ cm}^3$) was measured in an Eppendorf embedded in a plastic foam support to maintain the Eppendorf vertically adjusted in the sample compartment. Measurement time was 14.0 s. The samples were analyzed in triplicates. Low ($0.465 \pm 1\%$ kHz) and high frequency ($4.65 \pm 1\%$ kHz) were studied. Unburned superficial samples (0 – 5.0 cm) F1, F2, CP1, CP2 and CP4, fire burned samples RB1-RB6 (0 - 5.0 cm), and three aliquots from F2 (room temperature, 400°C and 800°C) were measured by this technique.

4.9 X-RAY DIFFRACTION

X-ray diffraction was applied on controlled heating samples (F1, F2,

CP1, CP2 and CSB) and fire-burned samples (RB1 to RB6). X-ray diffraction patterns were acquired with a PANalytical diffractometer model X'Pert PRO MPD at Laboratório de Análises por Raio X (LARX) in the Universidade Estadual de Londrina (UEL), Londrina, Paraná. The equipment uses $\text{CuK}\alpha$ radiation, 40 kV and 30 mA in the technique known as θ -2 θ , Bragg Brentano geometry. The 2 θ scanning interval ranged from 5° to 120° with an angular step of 0.05°. Counting time per point was 3.0 s. Samples were rotated cyclically during the measurement process with a period of one second. XRD patterns were analyzed using the software HighScore Plus 3.0.

4.10 VISIBLE NEAR-INFRARED

Vis-NIR was applied on unburned samples (F1, F2, CP1, CP2 and CSB), controlled heating F2 aliquots (150, 250, 350, 450, 550, 650, 750°C), and fire-burned samples (RB1 to RB6). The Vis-NIR spectra were acquired employing a FOSS XDS Vis-NIR spectrophotometer (Silver Spring, MD, USA), at Laboratório de Apoio à Pesquisa Agropecuária (LAPA) in the Universidade Estadual de Londrina (UEL), Londrina, Paraná. Samples were scanned using a ring cup of 5.0 cm diameter with 5 g of soil. Each sample spectrum, averaged from 15 spectra, was recorded as the logarithm of the inverse of the reflectance ($\log [1/R]$). The measurements were made from 400 to 2498 nm in a spectral interval of 2 nm. Data were analyzed using the WinISI III – V 1.63e software (Foss NIR Systems/Tecator Infrasoftware International, LLC, Silver Spring, MD, USA).

5 RESULTS

5.1 PARTICLE SIZE DISTRIBUTION AND CHEMISTRY

The particle size distribution and the chemical characteristics of samples F1 and F2, determined by conventional soil analysis, are presented in Table 2. The silt quantity was overestimated due to experimental limitations (~15% of error). It was expected to found more clay than silt in those soils.

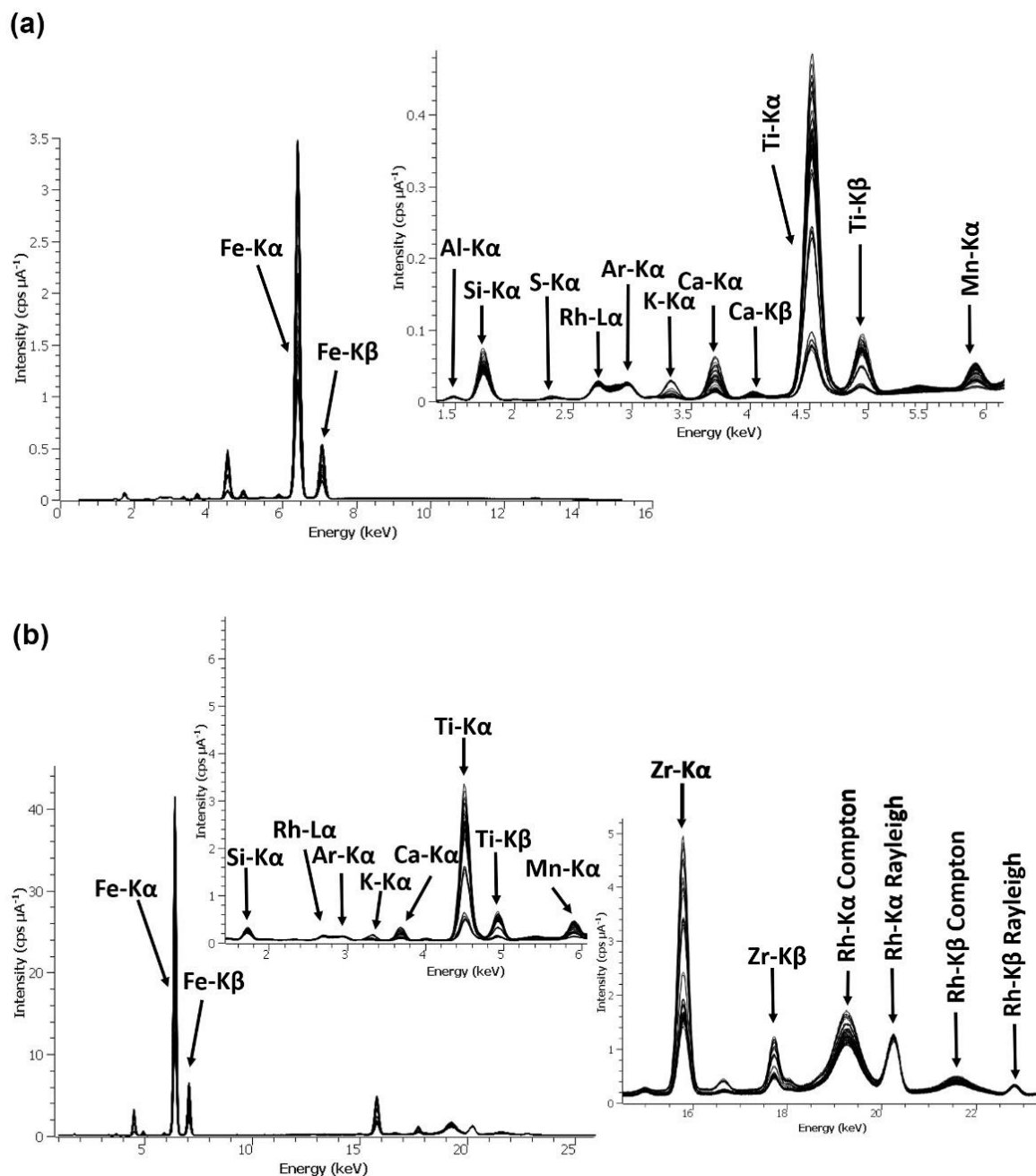
Table 2 – Particle size distribution and chemical characteristics in each forest site (F1 and F2). Soil collection depth: 0-20.0 cm

	F1	F2
Particle size distribution		
Clay (g kg ⁻¹)	260	250
Silt (g kg ⁻¹)	390	390
Sand (g kg ⁻¹)	350	360
Soil texture class	Loam	Loam
Soil chemistry		
pH CaCl ₂	4.36	4.52
Soil organic matter (g kg ⁻¹)	20.39	24.52
P (mg kg ⁻¹)	3.43	2.98
K (cmol _c kg ⁻¹)	0.15	0.10
Ca (cmol _c kg ⁻¹)	0.82	0.96
Mg (cmol _c kg ⁻¹)	0.77	0.88
Base saturation (%)	29.80	31.20
Total Kjeldahl N (%)	0.11	0.15
Cation Exchange Capacity (cmol _c kg ⁻¹)	5.83	6.22

5.2 ENERGY DISPERSIVE X-RAY FLUORESCENCE

The EDXRF spectra of all studied samples are presented in Figure 10 for both 15 kV and 50 kV conditions. The peaks were labeled according with the corresponding element.

Figure 10 – Superposed EDXRF spectra of all studied samples at (a) 15 kV and (b) 50 kV. Some regions were zoomed to label the peaks



5.2.1 EDXRF Quantitative Results

Before the quantitative analysis, the routine of the EDXRF equipment was verified using CRMs. Table 3 presents the calculated values for elemental concentration in the CRMs. For each element analyzed, two concentration values were presented: the certified concentration from the CRM, and the measured concentration (mean of six measurements). The detection limit (DL) and quantification limit (QL) for

each element are, respectively: Al = 0.3 and 1.0%; Si = 0.1 and 0.3%; K = 0.02 and 0.5%; Ca = 0.006 and 0.02%; Ti = 0.007 and 0.02%; Mn = 0.004 and 0.01%; Fe = 0.002 and 0.008%; Zn = 0.001 and 0.004%; Sr = 0.005 and 0.018%; Zr = 0.005 and 0.018%.

Table 3 – Certified and measured elemental concentrations and their respective relative deviation. Concentrations lower than the quantification limit are indicated as < QL

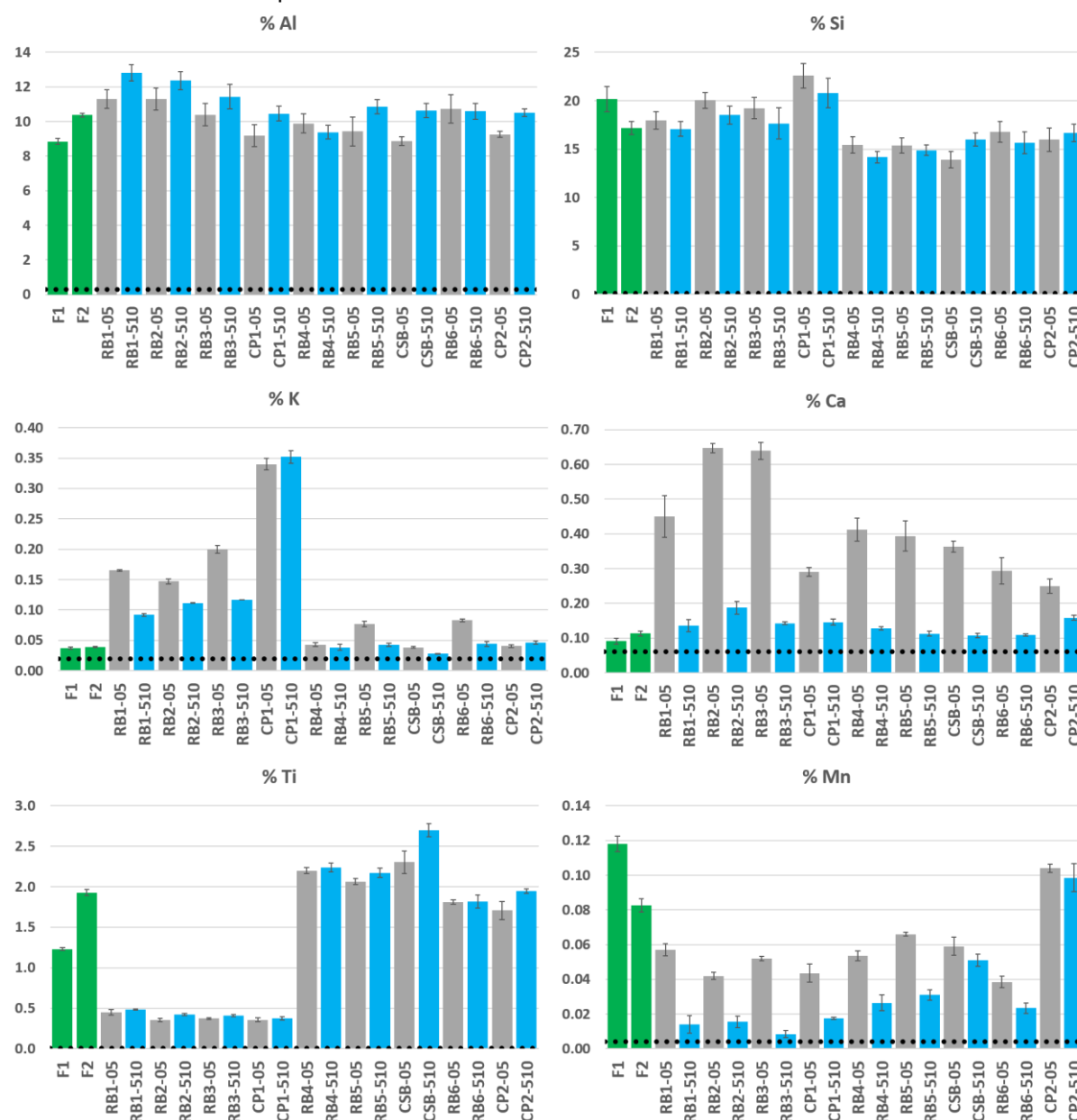
Element	Certified concentration \pm standard deviation (%)	Measured mean concentration \pm standard deviation (%)	Relative deviation
IAEA09			
Al	5.94 \pm 0.09	6.80 \pm 0.19 (< QL)	14%
Si	32.2 \pm 0.3	32.2 \pm 0.3	0%
K	1.95 \pm 0.04	1.896 \pm 0.014	-3%
Ca	1.38 \pm 0.03	1.38 \pm 0.07	0%
Ti	0.430 \pm 0.010	0.404 \pm 0.009	-6%
Mn	0.100 \pm 0.003	0.109 \pm 0.005	9%
Fe	2.97 \pm 0.05	2.837 \pm 0.013	-4%
Zn	0.0096 \pm 0.0004	0.0113 \pm 0.0005 (< QL)	18%
Sr	0.0101 \pm 0.001	0.0132 \pm 0.0003 (< QL)	25%
Zr	0.030 \pm 0.001	0.0352 \pm 0.0003	18%
IAEA13			
Al	10.00 \pm 0.14	7.9 \pm 0.4 (< QL)	21%
Si	26.1 \pm 0.2	24.5 \pm 0.8	6%
K	0.117 \pm 0.003	0.114 \pm 0.002 (< QL)	3%
Ca	1.54 \pm 0.03	1.871 \pm 0.008	-22%
Ti	0.442 \pm 0.016	0.446 \pm 0.009	-1%
Mn	0.148 \pm 0.004	0.157 \pm 0.008	-6%
Fe	5.38 \pm 0.08	5.25 \pm 0.02	2%
Zn	0.0066 \pm 0.0003	0.0065 \pm 0.0005 (< QL)	2%
Sr	0.015 \pm 0.002	0.0149 \pm 0.0003	-1%
Zr	0.0135 \pm 0.0005	0.0192 \pm 0.0004	42%
IPT32			
Al	15.08 \pm 0.11	15.3 \pm 0.7 (< QL)	-1%
Si	24.21 \pm 0.14	22.5 \pm 0.6	7%
K	0.66 \pm 0.03	0.570 \pm 0.011	14%
Ca	0.121 \pm 0.014	0.127 \pm 0.005 (< QL)	-4%
Ti	0.893 \pm 0.012	0.912 \pm 0.011	-2%
Fe	2.42 \pm 0.05	2.49 \pm 0.02	-3%
IPT42			
Al	17.04 \pm 0.11	18.3 \pm 0.8	-7%
Si	24.26 \pm 0.05	23.2 \pm 0.8	4%
K	0.39 \pm 0.04	0.434 \pm 0.003	-11%
Ca	0.036 \pm 0.007	0.047 \pm 0.014	-30%
Ti	0.58 \pm 0.02	0.555 \pm 0.005	4%
Fe	0.76 \pm 0.03	0.823 \pm 0.005	-8%

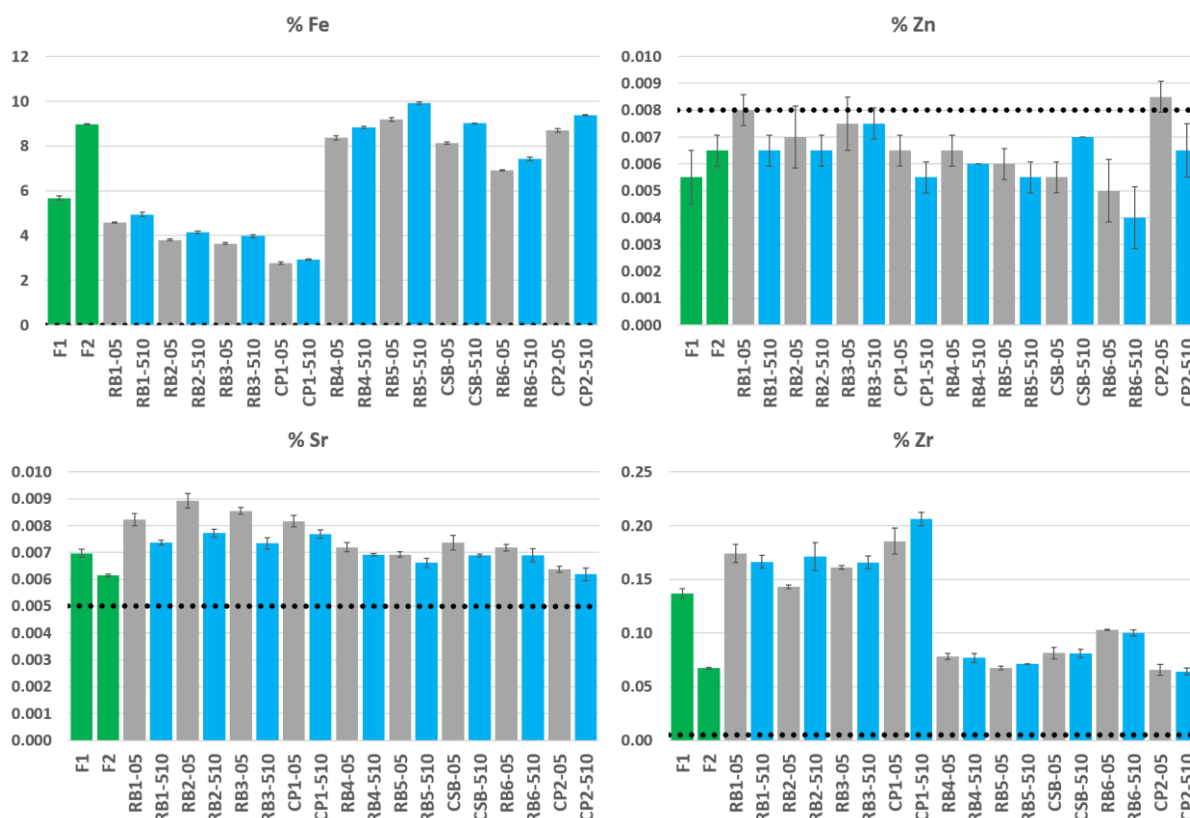
Although Al and Si are light elements, their concentrations in the standard samples used for validation are high enough to produce satisfactory results. Other elements (K, Ca, Ti, Mn, Fe, Zn, Sr and Zr) have satisfactory values of relative deviation. In general, the best results of validation were those from IAEA09 (river clay) because of its similar composition to IAEA04 (clay), the standard sample used in the calibration.

5.2.2 Elemental concentration

The measured elemental concentration with its respective standard deviation is presented in Figure 11 for unburned and fire-burned samples. There is one graph for each studied element (Al, Si, Ca, K, Ti, Mn, Fe, Zn, Sr and Zr). The bigger differences due to collection depth was found for Ca and Mn. Both presented greater concentration in superficial soil, i. e., 0 – 5.0 cm depth. The elemental concentration values are given in Annex A.

Figure 11 – Concentration (%) of Al, Si, K, Ca, Ti, Mn, Fe, Zn, Sr and Zr in the studied soils. The numbers after the sample name mean the collection depth (05 for 0 – 5.0 cm and 510 for 5.0 – 10.0 cm). F1 and F2: forests collected from 0 – 20.0 cm. RB1, RB2, RB3 and CP1: pasture 1. RB4, RB5, and CSB: slash-and-burn. RB6 and CP2: pasture 2. Black dashed line stands for detection limit





Samples from pasture 1 (RB1-05, RB1-510, RB2-05, RB2-510, RB3-05, RB3-510, CP1-05, CP1-510) presented a different behavior for K, Ti, Fe, and Zr. It indicates a lithological discontinuity, i. e., the materials may have come from a different origin.

5.2.3 Principal Component Analysis

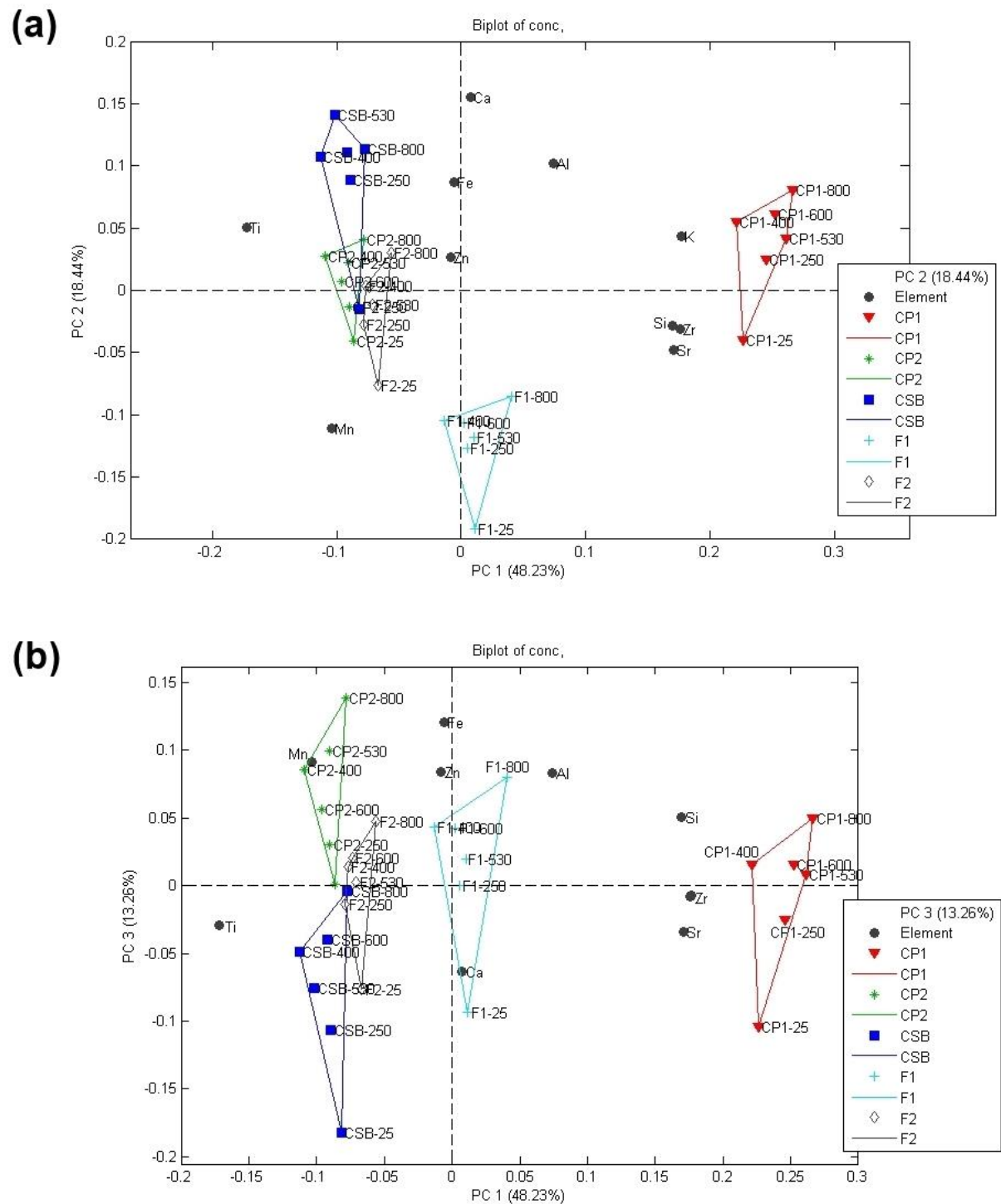
Principal component analysis was performed with elemental concentrations and EDXRF spectra. The first one, performed with elemental concentrations, had 10 variables (Al, Si, Ca, K, Ti, Mn, Fe, Zn, Sr and Zr) and is presented in the Annex A. Two components were selected, explaining 71.47% of the total variance. A separation tendency between the samples collected from 0 – 5.0 cm depth and the ones collected from 5.0 – 10.0 cm depth was observed. Superficial soil was characterized by Si, Ca, K, Mn, Zn and Sr, while soil was characterized by Al and Zr.

The PCA analysis was also performed using the spectral data. The PCA performed with 15 kV spectra and mean center preprocessing did not separate the samples by their collection depths, but according to their sites. Pareto scaling

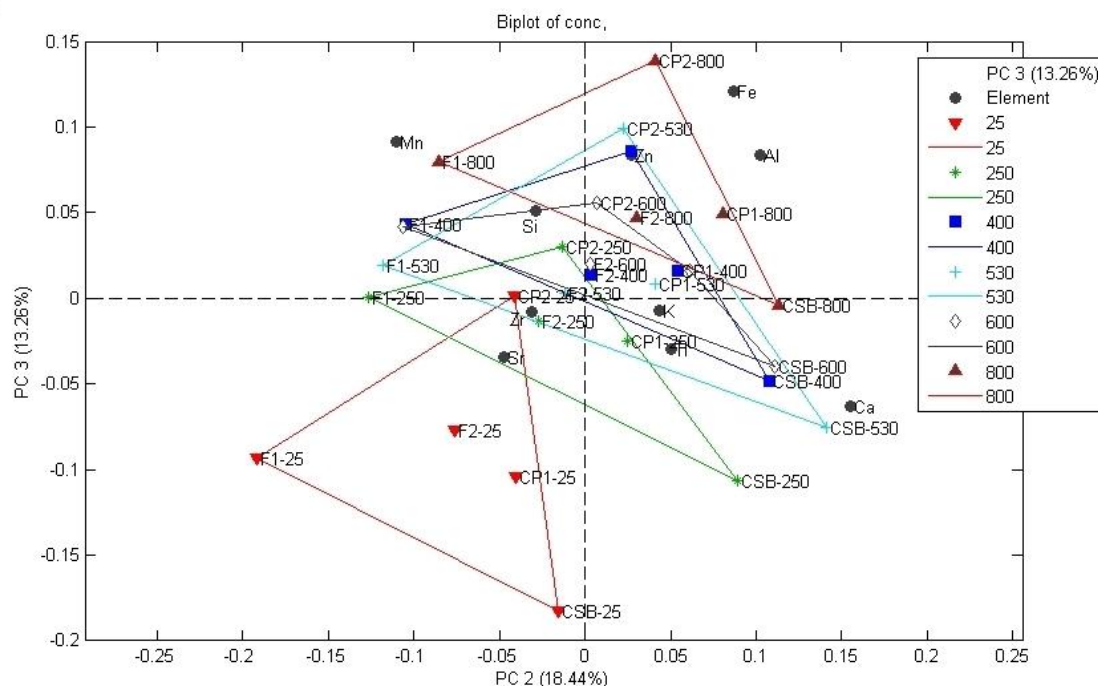
presented similar results to Poisson and mean center preprocessing. Scores plots are presented in Annex A. Three principal components were selected for the PCA model, totalizing 99.32% of explained variance. PC1 x PC2 presented a separation between pasture 1 and the samples from other sites, while PC1 x PC3 grouped the samples by their collection depths. Forests F1 and F2 (both with 0 – 20.0 cm depth) laid closer to 5.0 – 10.0 cm depth samples.

The spectra acquired in 50 kV were treated with the same preprocessing methods (mean center, Poisson and mean center, and Pareto), and the results were similar to those found in 15 kV analysis. The PCA performed with spectra was more efficient in characterizing the soils than the PCA performed with elemental concentrations. It occurred because the spectrum carries more information (scattering region, for example), and its employment must perform a better soil characterization. In addition to unburned and fire-burned soils study, samples submitted to controlled burning at different temperature levels were also analyzed using PCA. Temperatures analyzed were 25 (unburned), 250, 400, 530, 600, and 800 °C. Elemental concentration data was preprocessed with autoscale. The Figure 12 shows the biplots (scores and loadings) for PC1 x PC2 and PC2 x PC3. PC1 explained 48.23% of variance, PC2 18.44% and PC3 13.26%, totalizing 79.93% variance explained.

Figure 12 - Biplots of (a) PC1 x PC2, (b) PC1 x PC3 and (c) PC2 x PC3. Classes: F1 and F2 forests, CP1: control forest of pasture 1, CSB: control forest of slash-and-burn, CP2: control forest of pasture 2. In the biplot (c), PC2 x PC3, the classes are the heating temperatures



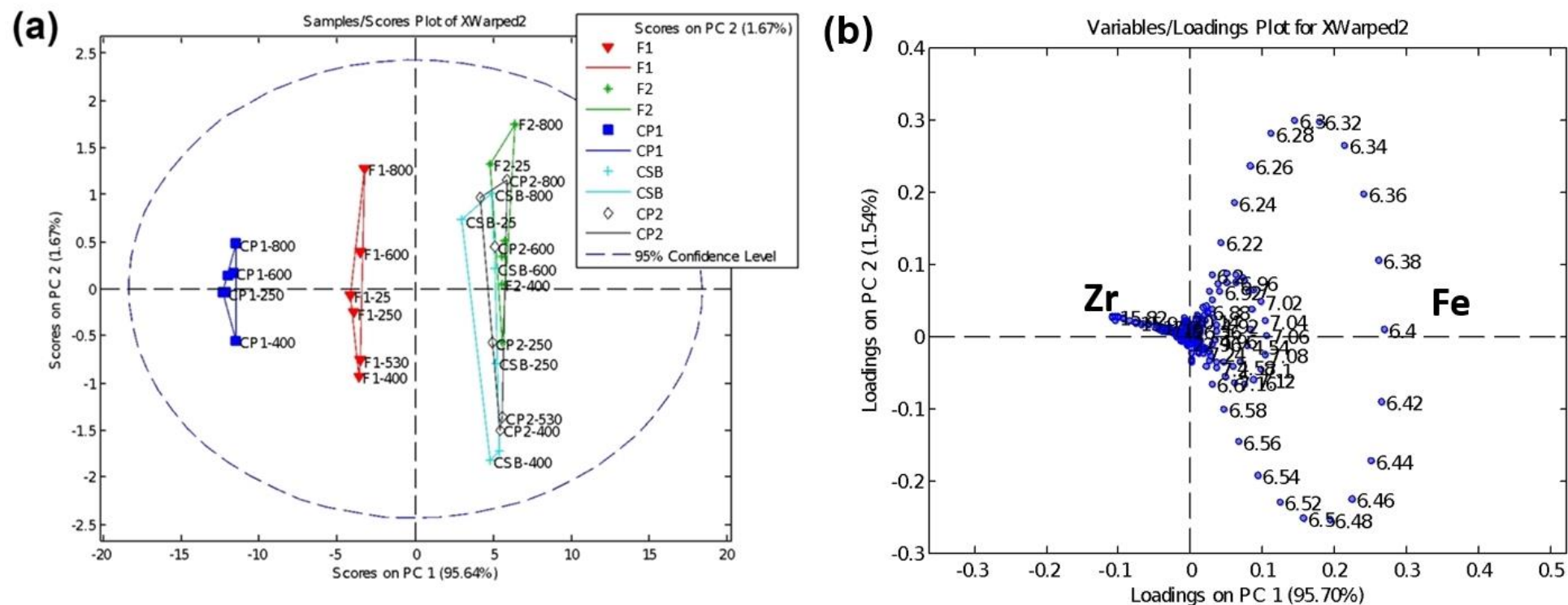
(c)

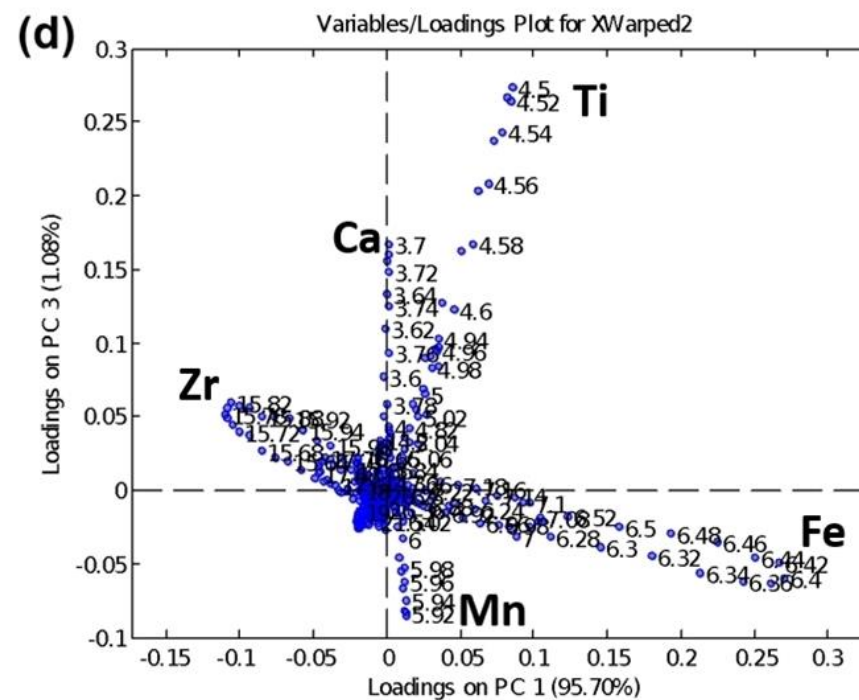
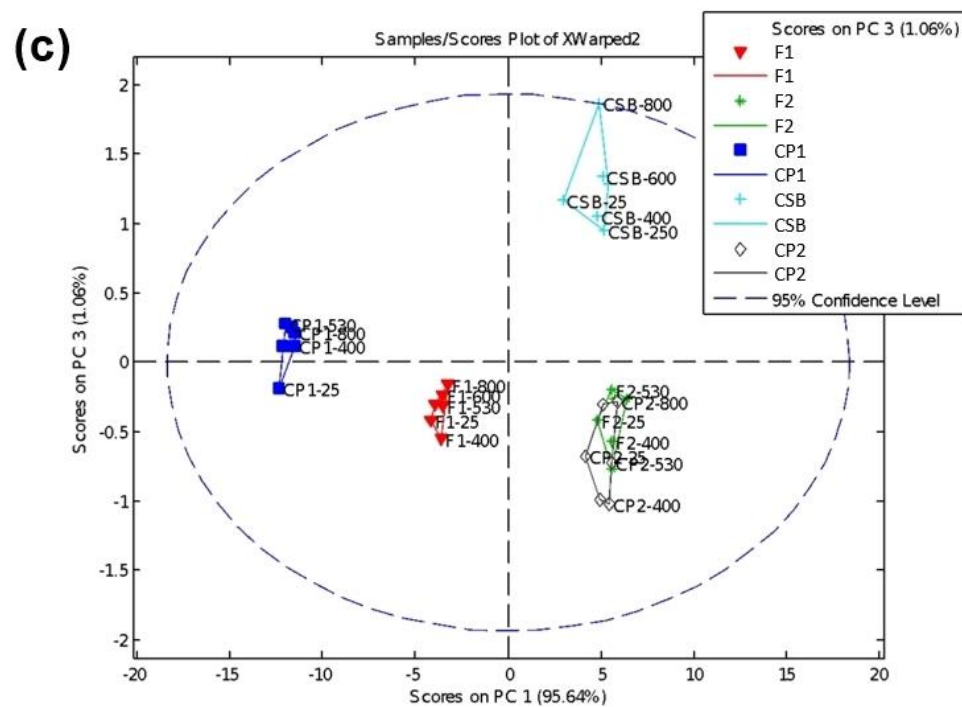


In the biplot PC1 x PC2, the samples were grouped by their collection site. Pasture 1 was characterized by K, Si, Sr and Zr (PC1 positive direction), while other sites were characterized by Ti and Mn (PC1 negative direction). PC2 x PC3 biplot indicates a temperature grouping tendency: higher temperatures tend to PC3 positive direction due to Al, Fe, Mn, and Zn, while lower temperatures tend to PC3 negative direction due to Ca, K, Ti, and Zr.

The spectra (15 kV and 50 kV conditions) of controlled heating samples were also analyzed by PCA. As the samples were measured in different days for each temperature, the acquired spectra presented a lack of alignment (the peaks were randomly horizontal shifted along the spectrum). It was solved by applying the Correlation Optimized Warping (COW). The preprocessing (mean center, Poisson and mean center, or Pareto scaling) was applied after the alignment. The condition that enabled the best differentiation between the groups, was using 50 kV spectra with Poisson and mean center preprocessing. Scores and loadings graphs for PC1 x PC2 and PC1 x PC3 are shown in Figure 13.

Figure 13 – (a) Scores for PC1 x PC2, (b) scores for PC1 x PC3, (c) loadings for PC1 x PC2, and (d) loadings for PC1 x PC3. The scores classes are the collection sites (F1, F2, CP1, CP2 and CSB)





PC1 x PC2 separated samples in three groups: pasture 1 (CP1) with forest 1 (F1); and forest 2 (F2) together with slash-and-burn (CSB) and pasture 2 (CP2). It was mainly due to the Fe (PC2 positive direction) and Zr (PC2 negative direction). The apparent separation by temperature may be an effect of the unalignment, as the scores of PC1 x PC2 present a “petal” in the Fe Ka peak (6.4 keV). Indeed, the samples are discriminated by their site of collection, as can be seen in PC1 x PC3 scores graph, which clearly separates the samples by their collection sites. It happens because the slight unalignment in the spectra was not reflected in these PCs.

5.2.4 PLS models and temperature estimation

The best regression model was using 50 kV spectra with Pareto preprocessing. Table 4 presents the quality parameters of PLS models, and Table 5 the estimated temperatures of each model. Figure 14 illustrates the PLS prediction, showing the graph of measured versus predicted temperature for model 1. RMSECV and R^2 values of models 1 to 5 were used to select the number of latent variables (leave-one-out method) and omitted from table. It was not possible to calculate the RMSEP and R^2 of prediction of model 6, as we did not have the burning temperature of RB samples in situ. The accuracy of such model is based on the results of models 1 to 5, mainly the ones that estimated the temperature of the muffle heated aliquots of samples CP1, CP2 and CSB. They presented high accuracy with R^2 Pred equals to 0.89, 0.82 and 0.98, respectively.

The PLS models developed with the elemental intensities and Compton correction are presented in the Annex B.

Table 4 – PLS models developed with EDXRF spectra at 50 kV. LVs: number of latent variables. RMSEC: root mean squared error of calibration. RMSECV: root mean squared error of cross-validation. RMSEP: root mean squared error of prediction. CV Bias: Cross-validation bias. Pred Bias: prediction bias. R^2 Cal: determination coefficient of calibration. R^2 CV: determination coefficient of cross-validation. R^2 Pred: determination coefficient of prediction

Model	Calibration samples	Estimation samples	LV	RMSEC (°C)	RMSEP (°C)	Bias	Pred Bias	R^2 Cal	R^2 Pred
1	F2, CP1, CP2, CSB (n=26)	F1 (n=5)	4	72	158	-5.7E-14	-7.54	0.8538	0.2951
2	F1, CP1, CP2, CSB (n=20)	F2 (n=10)	5	36	118	-2.27E-13	26.62	0.9624	0.5289
3	F1, F2, CP2, CSB (n=26)	CP1 (n=5)	2	153	122	0	-7.54	0.3460	0.8902
4	F1, F2, CP1, CSB (n=26)	CP2 (n=5)	3	76	158	0	-7.54	0.8345	0.8254
5	F1, F2, CP1, CP2 (n=26)	CSB (n=5)	4	52	89	0	-7.54	0.9252	0.9810
	Calibration	Estimation	LV	RMSEC (°C)	RMSECV* (°C)			R^2 Cal	
6	F1, F2, CP1, CP2, CSB (n=31)	RB (n=6)	3	81	129			0.8146	

* Mean of RMSEP from models 1 to 5

Figure 14 - Measured versus predicted temperature of model 1. Prediction samples are the F1 controlled heating samples (red triangles). Calibration samples (black dots) are the controlled heating samples F2, CP1, CP2 and CSB

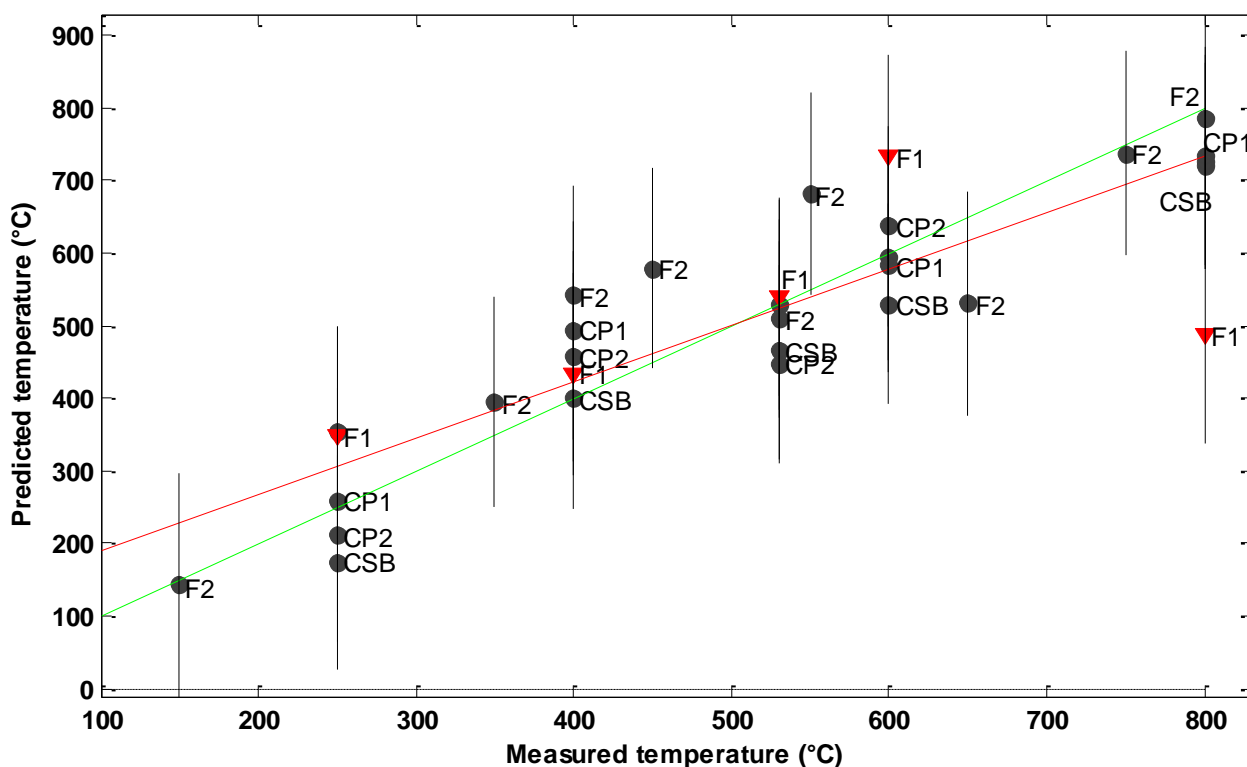


Table 5 – Controlled-heat temperature and estimated temperature by PLS models with their respective relative deviations

Model	Controlled temperature (°C)	Estimated temperature (°C)	Relative deviation	Model	Controlled temperature (°C)	Estimated temperature (°C)	Relative deviation
1 (F1 estimative)	250	349	40%	4 (CP2 estimative)	250	-7	-103%
	400	433	8%		400	438	10%
	530	539	2%		530	471	-11%
	600	733	22%		600	830	38%
	800	489	-39%		800	810	1%
2 (F2 estimative)	250	419	68%	5 (CSB estimative)	250	114	-55%
	350	502	44%		400	401	0%
	450	619	38%		530	494	-7%
	550	639	16%		600	592	-1%
	650	482	-26%		800	941	18%
	750	647	-14%	6 (RB estimative)	RB1 (from P1)	590	
	400	424	6%		RB2 (from P1)	325	
	530	463	-13%		RB3 (from P1)	422	
	600	655	9%		RB4 (from SB)	586	
	800	745	-7%		RB5 (from SB)	608	
					RB6 (from P2)	526	
3 (CP1 estimative)	250	392	57%				
	400	496	24%				
	530	537	1%				
	600	510	-15%				
	800	608	-24%				

In general, the relative deviation was higher in the 250°C estimation. Considering only 250°C estimation, the mean relative deviation (absolute value) was 45%. Now, considering 350 to 800°C range, the mean relative deviation (absolute value) was 19%. It was not possible to calculate the relative deviations in fire-burned samples, as temperatures during the fires were not known because such burnings were not prescribed fires. However, the accuracy of model 6 (model used to estimate the maximum temperature of sample RB1 to RB6) is demonstrated by the quality parameters values from models 1 to 5 (Table 4).

5.3 THERMAL ANALYSIS

Figure 15 presents unburned samples (F1, F2, CP1, CP2 and CSB)

graphs. For each analyzed sample, there are TGA (weight x temperature), DSC (heat flow x temperature), and DTA (temperature difference x temperature) curves. Colored ellipses were added to F1 graph to indicate the temperature range that the transformations were observed. All samples have similar behavior.

As the general behavior was similar for all samples, the following analysis considers only sample F2. Until 110°C, F2 lost superficial water. The hygroscopic water was lost until 200°C, together with lighter elements volatilization, as P and S (Araya et al., 2016). In this process, water molecules weak bounded in soil samples boil, the heat is being absorbed by the sample and a soft valley can be observed in the DTA curve (endothermic process). Gibbsite and goethite dehydroxylation occurred between 200 and 350°C (Plante et al., 2009; Lugassi, Ben-Dor & Eshel, 2014). The organic matter decomposition (mainly carboxylic and phenolic functional groups of the humic and fulvic acids and hydrocarbon compounds) happened until 320°C. In this range, the mass loss could also be due to the release of light organic compounds. From 320 to 430°C, the mass loss was mainly due to the C oxidation ($R-CH + O_2 \rightarrow CO_2 + H_2O$, R = radical). A valley between 400 and 500°C in the DTA curve is observed, characterizing the kaolinite dehydroxylation (endothermic process). The total mass loss for F2 was 12.2%. Temperature intervals and descriptions are presented in

Table 6 for all analyzed samples. Although the total mass loss had been different for each sample, the general behavior (reactions and transformations) was similar.

Figure 15 – Thermal analysis of unburned samples. Dot symbols: TGA, square symbols: DTA, and plus symbols: DSC. The dashed red line indicates the mass (%) and the dashed gray line indicates the temperature for TGA analysis. (a) Forest 1 (F1), (b) forest 2 (F2), (c) pasture 1 (CP1), (d) slash-and-burn (CSB) and (e) pasture 2 (CP2)

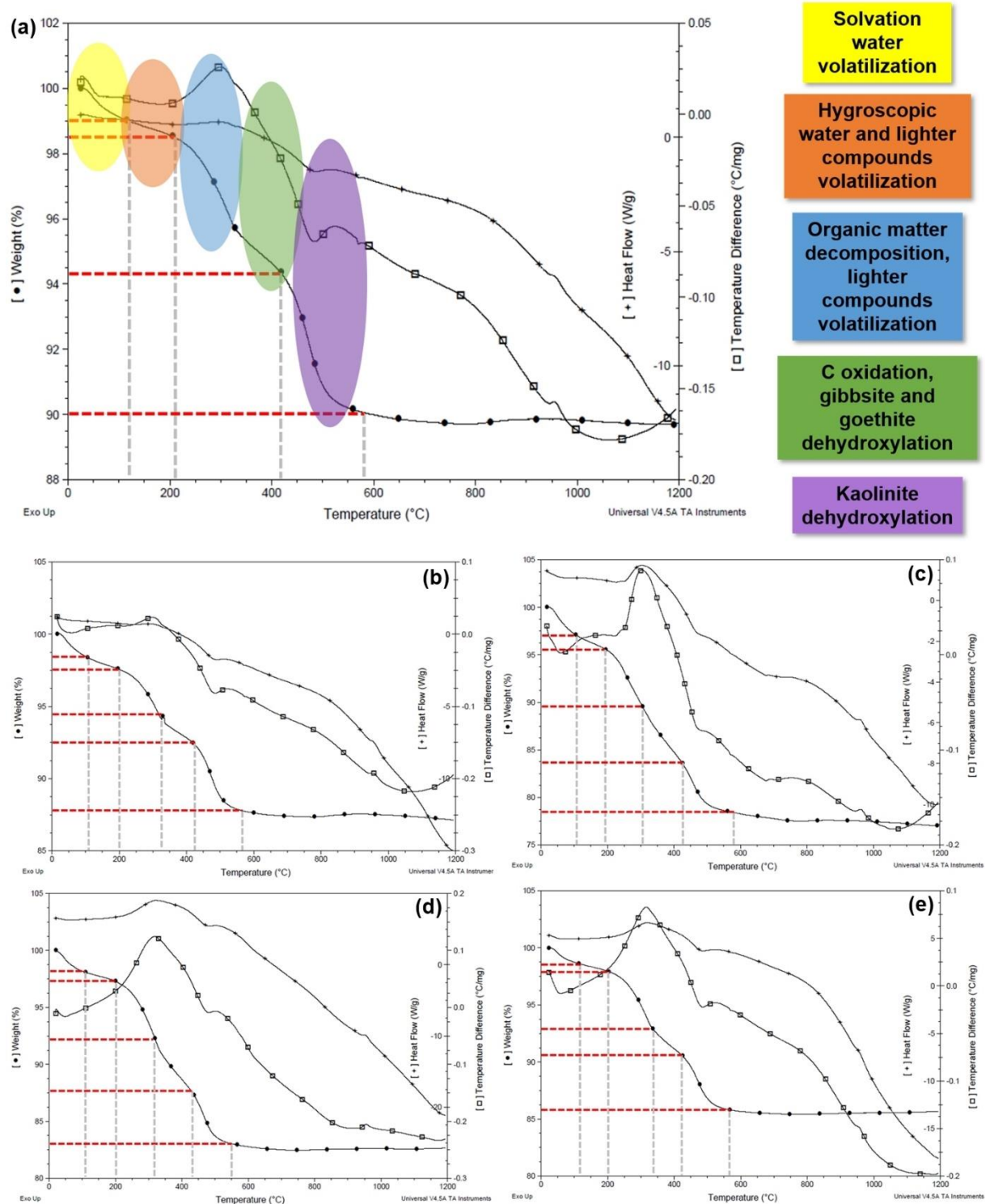


Table 6 - Main transformations and reactions with their respective mass loss in each temperature range

Sample	Solvation water volatilization	Hygroscopic water and lighter compounds volatilization	OM decomposition and lighter compounds volatilization	C oxidation, gibbsite and goethite dehydroxylation	Kaolinite dehydroxylation	Total mass loss (%)
Forest 1	$T_{amb} - 125^{\circ}\text{C}$ (1.0%)	125 – 210°C (0.5%)	210 – 250°C (2.8%)	250 – 420°C (1.4%)	420 – 580°C (4.3%)	10.0
Forest 2	$T_{amb} - 110^{\circ}\text{C}$ (1.3%)	150 – 200°C (1.2%)	200 – 320°C (3.1%)	320 – 430°C (1.9%)	430 – 570°C (4.7%)	12.2
Pasture 1	$T_{amb} - 110^{\circ}\text{C}$ (2.9%)	110 – 190°C (1.4%)	190 – 250°C (5.6%)	250 – 430°C (6.2%)	430 – 580°C (5.0%)	21.1
Slash-and-burn	$T_{amb} - 110^{\circ}\text{C}$ (1.8%)	110 – 200°C (0.9%)	200 – 250°C (5.0%)	250 – 430°C (4.8%)	430 – 550°C (4.3%)	16.8
Pasture 2	$T_{amb} - 110^{\circ}\text{C}$ (1.3%)	110 – 200°C (0.8%)	200 – 250°C (5.0%)	250 – 425°C (2.4%)	425 – 560°C (4.8%)	14.3

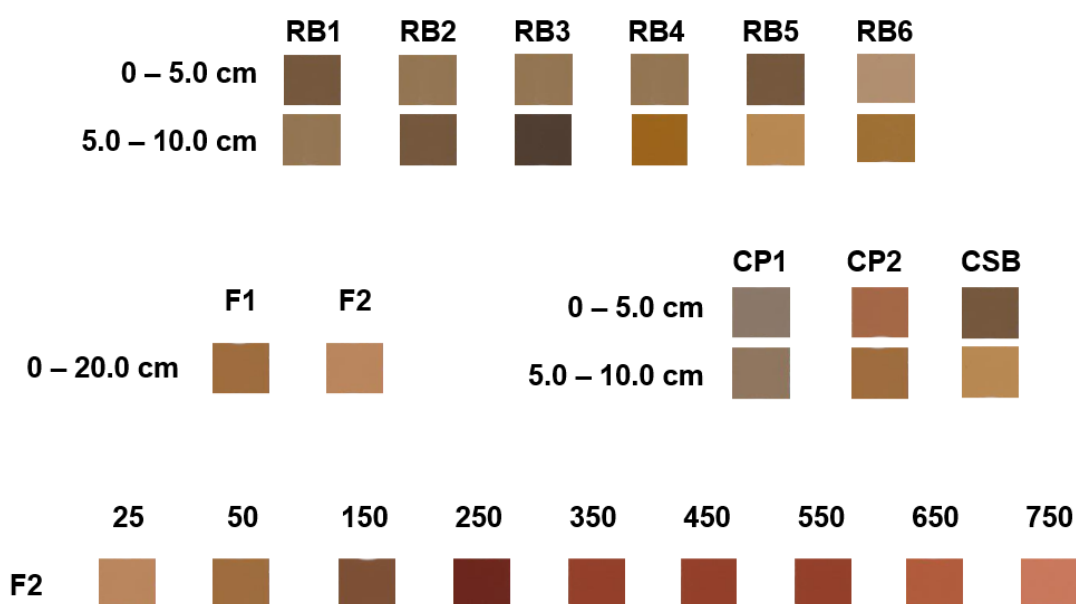
5.4 MUNSELL COLOR CHART

The Munsell colors are presented in Table 7 and Figure 16. In general, the samples collected from 0 – 5.0 cm and 5.0 – 10.0 cm (left columns) have 100% of yellow and 0% of red for hue, except by pasture 2 (CP2), which presented 50% of yellow and 50% of red in the 0 – 5.0 cm, and 75% of yellow and 25% of red in the 5.0 – 10.0 cm soil sample. The pasture 2 area is being converted into pasture, so its color is similar to forest color. The value ranged from 3 to 6 and chroma ranged from 2 to 8 for samples in the left column (pasture 1, pasture 2, and slash-and-burn). The forest F1 and F2 samples, collected from 0 – 20.0 cm depth, have 75% of yellow and 25% of red for hue, 5 and 6 for value, respectively, and both have 6 for chroma. The controlled-burned F2 aliquots presented more variation in hue. In general, it ranged from 75% of yellow and 25% of red for lower temperatures to 25% of yellow and 75% of red for higher temperatures. The value ranged from 3 to 6 and chroma from 4 to 8.

Table 7 - Munsell color for each soil sample studied. YR: yellow-red. RB1, RB2, RB3, CP1: old pasture. RB4, RB5, CSB: slash-and-burn. RB6, CP2: recent pasture. F1, F2: forest. RT1-RT8: F2 heated aliquots

Sample (depth in cm)	Munsell color	Sample (0 – 20.0 cm depth)	Munsell color
RB1 (0 – 5.0)	10YR 4/3	F1	7.5YR 5/6
RB1 (5.0 – 10.0)	10YR 5/4	F2	7.5YR 6/6
RB2 (0 – 5.0)	10YR 5/4	F2 (50°C)	7.5YR 5/6
RB2 (5.0 – 10.0)	10YR 4/3	F2 (150°C)	7.5YR 4/4
RB3 (0 – 5.0)	10YR 5/4	F2 (250°C)	2.5YR 3/6
RB3 (5.0 – 10.0)	10YR 3/2	F2 (350°C)	2.5YR 4/8
CP1 (0 – 5.0)	10YR 5/2	F2 (450°C)	2.5YR 4/8
CP1 (5.0 – 10.0)	10YR 5/3	F2 (550°C)	2.5YR 4/8
RB4 (0 – 5.0)	10YR 5/4	F2 (650°C)	2.5YR 5/8
RB4 (5.0 – 10.0)	10YR 5/8	F2 (750°C)	2.5YR 6/8
RB5 (0 – 5.0)	10YR 4/4		
RB5 (5.0 – 10.0)	10YR 6/6		
CSB (0 – 5.0)	10YR 4/4		
CSB (5.0 – 10.0)	10YR 6/6		
RB6 (0 – 5.0)	10YR 6/4		
RB6 (5.0 – 10.0)	10YR 5/6		
CP2 (0 – 5.0)	5 YR 5/6		
CP2 (5.0 – 10.0)	7.5 YR 5/6		

Figure 16 - Munsell colors of the analyzed samples in different collection depths. RB1-RB6: burned samples. F1, F2, CP1, CP2, CP2, CSB: unburned samples. 25-750: F2 aliquots heated in muffle (25 indicates the unburned aliquot). The number indicates the temperature peak (50-750°C) that the sample was heated



5.5 MAGNETIC SUSCEPTIBILITY

The magnetic susceptibility for the samples investigated in this study are presented in Table 8. The frequency dependent magnetic susceptibility was calculated using equation 9 and frequency dependent using equation 10.

Table 8 - Magnetic susceptibility measured for F2 aliquots: unburned, muffle heated at 400 °C and at 800 °C; fire-burned samples RB1 to RB6; and unburned samples CP1, CP2 and CSB. (χ_{FD}) is the frequency dependent magnetic susceptibility, and SD is the standard deviation

Sample	Mass \pm 0.05 g	(χ_{LF}) \pm SD $10^{-8} \text{ m}^3 \text{ kg}^{-1}$ (low frequency)	(χ_{HF}) \pm SD $10^{-8} \text{ m}^3 \text{ kg}^{-1}$ (high frequency)	(χ_{DF}) (%)
F2	1.07	18.9 \pm 0.1	16.1 \pm 0.4	15.1
F2 (400 °C)	1.06	18.8 \pm 0.4	16.3 \pm 0.8	13.7
F2 (800 °C)	1.04	2.6 \pm 0.4	2.4 \pm 0.5	8.6
RB1	1.05	4.4 \pm 0.1	4.0 \pm 0.4	10.7
RB2	1.10	4.3 \pm 0.1	3.8 \pm 0.2	11.9
RB3	1.03	4.6 \pm 0.2	3.8 \pm 0.1	16.9
CP1	1.08	3.0 \pm 0.1	2.3 \pm 0.3	22.7
RB4	1.11	7.8 \pm 0.1	6.5 \pm 0.3	16.9
RB5	1.09	29.4 \pm 0.1	25.5 \pm 0.4	13.4
CSB	1.10	6.1 \pm 0.2	5.4 \pm 0.2	11.9
RB6	1.04	6.2 \pm 0.2	5.1 \pm 0.4	17.1
CP2	1.05	21.7 \pm 0.5	17.6 \pm 1.4	19.3

In general, the samples presented small values of magnetic susceptibility, indicating a low content of magnetic minerals. Frequency dependent magnetic susceptibility ranged between 8.6 and 22.7%. Considering that the higher value of magnetic susceptibility was $30 \times 10^{-8} \text{ m}^3 \text{ kg}^{-1}$ (RB5 in the low frequency mode), and that the magnetic susceptibility of pure ferrimagnetic minerals (i. e., 100%) varies from 20000 to 110000 $10^{-8} \text{ m}^3 \text{ kg}^{-1}$ with an average value of $50000 \times 10^{-8} \text{ m}^3 \text{ kg}^{-1}$, the percentage of ferrimagnetic minerals in the samples were $< 0.06\%$. It indicates that only maghemite is present in the samples, not magnetite.

Different transformations may occur in the temperature range studied (Hanesch, Stanjek & Petersen, 2006). It was observed that pure goethite dehydroxylates to hematite between 200 and 400°C; if additional organic carbon is added, maghemite is formed. When hematite is heated, the presence of organic substance leads to reducing conditions, which promote the formation of maghemite or magnetite. Maghemite can transform into hematite when exposed to high temperatures, but isomorphic substitution (e.g., Al^{3+}) may largely influence this process. Nonaka et al., (2017) observed that such isomorphic substitution of Fe by Al

increased the critical temperature of transformation and the time necessary for maghemite to hematite transformation.

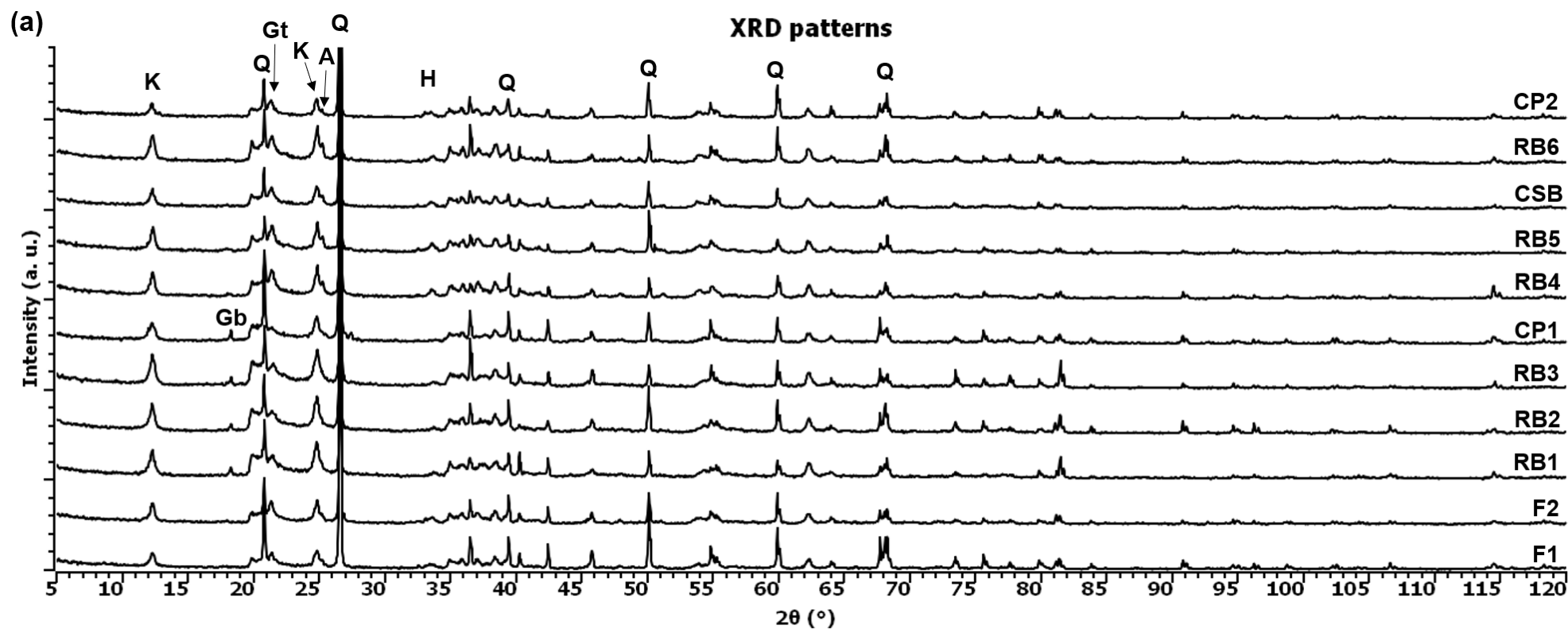
F2 samples presented a higher magnetic susceptibility until 400 °C, indicating the presence of a magnetic content, but it transforms into a non-magnetic phase and is not detected at 800 °C. It is a strong indicative of maghemite to hematite transformation. Sample RB5 also presented a high magnetic susceptibility, probably due to heating (hematite and/or goethite transformed into maghemite), because in the control sample, CSB, the magnetic susceptibility was low.

5.6 X-RAY DIFFRACTION

Crystalline phases detected in unburned samples F1, F2, CP2, and CSB were hematite (Fe_2O_3), quartz (SiO_2), kaolinite ($\text{Al}_2(\text{OH})_4\text{Si}_2\text{O}_5$), anatase (TiO_2), and goethite ($\text{FeO}(\text{OH})$). In the unburned sample CP1, gibbsite ($\text{Al}(\text{OH})_3$), quartz, and kaolinite were detected. Crystalline phases detected by XRD agreed with literature (Beinroth et al., 1996; Schaefer, Fabris & Ker, 2008). In controlled heating samples, goethite and kaolinite were no longer detected at temperatures above 250 and 530°C, respectively. Possible transformations are kaolinite dehydroxylation at 500°C and goethite to hematite transformation at 280°C (Ketterings, Bigham & Laperche, 2000). Gibbsite was not detected in CP1 above 250°C, which may be due to dehydroxylation at 200°C (Yusiharni & Gilkes, 2010). Other crystalline phases such as ilmenite, magnetite, and maghemite were investigated. However, they were not detected in the studied soil samples. As the fine (i. e., clay) fraction was not isolated and studied separately, some phases may not be detected by XRD (Araya et al., 2016).

Figure 17 presents XRD patterns for unburned, burned, and controlled-heated CSB aliquots (illustrate the general behavior of controlled-heated aliquots). The PCA developed with the peak intensities of the minerals indicated that the collection site and the temperature of heating play an important role in the soil characteristics, as the principal components grouped the samples according to such soil features. The preprocessing employed was autoscale. Three principal components were selected, totalizing 77.8% of explained variance. Figure 18 presents the biplots of PCA analysis for PC1 x PC2.

Figure 17 – XRD patterns of (a) unburned and fire-burned samples (F1, F2, CP1, CP2, CSB, and RB1 to RB6), and (b) slash-and-burn sample (CSB) in different temperatures (25 to 800°C). Kaolinite (K), gibbsite (Gb), goethite (Gt), anatase (A), hematite (H) and quartz (Q) most intense peaks were labeled. The quartz peak at $2\theta = 26.7^\circ$ extrapolated the y-scale



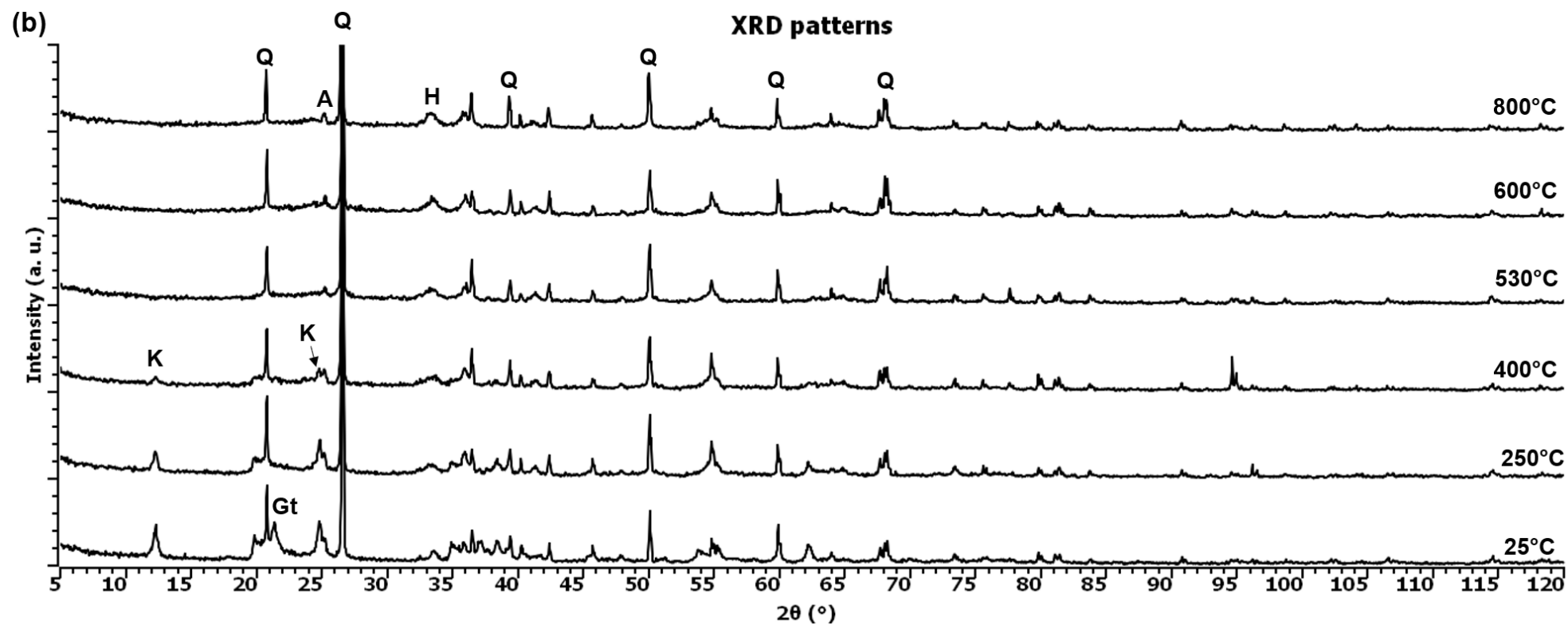
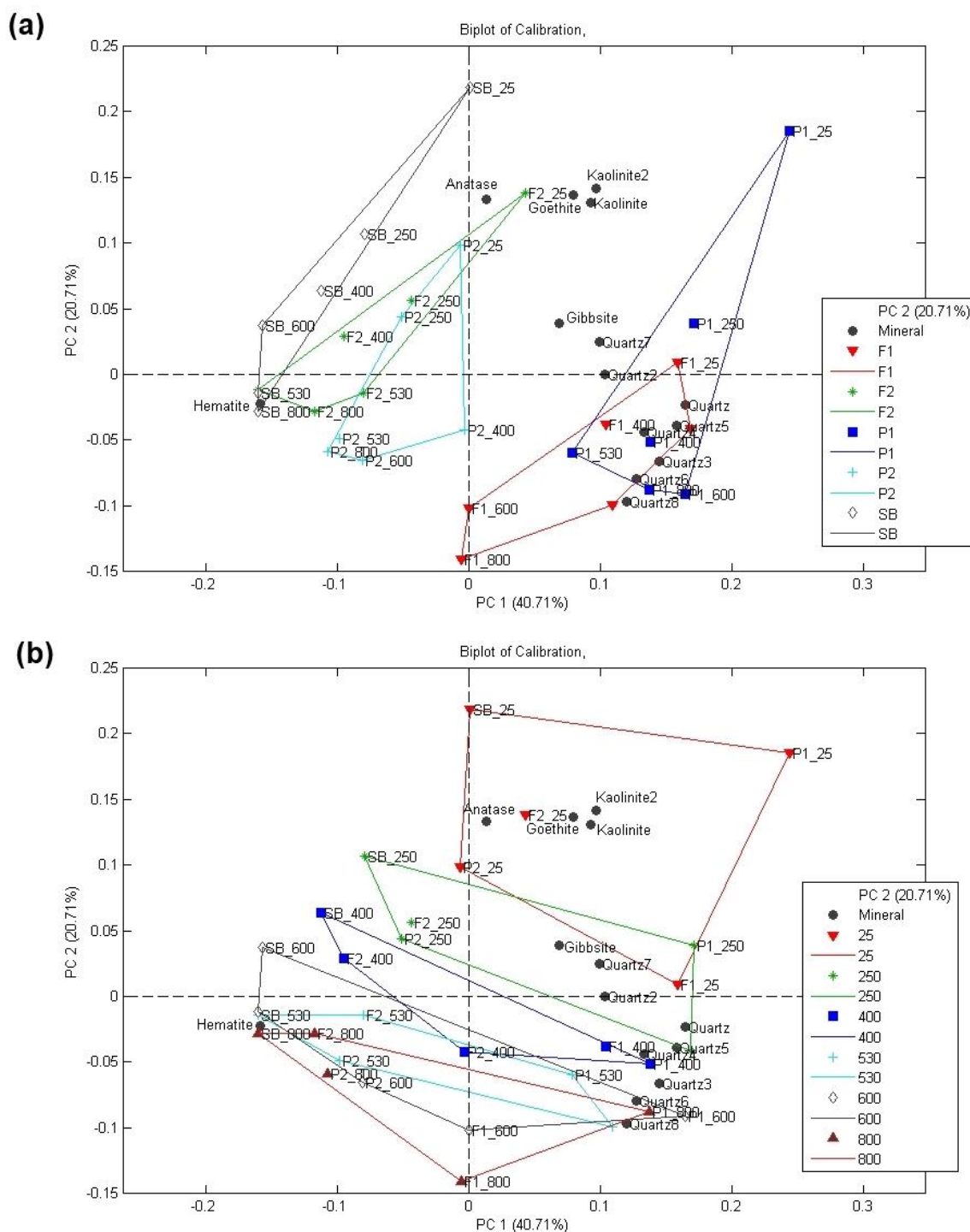


Figure 18 - PCA biplots performed with XRD intensities. (a) PC1 x PC2, grouped by collection sites and (b) PC1 x PC2, grouped by heating temperature. The number after the mineral name indicates some other peak that characterize the same mineral in the XRD pattern



PC1 (40.71% of explained variance) indicates different collection sites, with F1 and P1 in the positive portion, and F2, P2 and SB in the negative portion (higher hematite content). PC2 (20.71% of explained variance) indicates the heating temperatures, with lower temperatures in the positive portion (kaolinite, anatase,

goethite, and gibbsite) and higher temperatures in the negative portion (quartz and hematite are still detected in high temperatures).

5.7 VISIBLE NEAR-INFRARED

Vis-NIR spectra were acquired as $\log(1/\text{reflectance})$ and then transformed to reflectance and normalized to analyze the bands according to the literature. The bands identified in the spectra are associated with different minerals (Post and Noble, 1993; Ramarosan et al., 2018, Coblinski et al, 2021). Hematite and goethite bands occur due to Fe^{3+} electronic transitions. The absorption bands of goethite occur near 420, 480, 660 and 930 nm. Hematite is characterized by a band with very low reflectivity at 510 nm, a shoulder centered near 620 nm, and a reflectivity minimum near 880 nm. Different Fe oxides have different wavelength responses, according to their mineral structure. Their bands weakly absorb in the Vis-NIR range, while clay minerals such as phyllosilicates have distinct spectral signatures in the Vis-NIR region (Stenberg et al., 2010). Soil organic matter influences mainly between 400 and 1350 nm, reducing the reflectance and masking the bands related to Fe-oxyhydroxi minerals (Benedet et al., 2022). Kaolinite bands occur at 1400 nm and 2200 nm. The first band is associated with overtones of O-H stretching vibration (transition between vibrational levels of energy, above or below the original level), and the second one is due to OH-Al bend plus OH stretch combinations. Gibbsite band occurs at 2265 nm due to vibration of OH^- combined with Al. The band at 1900 nm is due to water (Genú, Demattê, & Fiorio, 2010). Figure 19 presents the Vis-NIR spectra of the F2 aliquots (from 50 to 750°C) heated in muffle, and Figure 20 the Vis-NIR spectra of the RB samples.

Figure 19 - Vis-NIR reflectance spectra of controlled-heat F2 aliquots, from 50 to 750°C. The 25°C aliquot was not heated

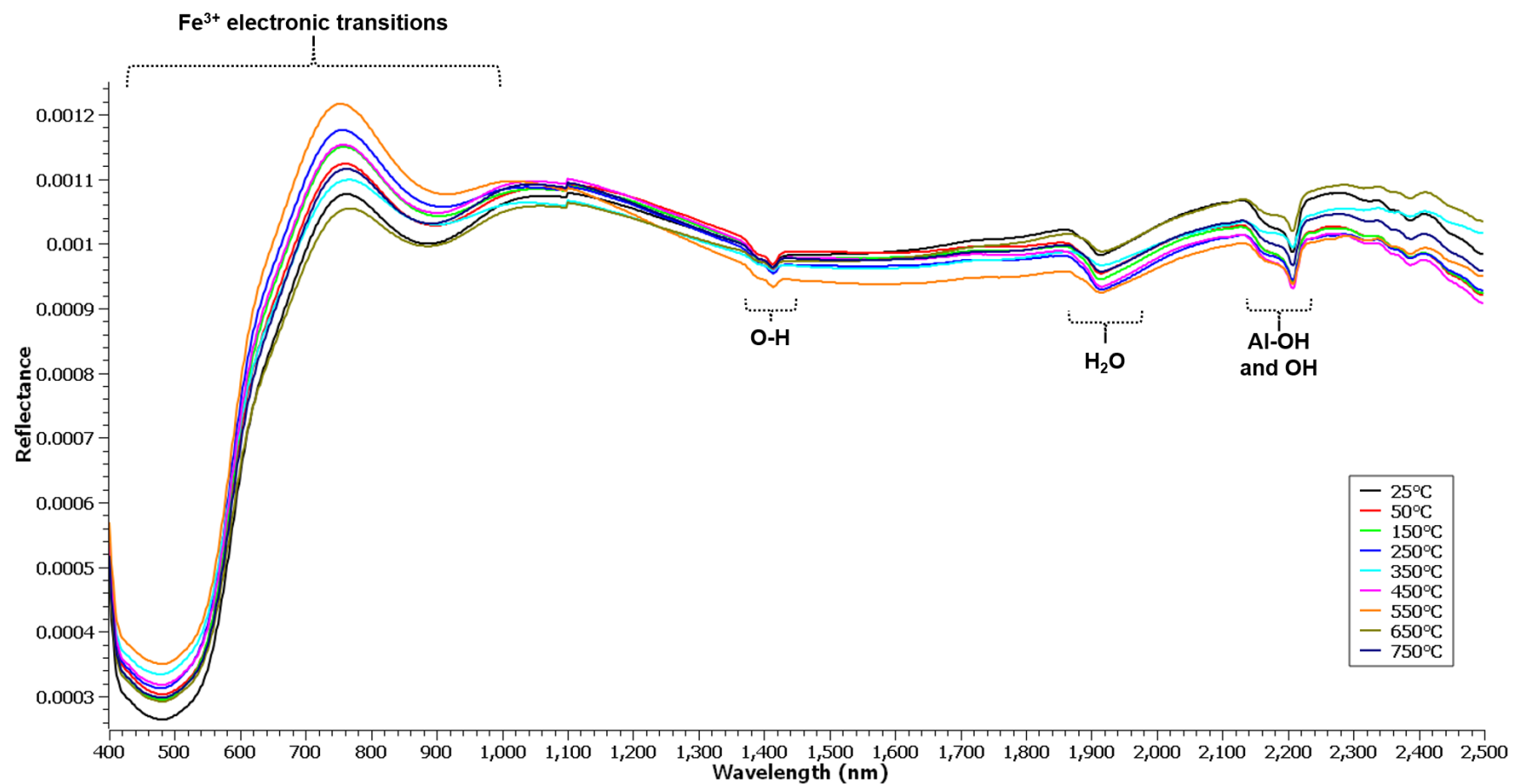
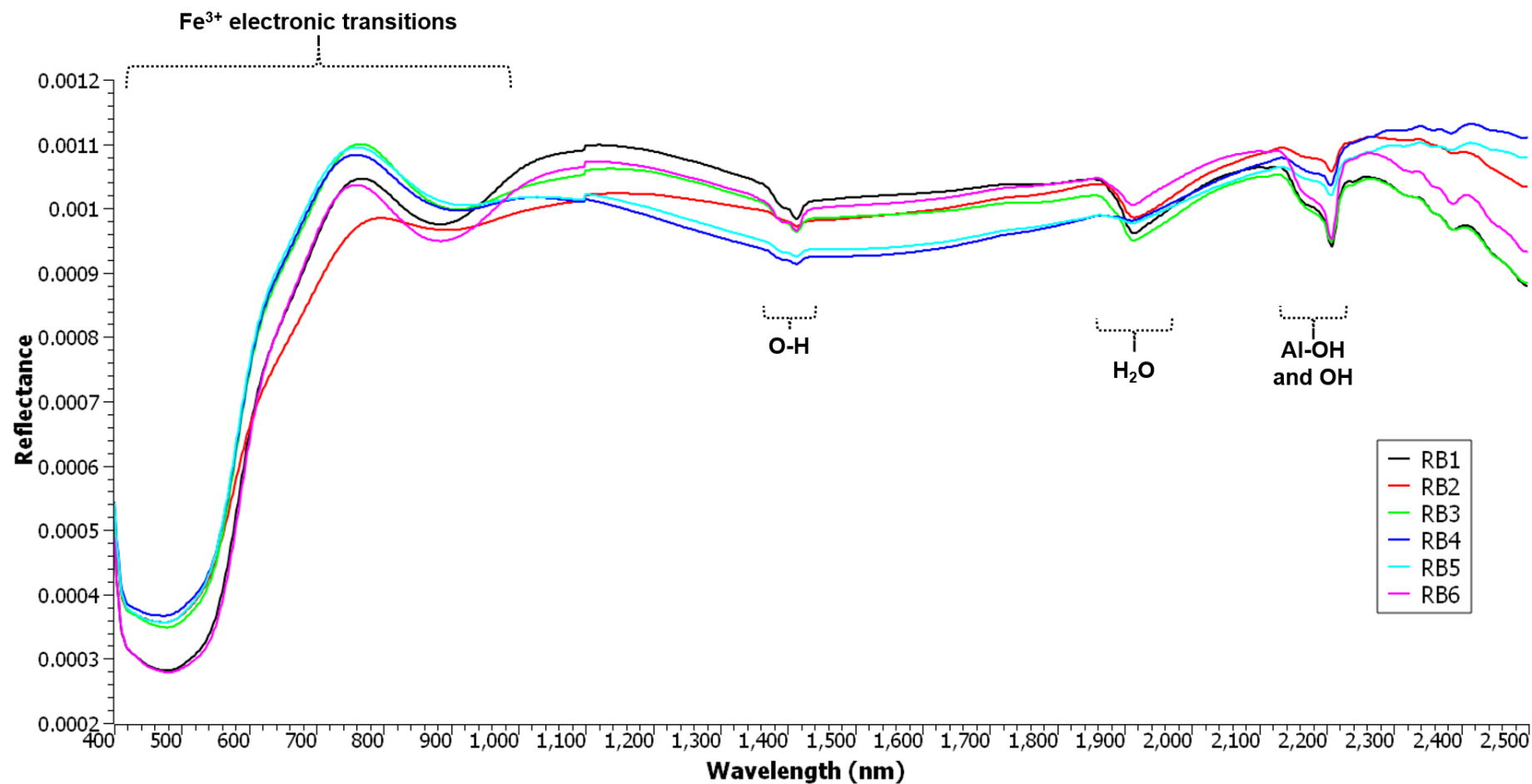
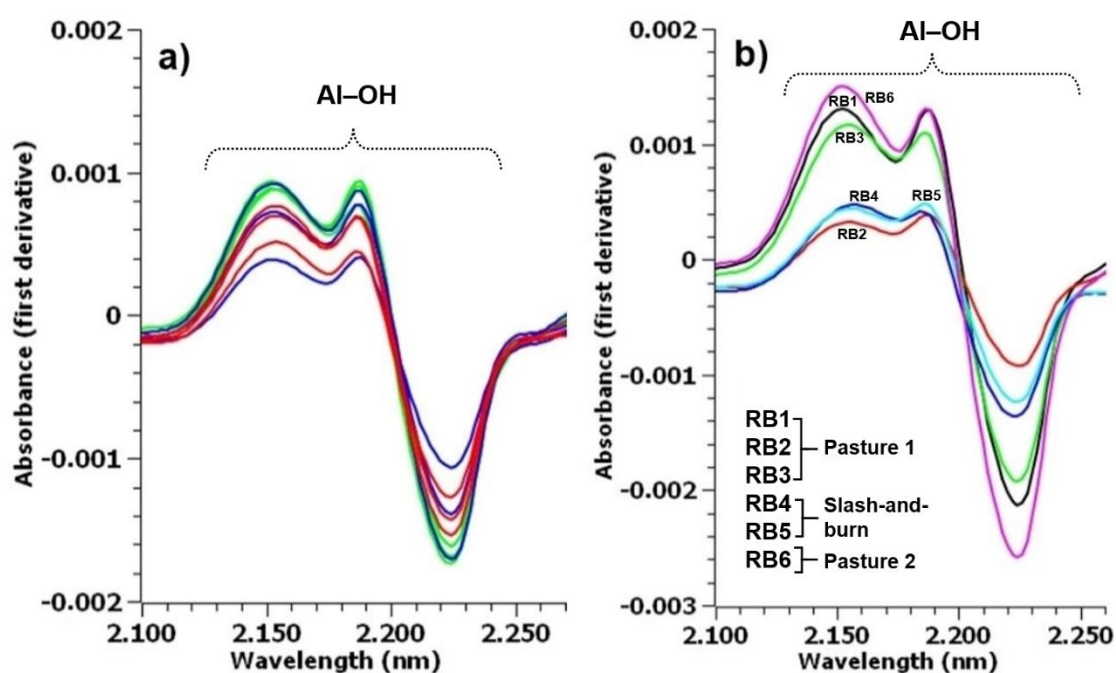


Figure 20 - Vis-NIR reflectance spectra of burned samples (RB) from pasture 1 (RB1, RB2 and RB3), slash-and-burn (RB4 and RB5), and pasture 2 (RB6)



In addition, the first derivative preprocessing was employed (Savitzky-Golay, 25 points), as performed by Pérez-Bejarano and Guerrero (2018), using the absorbance spectra. Figure 21(a) presents Al-OH band region in F2 controlled-heated aliquots, and Figure 21(b) presents fire-burned samples in the same wavelength region.

Figure 21 – Vis-NIR absorbance graphs. (a) controlled-heated samples F2, ranging from 25°to 150°C (green lines), from 250 to 450°C (blue lines) and from 550 to 750°C (red lines), Al-OH band region. (b) Fire-burned samples from pasture 1 (RB1, RB2, and RB3), pasture 2 (RB6), and slash-and-burn (RB4 and RB5) sites, Al-OH band region



In general, lower temperature levels (green lines in Figure 21(a)) presented higher absorbance than medium (blue lines in Figure 21(a)) and high temperature levels (red lines in Figure 21(a)). It suggests that the Al-OH absorption band had a decreasing trend as temperature increased. Fire-burned samples in Figure 21(b) also presented differences among the absorbance intensities. Slash-and-burn samples presented low intensity peaks (RB4 and RB5). It strongly suggests such samples were burned at high temperatures ($> 500^{\circ}\text{C}$). Heat has been observed to collapse some 2:1 type phyllosilicates, and destroy kaolinite between 500 and 700°C (Ketterings, Bigham & Laperche, 2000).

6 DISCUSSION

The differences between 0 – 5.0 cm and 5.0 – 10.0 cm in soil is not very expressive in soil science, except in studies concerning about soil organic matter. However, the quantitative results from EDXRF analysis demonstrated that the soil elemental composition changed according to the collection depth (Figure 11). The greatest difference between 0 to 5.0 and 5.0 to 10.0 cm layers was found for Ca in all studied sites. Ca content was higher in the superficial (0 – 5.0 cm) samples. Notable differences were also found for K and Mn contents, both presenting higher contents in the superficial soil layer. In general, following the burning there is a relative increase of nutrients P, K, Ca and Mg in ash and superficial layer. Thomaz, Doerr and Antonelli (2014) found that after rainfall K is rapidly transferred from the ash to the soil and leached to greater depths, while Ca and P are leached slower. In addition, it was observed that soil samples from pasture 1 (CP1, RB1, RB2, RB3) have different behavior than samples from other sites, mainly for K, Ti, Fe, and Zr. It strongly indicates that such samples have materials from different origin.

The PCA performed with the elemental concentrations (Figure 12) presented a tendency of grouping the samples by their collection sites (PC1 x PC2, and PC1 x PC3), indicating that the soil characteristics and land use type are the most significant features when analyzing the composition of the studied soils with EDXRF. The groups formed according to heating temperature (PC2 x PC3) were not as expressive as the ones formed by collection sites. Regarding to the PCA performed with the spectra, the COW alignment was fundamental. As the PCA seeks for data slight variations, the lack of alignment, even small, may alter the results. In general, PCA discriminated soils by their different composition, which depends mainly on their collection sites.

PLS estimated temperatures ranged from 325 to 608°C in fire-burned samples, a temperature range which has been reported elsewhere (Ketterings, Bigham & Laperche, 2000; Santín & Doerr, 2016; DeBano et al., 1998; Alcañiz et al., 2018; Badía et al., 2017; Busse et al., 2005). Multivariate analysis proved to be essential in the soil samples analyses. The EDXRF measurements combined with PCA were efficient to characterize different collection sites, which was not possible by means of thermal analysis or XRD alone. The 50 kV condition of EDXRF measurements presented the best calibration and estimation results.

As the PLS models were developed considering a single exposition time per controlled temperature, there might be some discrepancies when EDXRF results are compared with XRD and Vis-NIR results. Some heat-induced changes in soils depend on temperature as well as on exposition time (not investigated in this study). RB1, RB4, RB5 and RB6 samples had their estimated temperature above 500°C by PLS models (Table 5). Thus, kaolinite was not expected to be present in such samples. However, kaolinite was detected by XRD peak (Figure 17) and Vis-NIR Al-OH band (Figure 21) in samples RB1 to RB6. Such result suggests that the exposition time to extinguish all kaolinite present in the fire-burned samples was not enough. As the samples burned in field could have been exposed to heat during 1, 5, 10, or 20 min, etc. (in a real situation, we often do not know such information), the different exposition times should be taken into consideration. Aiming to improve the analyses in the next studies, the exposition time must be considered in the PLS models development, for instance, burning the samples during 1, 5, 10 and 20 min at each temperature and including them all in the models. Other possible phenomenon generating the discrepancy in the results is that the kaolinite detected by XRD and Vis-NIR may be present in the silt and sand fraction of soils (Aburto & Southard, 2016), being not extinguished in the muffle heating.

When analyzing soil samples, the EDXRF measurements can be influenced by moisture content (which affects the accuracy), by physical-matrix effects (soil particle size, homogeneity, surface conditions), and by chemical-matrix effects (interfering elements, e. g. Fe reduces Cu but enhances Cr measurements) (Peinado et al., 2010; Stockmann et al., 2016; Freitas et al., 2021). Also, finding a realistic way to burn the samples in the laboratory is challenging. Most laboratory studies have used sieved or disturbed soils rather than undisturbed soils (Wieting, Ebel and Singha, 2017), and experimental burning tends to increase the effects on soil properties (Thomaz, 2021). Influences caused by the diffusion of oxygen during wildfires can be different when compared to controlled heating in laboratory. Differences due to samples heterogeneity can also interfere in the analyses. Such effects should be taken into account before extrapolating their results to field burnings, either controlled or not.

Thermal analysis indicated the main transformations in the studied soils. In general, the samples had similar behavior. Until 125 °C, they lost solvation water. Then, in the range 125 to 200°C, hygroscopic water (2:1 solvated cations) was lost and lighter compounds as P and S volatilized. From 190 to 320°C the organic

matter decomposed and the lighter compounds volatilized. Gibbsite and goethite dehydroxylates in the range from 250 to 430°C. C oxidation occurred in the same range. From 420 to 580°C, kaolinite dehydroxylated.

Regarding to Munsell colors, unburned samples from pasture 1 and slash-and-burn presented 100% yellow in hue. Sample CP2 presented 25-50% of red in its hue, and is more similar to forest samples (F1 and F2), as its location is nearer to forests (Figure 9). The value ranged between 3 (darker color) to 6 (lighter color), and the chroma between 2 (lower saturation) to 8 (higher saturation). Now, for controlled burning samples, only forest F2 aliquots were analyzed. The controlled-burning soil presented 75% of yellow and 25% of red in hue until 150°C. Then, for higher temperatures, the hue became 25% of yellow and 75% of red. The reddening was reported in previous studies (Giovannini et al., 1988; Ketterings and Bigham, 2000; Ulery and Graham, 1993), and it is related to iron oxides transformations (p. e. maghemite and hematite). The soil became darker, and the value decreased for temperatures near to 250°C due to organic matter decomposition. The value increased again after 550°C, as all organic matter was consumed. The chroma decreased at 150°C, also due to organic matter decomposition, and increased after 350°C, as the organic matter was consumed and the soil became lighter and redder. Such temperature ranges and observed colors (transformation indicators) agreed with the transformations observed in the thermal analysis.

Determining the magnetic susceptibility χ_{LF} is a very sensible method to measure the magnetic behavior of soil and, in general, values χ_{LF} found in this study were low, indicating a small content of magnetic minerals in the investigated soils. The presence of these minerals in some samples is justified by the fact that they can occur naturally in Oxisols, or be formed after heating (Schaefer et al., 2008). The heating temperature is an important factor to be considered, because after a certain temperature threshold, maghemite and magnetite may transform to a more stable Fe oxide, hematite, which is not magnetic (Nonaka et al., 2017). Also, it was observed that pure goethite dehydroxylates to hematite between 200 and 400°C, and if additional organic carbon is added, maghemite is formed (Hanesch, Stanjek & Petersen, 2006). This explains the higher χ_{LF} for F2 samples from room temperature to 400 °C (maghemite presence) and lower χ_{LF} at 800 °C (hematite formed). In addition, the pasture 1 presented the lowest χ_{LF} values, indicating that the heating temperature were lower in these burned samples. Higher χ_{LF} values found for slash-and-burn indicate

higher burning temperature in such site.

The minerals detected by XRD were hematite, quartz, kaolinite, anatase, goethite and gibbsite. The main transformation observed was goethite and kaolinite dehydroxylation. Such phases were not detected after 250 and 530°C, respectively. Gibbsite also dehydroxylated and was not detected above 250°C in pasture 1 samples, the only site that presented such mineral. Pasture 1 did not present goethite neither hematite, indicating different origin material than other samples. It was observed also in the quantitative results of EDXRF measurements (Figure 11). The PCA distinguished the samples by their collection site (PC1) and presented a tendency to group the samples by their heating temperature (PC2), Figure 18. The Vis-NIR spectra were very similar for all the F2 heated aliquots (50-750°C), presenting small changes between different temperature levels (Figure 19). Higher temperatures spectra presented smaller absorbance of Al-OH band, what indicates the decreasing of kaolinite and gibbsite content (Figure 21). RB samples demonstrated strong differences between samples, and this behavior is related to the different collection sites.

7 CONCLUSIONS

Maximum temperatures reached during fire in soil samples classified as Red-Yellow Latosol have been investigated by multi-techniques, and an innovative methodology to determine the maximum temperature reached in soil was performed. The best PLS models were the ones employing 50 kV EDXRF spectra and using Pareto as preprocessing method. The accuracy of model 6, which was developed to estimate fire-burned samples, was inferred by the development of five different models with cross-validation made in blocks, including data from the five studied areas. The highest estimated temperature was 608°C in the slash-and-burn site (sample RB5), and the lowest one was 325°C in pasture 1 (RB2 sample). The results of such methodology indicated that the temperature estimation is feasible by using EDXRF data and multivariate analysis. The PCA with EDXRF data was efficient to characterize the samples from different collection sites, and presented a tendency of grouping the samples of different heating temperatures.

Thermal analysis was efficient to determine the mass loss and the reactions induced in soils by heat, mainly the OM decomposition (200 – 320°), the C oxidation, gibbsite and goethite dehydroxylation (250 – 430°C), and the kaolinite dehydroxylation (420 – 580°C). Soil colors were determined by the Munsell color chart, confirming the transformations observed in the thermal analysis (organic mass decomposition, mineral transformations). Measuring the magnetic susceptibility was efficient to verify the weak magnetic behavior of the studied soils, indicating a small quantity of maghemite. Soil mineralogy was determined by XRD measurements, as well as the mineralogical transformations due to heating (dehydroxylation of goethite, gibbsite and kaolinite at 250, 250 and 530°C, respectively). Vis-NIR confirmed the presence of kaolinite in all soils and presented no significative differences between the temperature levels of controlled-heated F2 aliquots. The apparent discrepancies found when comparing the temperatures estimated by EDXRF models with XRD and Vis-NIR results were mainly a consequence of exposure time limitations (a single exposure time of 20 min was studied). In future studies, a wider range of exposition time should be included in the multivariate models to improve the temperature estimations.

Acquiring fire intensity-severity information from soil after a burn event is a challenge. Innovative analytical methodologies development is fundamental for such investigation to evolve.

8 SCIENTIFIC PRODUCTION

Publications, events and projects developed during the PhD:

Sandwich internship grant (CNPq): “Physical-chemical evaluation of Amazonian burned soils”. Universidad Miguel Hernández, Elche, Spain. Approved by CNPq: September 2020. Executed: from October 01, 2021 to March 31, 2022.

Published article:

Rocha, D. R., Melquiades, F. L., Thomaz, E. L. (2019). Modeling the soil burn effect for temperature prediction by energy dispersive X ray Fluorescence in an haplic cambisol soil. Applied Radiation and Isotopes 150, 26-30. DOI: <https://doi.org/10.1016/j.apradiso.2019.05.012>.

Submitted article:

Rocha, D. R., Thomaz, E. L., Urbano, A., Vendrame, P. R. S., Melquiades, F. L. Multi-technique analysis to estimate the maximum temperature reached in burned soils from an Amazonian region. **Submitted to Journal of Environmental Quality.**

Articles under elaboration:

Rocha, D. R., Valles, J. X. B., Vidal, M. M. J., Urbano, A., Melquiades, F. L., Thomaz, E. L., Mataix-Solera, J. Multivariate analysis with XRD data as a fingerprinting technique to study burned soils. **Being elaborated to Minerals journal.**

Rocha, D. R., Melquiades, F. L., Thomaz, E. L., Mataix-Solera, J. Multivariate models to estimate the maximum temperature of burned soils: grain size effects.

Participation in events and presentations:

Rocha, D. R., Melquiades, F. L., Thomaz, E. L. Estudio de los cambios inducidos por el fuego en el suelo con EDXRF y predicción de la temperatura máxima después del incendio con análisis multivariante. Communication, Universidad Miguel Hernández, Elche, Spain, 2021.

Rocha, D. R., Melquiades, F. L., Thomaz, E. L. Multivariate calibration employing energy dispersive X-ray fluorescence data to predict the maximum temperature reached in a Ferralsol after burning. 8th International Conference on Fire Effects on Soil Properties (FESP8), 2021.

Ribeiro, J. V., Rocha, D. R., Melquiades, F. L. Caracterização de sedimentos finos em uma bacia rural por fluorescência de raios-X por dispersão de energia. Encontro Anual de Iniciação Científica da UEL, 2020, Londrina. Anais do encontro anual de iniciação científica da UEL, 2020. v. 01. p. 01-02.

Ribeiro, J. V., Rocha, D. R., Melquiades, F. L., Antonelli, V., Thomaz, E. L. Energy dispersive X-ray fluorescence for sediment characterization in a rural basin with Tobacco plantation. XLIII Reunião de Trabalho sobre Física Nuclear no Brasil, Brazilian Physical Society, 2020.

Virtuel: refletindo e capacitando. Laboratório de Tecnologia Educacional, UEL, 2020.

Rocha, D. R., Thomaz, E. L., Melquiades, F. L. Estimativa de temperatura máxima atingida por solos submetidos a queimadas empregando regressão por mínimos quadrados parciais. XI Workshop de Quimiometria, Universidade Estadual da Paraíba, 2020.

Rocha, D. R., Melquiades, F. L., Thomaz, E. L. Characterization of Rondônia soils submitted to fire using Energy Dispersive X Ray Fluorescence technique. Symposium INCT-FNA, UFF, 2019.

Rocha, D. R., Melquiades, F. L. Caracterização por Fluorescência de Raios X por Dispersão De Energia de Solos Submetidos a Queimadas. XXIV Semana da Física, UEL, 2019.

Rocha, D. R., Melquiades, F. L., Thomaz, E. L. Study of the soil burn effect by energy dispersive X-ray fluorescence in an humic cambisol soil. XVI Conferencia Latinoamericana de Análisis por Técnicas de Rayos X, 2018, Pucón. Resumen SARX JFMF 2018, 2018.

REFERENCES

- ABURTO, F. A., SOUTHARD, R. J. Thermal Analysis Mineral Quantification and Applications as a Relative Dating Tool in Moraine Chronosequences. *Soil Sci. Soc. Am. J.* 80:502–515, doi:10.2136/sssaj2015.08.0307, 2016.
- ALCAÑIZ, M., OUTEIRO, L., FRANCOS, M., ÚBEDA, X. Effects of prescribed fires on soil properties: A review. *Science of the Total Environment* 613-614, 944-957. <https://doi.org/10.1016/j.scitotenv.2017.09.144>, 2018.
- ANDERSSON, M. A. A comparison of nine PLS1 algorithms. *Journal of Chemometrics*, v.23. <https://doi.org/10.1002/cem.1248>, 2009.
- ARAYA, S. N., MEDING, M., & BERHE, A. A. Thermal alteration of soil physico-chemical properties: a systematic study to infer response of Sierra Nevada climosequence soils to forest fires. *SOIL*, 2, 351-366, 2016.
- ARCENEGUI, V., MATAIX-SOLERA, J., ZORNOZA, R., PÉREZ-BEJARANO, A., MATAIX-BENEYTO, J., GÓMEZ, I. Estimation of the maximum temperature reached in burned soils using near-infrared spectroscopy: Effects of soil sample pre-treatments. *Geoderma* 158, 85–92, 2010.
- BADÍA, D., LÓPEZ-GARCÍA, S., MARTÍ, C., ORTÍZ-PERPIÑÁ, O., GIRONA-GARCÍA, A., CASANOVA-GASCÓN, J. Burn effects on soil properties associated to heat transfer under contrasting moisture content. *Science of the Total Environment* 601-602, 1119-1128, 2017.
- BEINROTH, F. H., ESWARAN, H., PALMIERI, F., REICH, P. F. Properties, classification and management of Oxisols. Monograph. Guy D. Smith Memorial Slide Collection, 1996.
- BENEDET, L., SILVA, S. H. G., MANCINI, M., TEIXEIRA, A. F. S., INDA, A. V., DEMATTÊ, J. A. M., CURI, N. Variation of properties of two contrasting Oxisols enhanced by pXRF and Vis-NIR. *Journal of South American Earth Sciences*, 115, 103748, doi: <https://doi.org/10.1016/j.jsames.2022.103748>, 2022.
- BURCHAM, W. Física nuclear. Reverte, 1974.
- BUSSE, M. D., HUBBERT, K. R., FIDDLER, G. O., SHESTAK, C. J., POWERS, R. F. (2005). Lethal soil temperatures during burning of masticated forest residues. *International Journal of Wildland Fire*, 14, 267-276, <https://doi.org/10.1071/WF04062>, 2005.
- CARVAJAL-RAMÍREZ, F., SILVA, J. R. M., AGUËRA-VEGA, F., MARTÍNEZ-CARRICONDO, P., SERRNAO, J., MORAL, F. J. Evaluation of Fire Severity Indices Based on Pre- and Post-Fire Multispectral Imagery Sensed from UAV. *Remote Sens.*, 11, 993. <http://doi:10.3390/rs11090993>, 2019.
- CARVALHO, M. A. C. C., PANOSSO, A. R., TEIXEIRA, E. E. R., ARAÚJO, E. G., BRANCAGLIONI, V. A. Multivariate approach of soil attributes on the characterization

of land use in the southern Brazilian Amazon. *Soil & Tillage Research* 184, 207-2015, 2018.

CERTINI, G. Effects of fire on properties of forest soils: a review. *Oecologia*, 143, 1-10, 2005.

CLAESSEN, M. E. C. *Manual de Métodos de Análise de Solo*, 2nd ed., Embrapa-CNPS: Rio de Janeiro, 1997.

COBLINSKI, J. A., INDA, A. V., DEMATTÊ, J. A. M., DOTTO, A. C., GHOLIZADEH, A., GIASSEN, E. Identification of minerals in subtropical soils with different textural classes by VIS–NIR–SWIR reflectance spectroscopy. *Catena*, V. 203, 105334, doi: <https://doi.org/10.1016/j.catena.2021.105334>, 2021.

COOPER, F. G. *Munsell Manual of Color*. Munsell Color Company, Inc. Baltimore, Maryland, USA, 1929.

CRITTER S. A. M., AIROLDI, C. Thermal Analysis of Brazilian Tropical Soils Originating from Different Sources. *J. Braz. Chem. Soc.*, Vol. 17, No. 7, 1250-1258, 2006.

DEARING, J. *Environmental Magnetic Susceptibility. Using the Bartington MS2 System*. © Instruments. GMW Associates, 955 Industrial Road, San Carlos, CA, 94070 USA, ISBN 0 9523409 0 9, 1994.

DEBANO, L. F., NEARY, D. G., FFOLLIOTT, P. F. *Fire's Effects on Ecosystems*. John Wiley & Sons, New York, NY. 331p., ISBN: 978-0-471-16356-5, 1998.

DE JONG, S. SIMPLS: an alternative approach to partial least squares regression. *Chemom. Intell. Lab. Syst.* 1993; 18: 251–263, [https://doi.org/10.1016/0169-7439\(93\)85002-X](https://doi.org/10.1016/0169-7439(93)85002-X), 1993.

DOMENÉCH-CARBÓ, M. T., & OSETE-CROTINA, L. Another beauty of analytical chemistry: chemical analysis of inorganic pigments of art and archaeological objects. *ChemTexts*, 2(14), 2016.

EMBRAPA, dos SANTOS, H. G. et al. *Sistema Brasileiro de Classificação de Solos*. Ed. 5, 2018.

EMBRAPA, *Guia de campo da XII Reunião Brasileira de Classificação e Correlação de Solos: RCC de Rondônia*. 2019.

FAO, *World reference base for soil resources 2014, Update 2015. International soil classification system for naming soils and creating legends for soil maps. World Soil Resources Reports*. 2015.: ISSN 0532-0488

FERREIRA, M. M. C., ANTUNES, A. M., MELGO, M. S. & VOLPE, P. L. O. *Quimiometria I: calibração multivariada, um tutorial*. Quím. Nova vol.22 n.5, 1999.

FERREIRA, M. M. C. *Quimiometria. Coinceitos métodos e Aplicações*. Editora

Unicamp, 2015.

FREITAS, M. G., SANTOS, F. R., PARREIRA, P. S., MELQUIADES, F. L. Influence of soil sample grain size on energy dispersive X-ray fluorescence analysis: a comparative study case with three spectrometers. *Spectroscopy Letters*, vol. 54, 7, 2021.

GENÚ, A. M., DEMATTÊ, J. A. M., FIORIO, P. R. Spectral analysis of soils from Mogi-Guaçu (SP) Region. *Semina: Ciências Agrárias, Londrina*, v. 31, suplemento 1, p. 1235-1244, 2010.

GUEMBOU, J. C. S., NDONTCHUENG, M. M., CHENE, G., NGUELEM, J. E. M., MOTAPON, O., STRIVAY, D. Simultaneously gamma spectrometry & energy dispersive X-ray fluorescence-based color differentiation analysis of Douala-Bassa area's soil. *Environmental Technology & Innovation*, 16, 100486, <https://doi.org/10.1016/j.eti.2019.100486>, 2019.

GIOVANNINI, G., LUCCHESI, S., GIACHETTI, M. Effect of heating on some physical and chemical parameters related to soil aggregation and erodibility, *Soil Sci.*, 146, 255–261, doi:10.1097/00010694-198810000-00006, 1988.

GLAZER, M. Notes about the Bragg's first paper. The Two Braggs Exhibition, Warwick University, 2013. Mike Glazer's Programs. <<https://www.amg122.com/twobraggs/firstpaper-mini.pdf>>. Retrieved Sep, 2020.

GRISI, B., GRACE, C., BROOKES, P. C., BENEDETTI, A., DELL'ABATE, M. T. Temperature effects on organic matter and microbial biomass dynamics in temperate and tropical soils. *Soil Biol. Biochem*, Vol. 30, No 10/11, pp. 1309-1315, 1998.

GUERRERO, C., MATAIX-SOLERA, J., ARCENEGUI, V., MATAIX-BENEYTO, J. & GOMEZ I. Near-infrared spectroscopy to estimate the maximum temperatures reached on burned soils. *Soil Science Society of America Journal*. 71:1029–1037, 2007.

HANESCH, M., STANJEK, H., PETERSEN, N. Thermomagnetic measurements of soil iron minerals: the role of organic carbon. *Geophys. J. Int.* 165, 53-61, 2006.

HARRIS, L. A. Polymer Stabilized Magnetite Nanoparticles and Poly(propylene oxide) Modified Styrene-Dimethacrylate Networks. Dissertation Submitted to the Faculty of the Virginia Polytechnic Institute and State University, 2002.

JAVADI, S. H., MUNNAF, M. A., MOUAZEN, A. M. Fusion of Vis-NIR and XRF spectra for estimation of key soil attributes. *Geoderma*, 385, 114851, <https://doi.org/10.1016/j.geoderma.2020.114851>, 2021.

JIMÉNEZ-PINILLA, P., MATAIX-SOLERA, J., ARCENEGUI, V., DELGADO, R., MARTÍN-GARCÍA, J. M., LOZANO, E., MATÍNEZ-ZAVALA, L. & JORDÁN A. Advances in the knowledge of how heating can affect aggregate stability in Mediterranean soils: a XDR and SEM-EDX approach. *Catena* 147 315-324, 2016.

KETTERINGS, Q. M., BIGHAM, J. M. & LAPERCHE, V. Changes in Soil Mineralogy and Texture Caused by Slash-and-Burn Fires in Sumatra, Indonesia. *Soil Science*

Society of America Journal, Volume 64, Issue 3, p. 1108-1117, <https://doi.org/10.2136/sssaj2000.6431108x>, 2000.

LUGASSI, R., BEN-DOR, E., ESHEL, G. Reflectance spectroscopy of soils post-heating — Assessing thermal alterations in soil minerals. *Geoderma* 213, 268-279, doi: <http://dx.doi.org/10.1016/j.geoderma.2013.08.014>, 2014.

MARCOS, E., FERNÁNDEZ-GARCÍA, V., FERNÁNDEZ-MANSO, A., QUINTANO, C., VALBUENA, L., TÁRREGA, R., LUIS-CALABUIG, E. & CALVO, L. Evaluation of Composite Burn Index and Land Surface Temperature for Assessing Soil Burn Severity in Mediterranean Fire-Prone Pine Ecosystems. *Forests*, 9, 494, 2018.

MARTINS, R. A. A Descoberta dos Raios X: O Primeiro Comunicado de Röntgen. *Revista Brasileira de Ensino de Física* vol. 20, no. 4, 1998.

MATAIX-SOLERA, J., ARCENEGUI, V., GUERRERO, C., JORDÁN, M.M., DLAPA, P., TESSLER, N., WITTENBERG, L. Can terra rossa become water repellent by burning? A laboratory approach. *Geoderma* 147 (3–4), 178–184, <https://doi.org/10.1016/J.GEODERMA.2008.08.013>, 2008.

MELO, V. F., ORRUTÉA, A. G., MOTTA, A. C. V., TESTONI, S. A. Land Use And changes in soil morphology and physical-chemical properties in southern Amazon. *Rev. Bras. Cienc. do Solo* 4, <https://doi.org/10.1590/18069657rbc20170034>, 2017.

MELQUIADES, F. L., THOMAZ, E. L. X-Ray Fluorescence to Estimate the Maximum Temperature Reached at Soil Surface during Experimental Slash-and-Burn Fires. *Journal of Environmental Quality*, 45(3):1104-9, 2016.

MERINO, A., FERREIRO, A., SALGADO, J., FONTÚRBEL, M. T., BARROS, N., FERNÁNDEZ, C. & VEJA, J.A. Use of thermal analysis and solid-state ¹³C CP-MAS NMR spectroscopy to diagnose organic matter quality in relation to burn severity in Atlantic soils. *Geoderma* 226–227:376–386, 2014.

MIYAZAWA, M. PAVAN, M. A., OLIVEIRA, E. L., IONASHIRO, M., SILVA, A. K. Gravimetric Determination of Soil Organic Matter. *Brazilian Archives of Biology and Technology*, v. 43, n. 5, p. 475-478, 2000.

MORAES, J. F. L., VOLKOFF, B., CERRI, C. C., BERNOUX, M. Soil properties under Amazon forest and changes due to pasture installation in Rondônia, Brazil. *Geoderma* 70, 63–81, [https://doi.org/10.1016/0016-7061\(95\)00072-0](https://doi.org/10.1016/0016-7061(95)00072-0), 1996.

MOYA D., GONZÁLEZ-DE VEGA, S., LOZANO, E., GARCÍA-ORENES, F., MATAIX-SOLERA, J., LUCAS-BORJA, M. E. & DE LAS HERAS, J. The burn severity and plant recovery relationship affect the biological and chemical soil properties of *Pinus halepensis* Mill. stands in the short and midterms after wildfire. *Journal of Environmental Management* 235 250-256, 2019.

NASCIMENTO FILHO, V. F. Técnicas analíticas nucleares de fluorescência de raios X por dispersão de energia (EDXRF) e por reflexão total (TXRF). Piracicaba: ESALQ, Depto. de Física e Meteorologia; CENA, 1999.

National Park Service, Wildfires, Prescribed Fires, and Fuels. <<https://www.nps.gov/orgs/1965/wildfires-prescribed-fires-fuels.htm>>. Retrieved Jan, 2021.

NONAKA, A. G., BATISTA, M. A., COSTA, A. C. S. da, INOUE, T. T. BONADIO, T. G. M., SOUZA JUNIOR, I. G. de. Kinetics of Thermal Transformation of Synthetic Al-Maghemites into Al-Hematites. *Rev. Bras. Cienc. Solo*, 41:e010384, 2017.

OLIVEIRA, J. R. B., RIBAS, R. V. & SOUZA, A. F. Modern Physics' Laboratory notes. Universidade de São Paulo, Instituto de Física, 2009.

PASQUINI, C. Near Infrared Spectroscopy: Fundamentals, Practical Aspects and Analytical Applications, *J. Braz. Chem. Soc.*, Vol. 14, No. 2, 198-219, 2003.

PEINADO, F. M., RUANO S. M., GONZÁLEZ, M. G. B., MOLINA, C.E., A rapid field procedure for screening trace elements in polluted soil using portable X-ray fluorescence (PXRF). *Geoderma* 159, p. 76-82, 2010.

PEREIRA, A. M. R. Estudo do Impacto da Descoberta dos Raios-X e das suas Aplicações Médicas em Portugal. Master thesis in chemistry, Universidade de Lisboa, 2012.

PÉREZ-BEJARANO, A., GUERRERO, C. Near infrared spectroscopy to quantify the temperature reached in burned soils: Importance of calibration set variability. *Geoderma* 326 133-143, 2018.

PLANTE, A. F., FERNÁNDEZ, J. M., & LEIFELD, J. Application of thermal analysis techniques in soil science. *Geoderma* 153, 1-10, 2009.

POPPIEL, R. R., LACERDA, M. P. C., RIZZO, R., SAFANELLI, J. L., BONFATTI, B. R., SILVERO, N. E., DEMATTÊ, J. A. M. Soil Color and Mineralogy Mapping Using Proximal and Remote Sensing in Midwest Brazil. *Remote Sens.* 12, 1197, doi:10.3390/rs12071197, 2020.

POST, J.L., NOBLE, P.N. The near-infrared combination band frequencies of dioctahedral smectites, micas, and illites. *Clays and Clay Miner.* 41, 639–644, <https://doi.org/10.1346/CCMN.1993.0410601>, 1993.

RAMAROSON, V. H., BECQUER, T., SÁ, S. O., RAZAFIMAHATRATRA, H., DELARIVIÈRE, J. L., DIDIER BLAVET, D., VENDRAME, P. R. S., RABEHARISOA, L., RAKOTONDRAZAFY, A. F. M. Mineralogical analysis of ferrallitic soils in Madagascar using NIR spectroscopy. *CATENA*, volume 168, pages 102-109, <https://doi.org/10.1016/j.catena.2017.07.016>, 2018.

ROCHA, D. R., MELQUIADES, F. L. THOMAZ, E. L. Modeling the soil burn effect for temperature prediction by energy dispersive X ray Fluorescence in an haplic cambisol soil. *Applied Radiation and Isotopes* 150, 26-30, 2019.

SANTÍN, C. & DOERR, S. H. Fire effects on soils: The human dimension. *Phil. Trans.*

R. Soc. B 371: 20150171, <https://doi.org/10.1098/rstb.2015.0171>, 2016.

SCHAEFER, C. E. G. R., FABRIS, J. D. & KER, J. C. Minerals in the clay fraction of Brazilian Latosols (Oxisols): a review. *Clay Minerals*, 43, 137–154, <https://doi.org/10.1180/claymin.2008.043.1.11>, 2008.

SOUZA, E. S., FERNANDES, A. R., BRAZ, A. M. S., OLIVEIRA, F. J., ALLEONI, L. R. F. & CAMPOS, M. C. C. Physical, chemical, and mineralogical attributes of a representative group of soils from the eastern Amazon region in Brazil. *SOIL*, 4, 195–212, 2018.

STENBERG, B., ROSSEL, R. A. V., MOUAZEN, A. M. & WETTERLIND, J. Visible and Near Infrared Spectroscopy in Soil Science. Donald L. Sparks, *Advances in Agronomy*, Vol. 107, Burlington: Academic Press, pp. 163-215. [http://dx.doi.org/10.1016/S0065-2113\(10\)07005-7](http://dx.doi.org/10.1016/S0065-2113(10)07005-7), 2010.

STOCKMANN, U., JANG, H. J., MINASNY, B., MCBRATNEY, A. B. Chapter 5: The Effect of Soil Moisture and Texture Fe Concentration Using Portable X-Ray Fluorescence Spectrometers. *Digital Soil Morphometrics*, Springer. http://doi.com/10.1007/978-3-319-28295-4_5, 2016.

TAVARES, T. R., MOUAZEN, A. M., ALVES, E. E. N., DOS SANTOS, F. R., MELQUIADES, F. L., DE CARVALHO, H. W. P., MOLIN, J. P. Assessing Soil Key Fertility Attributes Using a Portable X-ray Fluorescence: A Simple Method to Overcome Matrix Effect. *Agronomy*, 10(6), 787, <https://doi.org/10.3390/agronomy10060787>, 2020.

THOMAZ, E. L., DOERR, S. H. & ANTONELLI, V. Effects of fire on the physicochemical properties of soil in a slash-and-burn agriculture. *Catena* 122, 209–215, 2014.

THOMAZ, E. L. High fire temperature changes soil aggregate stability in slash-and-burn agricultural systems. *Sci. Agric.* v.74, n.2, p. 157-162, <https://doi.org/10.1590/1678-992X-2015-0495>, 2017a.

THOMAZ, E. L. Realistic soil-heating gradient temperature linearly changes most of the soil chemical properties. *Soil Science and Plant Nutrition*, Vol. 63, No. 1, 84-91, <https://doi.org/10.1080/00380768.2016.1255538>, 2017b.

THOMAZ, E. L., NUNES, D. D., WATANABE, M. Effects of tropical forest conversion on soil and aquatic systems in southwestern Brazilian Amazonia: A synthesis. *Environmental Research*, 2020.

THOMAZ, E. L. Effects of fire on the aggregate stability of clayey soils: A meta-analysis. *Earth-Science Reviews*, 221, 103802. <https://doi.org/10.1016/j.earscirev.2021.103802>, 2021.

TOMASI, G., VAN DEN BERG, F., ANDERSSON, C. Correlation optimized warping and dynamic time warping as preprocessing methods for chromatographic data. *J. Chemometrics*, 18: 231–24, <https://doi.org/10.1002/cem.859>, 2004.

ULERY, A. L. & GRAHAM, R. C. Forest-fire effects on soil color and texture, *Soil Sci. Soc. Am. J.*, 57, 135–140, doi: 10.2136/sssaj1993.03615995005700010026x, 1993.

United Nations. Transforming our world: the 2030 Agenda for Sustainable Development. A/RES/70/1, Resolution adopted by the General Assembly on 25 September 2015.

USDA-NRCS. Soil Survey Staff. Soil taxonomy: A basic system of soil classification for making and interpreting soil surveys. 2nd edition. Natural Resources Conservation Service. U.S. Department of Agriculture Handbook 436. 1999.

VALDERRAMA, P., BRAGA, J. W. B., POPPI, R. J. Estado da Arte de Figuras de Mérito em Calibração Multivariada. *Quim. Nova*, Vol. 32, No. 5, 1278-1287, 2009.

VAN GRIEKEN, R. E. & MARKOWICZ, A. A. Handbook of X-Ray Spectrometry, 2nd edition, New York: Marcel Dekker Inc, 983 p., 2002.

WEINDORF, D. C., BAKR, N. & ZHU, Y. Advances in Portable X-ray Fluorescence (PXRF) for Environmental, Pedological, and Agronomic Applications. *Advances in Agronomy*, Volume 128, Chapter One 1-37, 2014.

WIETING, C., EBEL, B. A., SINGHA, K. Quantifying the effects of wildfire on changes in soil properties by surface burning of soils from the Boulder Creek Critical Zone Observatory. *Journal of Hydrology: Regional Studies* 13, 43-57. <http://dx.doi.org/10.1016/j.ejrh.2017.07.006>, 2017.

Yale University. XRD Principle. West Campus Materials Characterization Core. <<https://ywcmatsci.yale.edu/principle-0>>. Retrieved Sep, 2020.

YOSHIMURA, E. M. Física das Radiações: interação da radiação com a matéria. *Revista Brasileira de Física Médica*, 3(1): 57-67, 2009.

YUSIHARNI, E., GILKES, R. J. Soil minerals recover after they are damaged by bushfires. 19th World Congress of Soil Science, Soil Solutions for a Changing World, Brisbane, Australia. Published on DVD, 2010.

ANNEXES

ANNEX A

The elemental concentration of each element measured by EDXRF in unburned and fire-burned samples are presented in Table 1A.

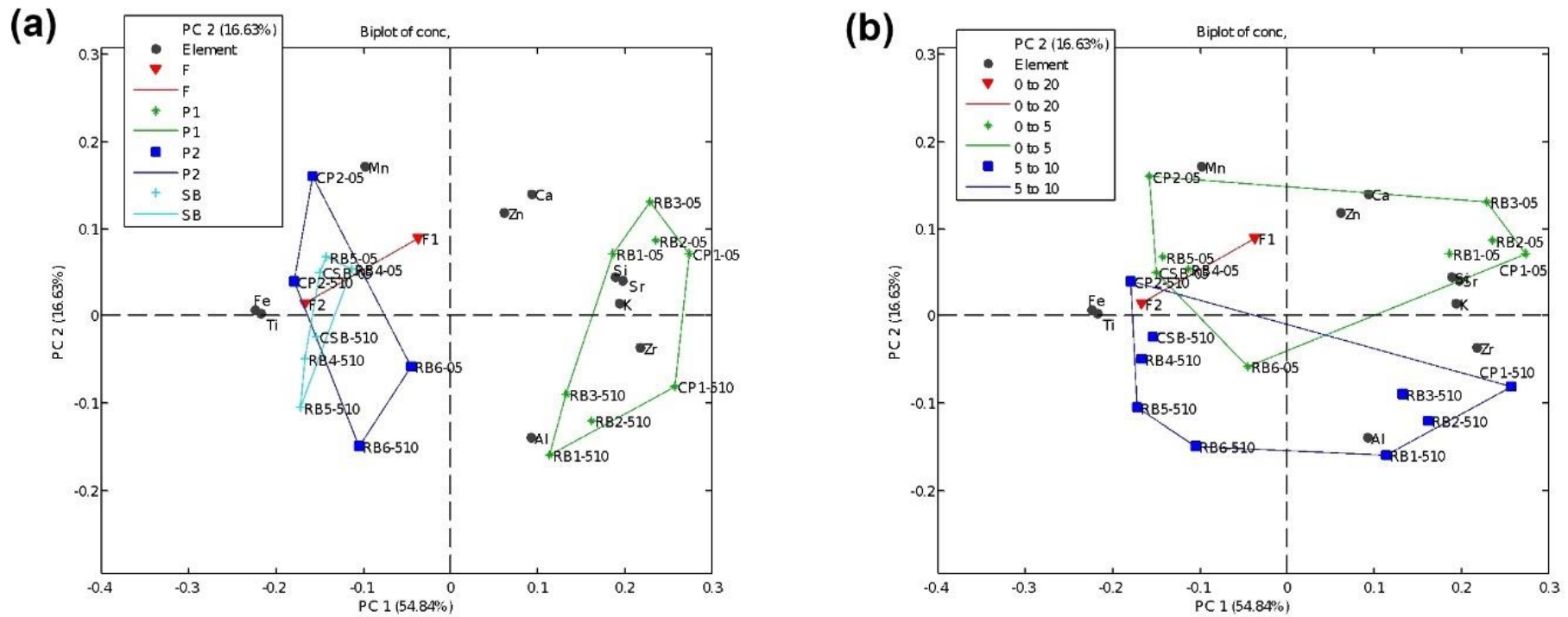
Table 1A - Samples and elemental concentrations with the respective standard deviation. Each value is a mean of three measurements. Indexes 0-5, 5-10 and 0-20 indicate 0 – 5.0 cm, 5.0 – 10.0 cm and 0 – 20.0 cm depth of collection, respectively

Sample	Al	Si	K	Ca	Ti	Mn	Fe	Zn	Sr	Zr
F1 ₀₋₂₀	8.8 ± 0.2	20.2 ± 1.3	0.037 ± 0.002	0.09 ± 0.01	1.23 ± 0.02	0.118 ± 0.004	5.68 ± 0.10	0.0055 ± 0.0010	0.0070 ± 0.0001	0.139 ± 0.004
F2 ₀₋₂₀	10.3 ± 0.1	17.2 ± 0.7	0.039 ± 0.001	0.11 ± 0.01	1.93 ± 0.04	0.083 ± 0.004	8.98 ± 0.03	0.0065 ± 0.0006	0.0061 ± 0.0001	0.068 ± 0.001
RB1 ₀₋₅	11.3 ± 0.5	18.0 ± 0.9	0.165 ± 0.002	0.45 ± 0.06	0.45 ± 0.03	0.057 ± 0.003	4.59 ± 0.03	0.0080 ± 0.0006	0.0082 ± 0.0002	0.177 ± 0.010
RB1 ₅₋₁₀	12.8 ± 0.5	17.1 ± 0.7	0.092 ± 0.002	0.14 ± 0.02	0.48 ± 0.01	0.014 ± 0.005	4.95 ± 0.09	0.0065 ± 0.0006	0.0074 ± 0.0001	0.168 ± 0.007
RB2 ₀₋₅	11.3 ± 0.6	20.0 ± 0.8	0.147 ± 0.004	0.65 ± 0.01	0.36 ± 0.02	0.042 ± 0.002	3.81 ± 0.04	0.0070 ± 0.0012	0.0089 ± 0.0003	0.144 ± 0.001
RB2 ₅₋₁₀	12.4 ± 0.5	18.5 ± 0.9	0.112 ± 0.001	0.19 ± 0.02	0.42 ± 0.01	0.016 ± 0.003	4.15 ± 0.06	0.0065 ± 0.0006	0.0077 ± 0.0001	0.174 ± 0.015
RB3 ₀₋₅	10.4 ± 0.7	19.2 ± 1.1	0.200 ± 0.006	0.64 ± 0.02	0.37 ± 0.01	0.052 ± 0.001	3.64 ± 0.04	0.0075 ± 0.0010	0.0085 ± 0.0001	0.163 ± 0.004
RB3 ₅₋₁₀	11.4 ± 0.7	17.6 ± 1.6	0.117 ± 0.000	0.14 ± 0.01	0.41 ± 0.01	0.009 ± 0.002	3.97 ± 0.06	0.0075 ± 0.0006	0.0073 ± 0.0002	0.163 ± 0.008
CP1 ₀₋₅	9.2 ± 0.6	22.6 ± 1.3	0.340 ± 0.010	0.29 ± 0.01	0.36 ± 0.02	0.044 ± 0.005	2.77 ± 0.05	0.0065 ± 0.0006	0.0082 ± 0.0002	0.188 ± 0.010
CP1 ₅₋₁₀	10.5 ± 0.4	20.8 ± 1.5	0.352 ± 0.010	0.15 ± 0.01	0.38 ± 0.02	0.018 ± 0.001	2.93 ± 0.02	0.0055 ± 0.0006	0.0077 ± 0.0002	0.209 ± 0.005
RB4 ₀₋₅	9.9 ± 0.6	15.5 ± 0.9	0.043 ± 0.003	0.41 ± 0.03	2.20 ± 0.04	0.054 ± 0.003	8.37 ± 0.09	0.0065 ± 0.0006	0.0072 ± 0.0002	0.078 ± 0.004
RB4 ₅₋₁₀	9.4 ± 0.4	14.2 ± 0.6	0.039 ± 0.005	0.13 ± 0.01	2.24 ± 0.05	0.027 ± 0.005	8.83 ± 0.05	0.0060 ± 0.0000	0.0069 ± 0.0001	0.077 ± 0.004
RB5 ₀₋₅	9.4 ± 0.8	15.4 ± 0.8	0.077 ± 0.005	0.39 ± 0.04	2.06 ± 0.04	0.066 ± 0.001	9.19 ± 0.07	0.0060 ± 0.0006	0.0069 ± 0.0001	0.067 ± 0.002
RB5 ₅₋₁₀	10.9 ± 0.4	14.9 ± 0.5	0.043 ± 0.003	0.11 ± 0.01	2.17 ± 0.06	0.031 ± 0.003	9.91 ± 0.05	0.0055 ± 0.0006	0.0066 ± 0.0002	0.071 ± 0.001
CSB ₀₋₅	8.8 ± 0.3	13.9 ± 0.9	0.039 ± 0.002	0.36 ± 0.02	2.30 ± 0.14	0.059 ± 0.005	8.13 ± 0.06	0.0055 ± 0.0006	0.0074 ± 0.0003	0.081 ± 0.006
CSB ₅₋₁₀	10.6 ± 0.4	16.0 ± 0.7	0.028 ± 0.001	0.11 ± 0.01	2.70 ± 0.08	0.051 ± 0.003	9.01 ± 0.01	0.0070 ± 0.0000	0.0069 ± 0.0001	0.082 ± 0.004
RB6 ₀₋₅	10.7 ± 0.8	16.8 ± 1.1	0.083 ± 0.002	0.29 ± 0.04	1.81 ± 0.03	0.039 ± 0.003	6.91 ± 0.04	0.0050 ± 0.0012	0.0072 ± 0.0001	0.103 ± 0.001
RB6 ₅₋₁₀	10.6 ± 0.5	15.6 ± 1.1	0.044 ± 0.004	0.11 ± 0.01	1.82 ± 0.08	0.024 ± 0.003	7.43 ± 0.07	0.0040 ± 0.0012	0.0069 ± 0.0003	0.101 ± 0.004
CP2 ₀₋₅	9.3 ± 0.2	16.0 ± 1.2	0.041 ± 0.002	0.25 ± 0.02	1.71 ± 0.11	0.104 ± 0.002	8.69 ± 0.08	0.0085 ± 0.0006	0.0064 ± 0.0001	0.066 ± 0.006
CP2 ₅₋₁₀	10.5 ± 0.2	16.7 ± 0.9	0.047 ± 0.003	0.16 ± 0.01	1.95 ± 0.02	0.099 ± 0.008	9.39 ± 0.03	0.0065 ± 0.0010	0.0062 ± 0.0002	0.064 ± 0.003

The PCA performed with the elemental concentration acquired by EDXRF is presented in Figure 1A. The data was preprocessed with autoscale. The number of principal components (PCs) chosen was 2, explaining 71.47% of the total variance. In Figure 1A(a), PC1 separates the pasture 1 samples (positive axis direction,

Al, Si, K, Ca, Zn, Sr and Zr) from other sites (negative axis direction, Ti, Mn and Fe). Figure 1A(b) shows that there is a tendency of samples collected from 0 – 5.0 cm to be at the first and second quadrants (except by RB6₀₅, that lays at the third quadrant), while samples collected from 5.0 – 10.0 cm are found at the third and fourth quadrants (except by CP2₅₁₀, that lays at the second quadrant). The samples collected from 0 – 5.0 cm have higher Si, Ca, K, Mn, Zn and Sr concentrations, while samples with 5.0 – 10.0 cm have more Al and Zr contents. The forest (0 – 20.0 cm depth) samples lay at the same direction of 0 – 5.0 cm depth samples (positive PC2) and in the PC1 negative direction (higher Ti, Mn and Fe contents).

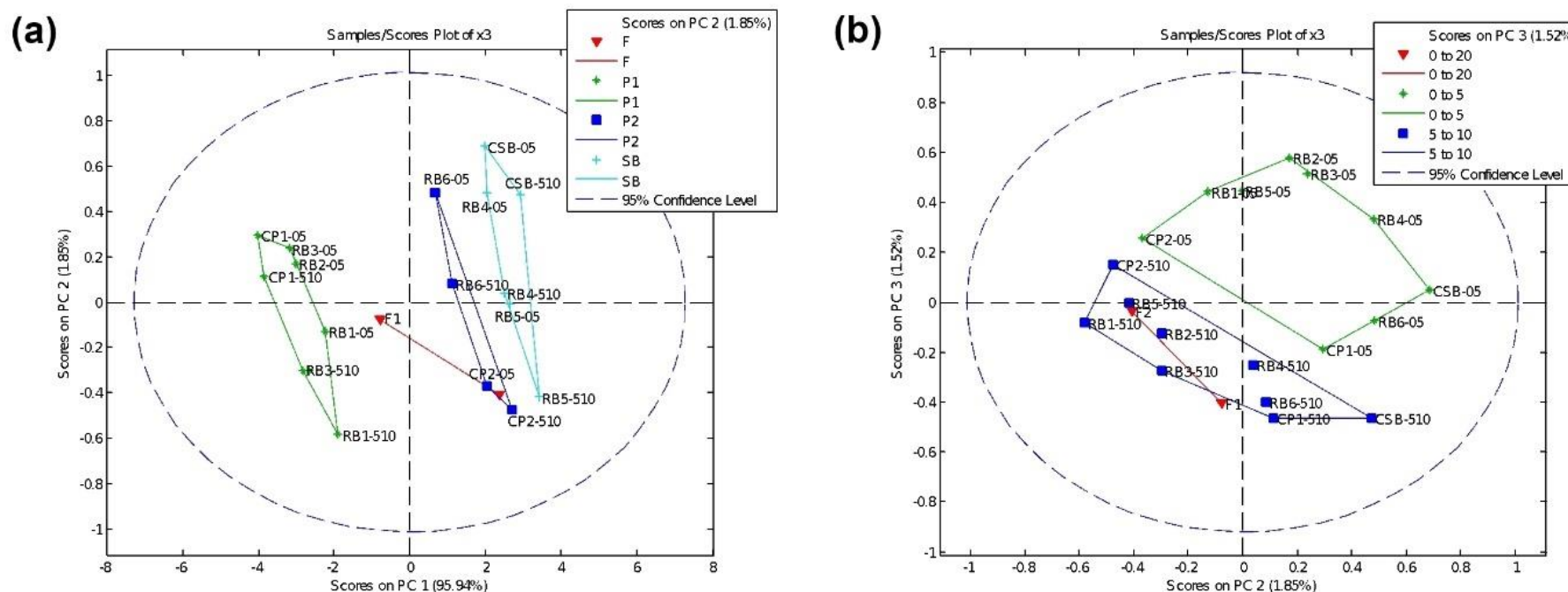
Figure 1A – PC1 x PC2 scores. PCA performed with the elemental concentrations of unburned and fire-burned samples. In (a), the color indicates the collection site. In (b), the color indicates the collection depth. F1 and F2: forests. RB1, RB2, RB3 and P1: pasture 1. RB4, RB5, and SB: slash-and-burn. RB6 and P2: pasture 2

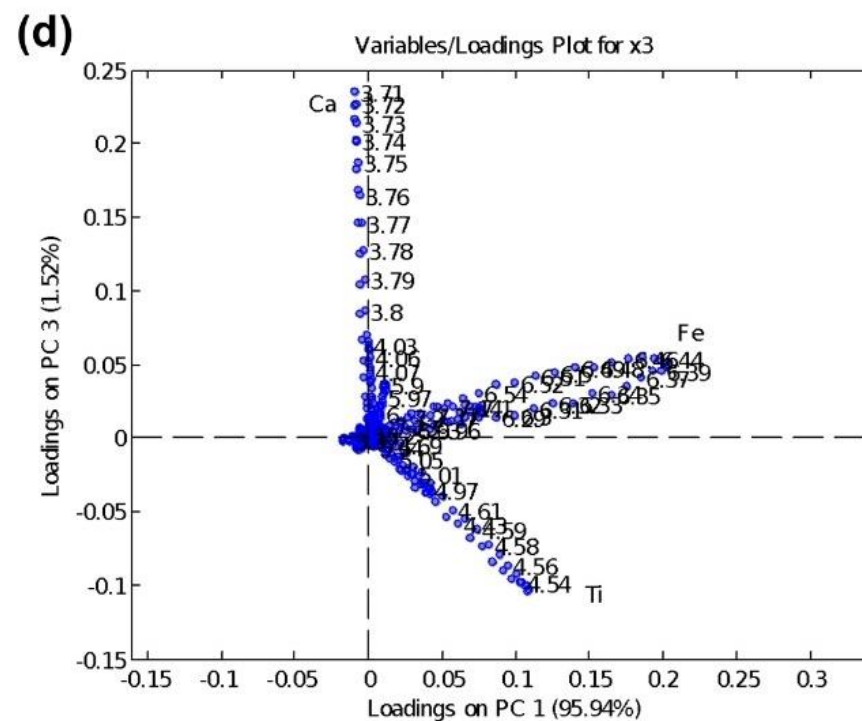
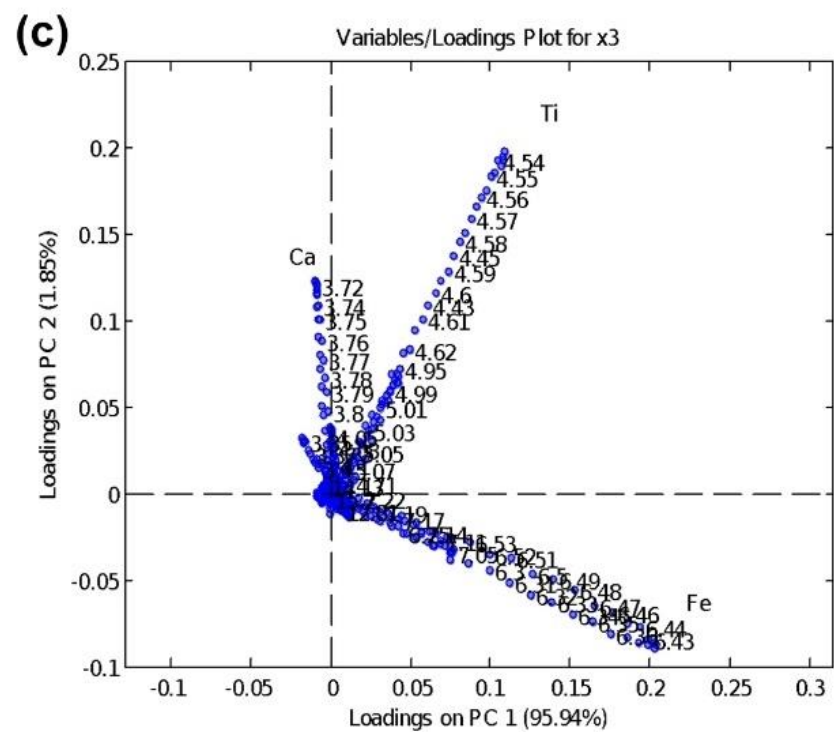


The PCA performed with 15 kV spectra and mean center preprocessing did not separate the samples by their collection depths, but according to their sites. Pareto scaling presented similar results to Poisson and mean center preprocessing. Scores plots are presented in the Figure 2A and loading in Figure 3A. Three principal components were selected for the PCA model. The explained variance was 95.94% in PC1, 1.85% in PC2 and 1.52% in PC3, totalizing 99.32% explained variance. PC1 x PC2 presented a separation between pasture 1 (PC1 negative direction) and samples from other sites (PC1 positive direction), while PC1 x PC3 grouped the samples by their collection depths. Forests F1 and F2 (both with 0 – 20.0 cm depth) are located closer to 5.0 – 10.0 cm depth samples.

PC1: positive contribution of Ti (4.51 keV) and Fe (6.41 keV), small negative contribution of Si (1.74 keV), K (3.31 keV) and Ca (3.69 keV). PC2: positive contribution of K, Ca, Ti, negative Fe contribution. PC3: positive contribution of Ca and Fe, negative contribution of Ti.

Figure 2A – (a) PC1 x PC2 and (b) PC2 x PC3 scores for 15 kV spectra model, using Poisson and mean center as preprocessing. (c) Loadings plot for PC1 x PC2 and (d) PC1 x PC3. Classes: F: forest. P1: pasture 1. P2: pasture 2. SB: slash-and-burn. The numbers after samples names mean the collection depth (05 for 0 – 5.0 cm and 510 for 5.0 – 10.0 cm). F1 and F2: forests. RB1, RB2, RB3 and P1: pasture 1. RB4, RB5, and SB: slash-and-burn. RB6 and P2: pasture 2. Ca Ka = 3.69 keV, Ti Ka = 4.51 keV, and Fe Ka = 6.41 keV





ANNEX B

PLS models were developed using the elemental intensities from EDXRF measurements (Al, Si, K, Ca, Ti, Mn, Fe, Zn, Sr, Zr). Compton correction (equation (8)) was also employed. The preprocessing method chosen was autoscale, and the cross-validation as made in blocks (one block for each collection site: F1, F2, CP1, CP2 and CSB) in both cases. Table B1 presents PLS models parameters, and Table B2 the cross-validation predicted temperatures. The accuracy of the models was poor, with RMSEC $\sim 100^{\circ}\text{C}$ and RMSECV $\sim 1000^{\circ}\text{C}$. The results were better (lower RMSECV and higher R^2 CV) without using the Compton correction. The temperatures estimated for RB samples ranged from 226 (pasture 1, elemental intensities model) to 476°C (pasture 2, Compton correction model).

Table 1B - PLS models developed with EDXRF elemental intensities and elemental intensities with Compton correction. LVs: number of latent variables. RMSEC: root mean squared error of calibration. RMSECV: root mean squared error of cross-validation. CV Bias: Cross-validation bias. R^2 Cal: determination coefficient of calibration. R^2 CV: determination coefficient of cross-validation

Model	LV	RMSEC ($^{\circ}\text{C}$)	RMSECV ($^{\circ}\text{C}$)	CV Bias	R^2 Cal	R^2 CV
Intensity	2	115	671	-250	0.5896	0.0378
Compton correction	2	145	1046	-584	0.3509	0.0034

Table 2B - Controlled-heat temperature and estimated temperature by PLS models developed with elemental intensities and Compton correction, with their respective relative deviations

Sample name and temperature ($^{\circ}\text{C}$)	Intensity		Compton correction	
	Estimated temperature ($^{\circ}\text{C}$)	Relative deviation	Estimated temperature ($^{\circ}\text{C}$)	Relative deviation
F1 (250)	186	-34%	478	48%
F1 (400)	149	-169%	453	12%
F1 (530)	318	-67%	518	-2%
F1 (600)	333	-80%	535	-12%
F1 (800)	567	-41%	630	-27%
F2 (250)	514	51%	467	46%
F2 (350)	693	49%	-863	141%
F2 (400)	540	26%	368	-9%
F2 (450)	724	38%	-790	157%
F2 (530)	688	23%	765	31%
F2 (550)	869	37%	-615	189%
F2 (600)	685	12%	497	-21%
F2 (650)	769	15%	-691	194%

F2 (750)	844	11%	-560	234%
F2 (800)	885	10%	898	11%
CP1 (250)	-1166	121%	-1593	116%
CP1 (400)	-1204	133%	-1755	123%
CP1 (530)	-1092	149%	-1774	130%
CP1 (600)	-1002	160%	-1663	136%
CP1 (800)	-892	190%	-1661	148%
CP2 (250)	463	46%	419	40%
CP2 (400)	406	2%	391	-2%
CP2 (530)	615	14%	485	-9%
CP2 (600)	584	-3%	510	-18%
CP2 (800)	726	-10%	587	-36%
CSB (250)	301	17%	364	31%
CSB (400)	227	-76%	346	-15%
CSB (530)	413	-28%	390	-36%
CSB (600)	398	-51%	399	-50%
CSB (800)	602	-33%	581	-38%
RB1	348		321	
RB2	343		325	
RB3	226		243	
RB4	309		370	
RB5	290		369	
RB6	380		476	